Investigation of the scalar variance and scalar dissipation rate in URANS and LES

by

Isaac Keeheon Ye

A thesis
presented to the University of Waterloo
in fulfillment of the
thesis requirement for the degree of
Doctor of Philosophy
in
Mechanical Engineering

Waterloo, Ontario, Canada, 2011

©Isaac Keeheon Ye 2011

I hereby declare that I am the sole author of this thesis. This is a true copy of the thesis, including any required final revisions, as accepted by my examiners.

I understand that my thesis may be made electronically available to the public.

Abstract

Large-eddy simulation (LES) and unsteady Reynolds-averaged Navier-Stokes (URANS) calculations have been performed to investigate the effects of different mathematical models for scalar variance and its dissipation rate as applied to both a non-reacting bluff-body turbulent flow and an extension to a reacting case. In the conserved scalar formalism, the mean value of a thermo-chemical variable is obtained through the PDF-weighted integration of the local description over the conserved scalar, the mixture fraction. The scalar variance, one of the key parameters for the determination of a presumed β-function PDF, is obtained by solving its own transport equation with the unclosed scalar dissipation rate modelled using either an algebraic expression or a transport equation. The proposed approach is first applied to URANS and then extended to LES. Velocity, length and time scales associated with the URANS modelling are determined using the standard two-equation $k-\varepsilon$ transport model. In contrast, all three scales required by the LES modelling are based on the Smagorinsky subgrid scale (SGS) algebraic model. The present study proposes a new algebraic and a new transport LES model for the scalar dissipation rate required by the transport equation for scalar variance, with a time scale consistent with the Smagorinsky SGS model.

Acknowledgement

God is good all the time! Everything is done by His grace!

First of all, I cannot find enough words to thank my supervisor, Professor Fue-Sang Lien for his warm consideration and kind advice. Professor Lien always encouraged me and helped me to finish my studies. Special thanks is also due to Dr. Eddy Chui for providing me with insightful comments based on his field experience and for supporting my study financially, to Professor Cecile Devaud for her encouragement, to Professor Hans De Sterck for introducing me to a mathematical understanding of CFD, and to Professor Xianguo Li for his advice on real combustion phenomena. I also appreciate Professor Clinton Groth at University of Toronto for his kind comments as the external committee member.

There are a number of great colleagues within our research group that made the long journey of study more enjoyable and interesting; I believe it was a great blessing to me. In particular, I would like to acknowledge Ho-Jun Ahn who helped me to begin my studies smoothly and gave me great advice about life; Andrew Keats who was a big help in many ways; Johan Larsson who was a great office-mate, and Andrea Scott and Kun-Jung Hsieh with whom I shared good discussions on many topics. Furthermore, I would like to give thanks to Professor Yong-Mo Kim at Hangyang University, Seoul, Korea, who helped me to build a good foundation in CFD and turbulent combustion during my Master's degree coursework, and to Dr. Gun-Hong Kim who answered my many combustion questions.

During the many years of study, my family has always been the greatest source of strength and support. My parents and parents-in-law in Korea encouraged me all along and respected my decisions. My two sons, Eugene and Ian, gave me great joy and comfort, and motivated me to continue my work. To my wife, Jiyeon, who has been with me every step of the way through each defeat and achievement, I would like to give the most thanks of all.

I would like to recognize and thank CANMET Energy Technology Centre-Ottawa, Natural Resources Canada for financially supporting this study.

Table of contents

List of Figures

List of Tables

Nomenclature

Abbreviations

CDS Central Difference Scheme

DM Dynamics Smagorinsky model

DNS Direct Numerical Simulation

Le Lewis number

LES Large Eddy Simulation

MPI Message Passing Interface

NM No-SGS model

NRBB Non Reacting Bluff Body

PDF Probability Density Function

RANS Reynolds-Averaged Navier-Stokes

RBB Reacting Bluff Body

Re Reynolds number

rms root-mean-square

SGS Sub-Grid Scale

SM Static Smagorinsky model

URANS Unsteady RANS

Greek symbols

χ	scalar dissipation rate of the scalar
δ_{ij}	Kronecker delta
$\dot{\omega}_k$	Chemical reaction of the species k
ℓ_s	Scalar turbulence length scale
ℓ_u	Mechanical length scale
κ	von Karman constant, 0.4187
λ	Thermal diffusivity
μ	Molecular viscosity
ν	Kinematic viscosity
ν'_{kl}, ν''_{kl}	Stoichiometric coefficients of reaction l of the species k
ω_l	Rate of reaction l
ϕ	General variable
ρ	Density
τ^d_{ij}	Deviator of τ_{ij}
τ_s	Scalar turbulence time scale
τ_{ij}	Shear stress in fluids
τ_s	Scalar times scale
τ_u	Turbulence times scale
ξ, η, ζ	General curvilinear coordinate system
R_τ	Mechanical to scalar time scale ratio

Roman symbols

Δt	Numerical time-step
$\hat{\Delta}$	Test-filtered grid size
$\nabla\phi$	Gradient of variable ϕ

$\overline{\Delta}$ Filtered grid size

τ_w Wall shear stress

$\widetilde{\phi}$ Favre-filtered or Favre-averaged variable

$\widetilde{Z''^2}$ Scalar variance in RANS

$\widetilde{Z'^2}$ Scalar variance in LES

A^+ van Driest damping function constant

A_k Arrhenius pre-exponential factor

C_χ Model constant for the scalar dissipation algebraic model

C_g Gradient-based model constant

C_S Smagorinsky constant

$C_{p,k}$ Specific heat ratio of the species k

C_{ss} Scale similarity model constant

D Molecular diffusivity

D_k Molecular diffusivity of the species k

E_k Activation energy

h_k Enthalpy of the species k

J Jacobian for the coordinate transformation

K_{cl} Equilibrium constants

k_{fl}, k_{bl} Forward, backward rate coefficient of reaction l

L_x, H, L_z Computational domain size x, r, z

Le_k Lewis number of the species k

m_α mass of the element α

n_k Number of moles of species k

P Pressure

R Gas constant

Re Reynolds number

s Entropy

S_{ij} Rate-of-strain tensor

Sc Schmidt number

T_b Flow-through time, $T_b = H/U_b$

U, V, W Contravariant velocities

u_τ Friction velocity, $\sqrt{\tau_w/\rho}$

U_b Bulk velocity

u_j Instantaneous velocity

W_k Molecular weight of the species k

y^+ Viscous scale, $y^+ = u_\tau y/\nu$

Y_k Mass fraction of the species k

Z_{st} Stoichiometric mixture fraction

Subscripts

E, W, N, S, T, B Grid indices in the discretized system

i, j, k Tensor indices

s Isotropic process

st Stoichiometric condition

w Quantity at a solid wall

sgs Property at Subgrid-scale level

T Transpose

t Property of turbulence

Chapter 1

Introduction

1.1 Introduction

An understanding of turbulent reacting flows is essential in the design of many engineering devices such as furnaces, gas turbines, and internal combustion engines, and there is a clear need to predict their performance. The majority of current methods for calculating the properties of turbulent reacting flows and practical combustion systems are based on Reynolds averaging of the Navier-Stokes equations (RANS). This traditional approach has met with variable success in reproducing many of the important effects present in practical combustion systems. However, RANS calculations often show weakness in predicting flow separation and recirculation correctly due to limitations of the model itself. Large eddy simulation (LES) represents a potentially powerful and promising method of overcoming some of the deficiencies of RANS calculations.

The range of scales in turbulent flow motions is a strong function of the Reynolds number. In DNS, all the scales of motion, up to and including the dissipative scales of order η, the Kolmogorov scales, must be resolved; the computational domain must be significantly larger than the scale of the largest eddies, L, while the grid size must

be of order η, and the number of grid points required is proportional to the ratio $L/\eta \approx Re^{3/4}$ [76] (where Re is the Reynolds number based on the integral scale of the flow). Thus, the number of grid points needed to perform a three-dimensional DNS scales as the 9/4 power of the Reynolds number. The time-scale of the smallest eddies also supplies a bound for the maximum time-step allowed: since the ratio of the integral time-scale of the flow to the Kolmogorov time-scale is also proportional to $Re^{1/2}$, the number of time-steps required to advance the solution by a fixed time has the same dependence on Re. Assuming that the CPU time required by a numerical algorithm is proportional to the total number of points N, the cost of a calculation will depend on the product of the number of points by the number of time-steps, hence to $Re^{11/4}$. Therefore, as shown in Table 1.1, it is not feasible to perform DNS calculations for high-Reynolds number situations in near future.

The RANS approach corresponds to the opposite end of the computational complexity spectrum. In this approach, only the time-averaged flow properties are resolved, with all other scales of motion being modelled. The computational cost of RANS is independent of the Reynolds number, except for wall-bounded flows where the number of grid points required in the near-wall region is proportional to $\ln Re$ [69]. Because of its computational efficiency, RANS is the most commonly used CFD methodology for the simulation of turbulent flows encountered in industrial and engineering applications. However, the RANS approach can perform poorly in the prediction of features

Reynolds number	CPU-	Time
94	20	Mins
375	9	Hours
1500	13	Days
6,000	20	Months
24,000	90	Years
96,000	5,000	Years

Table 1.1: Estimates for DNS of isotropic turbulence at various Reynolds numbers [69].

in complex flows (e.g., bluff body flows), which tend to be dominated by coherent large-eddy structures. Because most turbulence models used in RANS are empirically tuned to optimize their performance in simple and thin shear flows where the mean pressure gradient and mean streamline curvature are small, RANS is generally unable to capture correctly the geometry-dependent large eddies in many complex flows.

LES stands in the middle of the range of turbulent flow prediction tools, between direct numerical simulation (DNS), in which all scales of turbulence are numerically resolved and which is hence expensive in computational cost, and RANS calculations, in which all scales of turbulence are modelled and which is hence relatively cheap in computational cost. In LES, the large, energy-containing scales of turbulence are resolved by the discretized equations, whereas the small scales of turbulence are modelled through the subgrid-scale (SGS) models to replace the information that has been removed in the discretized equations by the filtering operation. The large scales, which usually control the behavior and the statistical properties of turbulent flows, tend to be geometry and flow dependent, whereas the small scales tend to be more universal in their statistical description and consequently easier to model. In many practical combustion devices such as furnaces, boilers, and gas turbines, the flames are essentially controlled by the rate of mixing and hence an accurate description of turbulent large scale mixing is of crucial importance in the simulation of such flames. LES offers the possibility of improvement in this area by providing a description of the dynamics of the large scales that is of greater accuracy than can be attained with RANS calculations.

Even though LES only resolves the large scales and models the small or sub-grid scales, LES is still expensive in the computational cost. The cost of LES also depends on the Reynolds number if a solid surface is present, since in that case even the largest scales of motion depend on the Reynolds number. Chapman [8] estimated that the resolution required to resolve the outer layer of a growing boundary layer is proportional to $Re^{0.4}$, while for the viscous sublayer the number of points needed increase at least $Re^{1.8}$. Thus, although LES can give some improvement over RANS, and be extended to flows at Reynolds numbers at least an order of magnitude higher

than DNS at a reasonable cost, its application to engineering flows remains expensive.

The application of LES to turbulent reacting flows has been a subject of growing interest with the rapid growth in computing power, but to date few simulations of realistic combustion systems have been undertaken. The primary difficulty in applying LES to turbulent reacting flows is that in general, chemical reactions take place below the resolved (grid) scale. Hence, chemical reactions must be entirely modelled and it is necessarily required to obtain an accurate physical description of the reaction processes at the SGS level within each LES grid cell. This is also true for RANS calculations. Therefore, most of studies on LES combustion are the extension of the well-established approaches in RANS.

For non-premixed combustion, mixing at the molecular level between fuel and oxidizer must occur prior to chemical reactions. Furthermore, during the combustion process many intermediate and stable species are produced and consumed, and their local concentrations are also strongly affected by the mixing process. As will be discussed in Sec. 2.2.1, a conserved scalar approach based on the mixture fraction, the so-called conserved-scalar formalism, is introduced to simplify the subsequent analysis and discussion of such a multi-component system involving chemical reactions. In this conserved-scalar formalism, the local mixing state is determined by the mixture fraction. Furthermore, the local thermo-chemical variables such as temperature and species mass fractions are described solely by the conserved scalar, the mixture fraction. Therefore, the main issues involved in implementing this formalism are firstly how to obtain the accurate local mixing state and secondly how to model the local chemical reaction processes.

The description of the mixture fraction distribution in a local cell is often modelled using a probability density function (PDF). In the conserved-scalar formalism, the mean values of any local thermo-chemical variable can be obtained through

$$\widetilde{\phi} = \int_0^1 \phi(Z)\widetilde{P}(Z)dZ, \tag{1.1}$$

provided the functional dependence of the local variables on the scalar, $\phi(Z)$, and the local distribution of the scalar, $\widetilde{P}(Z)$, are known. Here, Z stands for the mixture

fraction. Note that in this work, the mixture fraction is called the *scalar* for the purpose of general use.

The shape of the PDF $\tilde{P}(Z)$ can either be presumed a priori, or else it can be obtained by solving a PDF transport equation. Following many previous reports [14, 20, 35, 65, 67], the shape of PDF is presumed in the present study to save computational cost. Even though there is argument about what kind of the presumed PDF shape would be appropriate, a β-function PDF, which is parameterized by the mean and the variance, has been widely adopted. Since the PDF is used to describe the local mixing state, the mean and the variance of the mixture fraction are required to construct the $\beta-$function PDF. The problem of how to accurately model the mixing now shifts to how to correctly describe the evolution of mean and variance of the scalar (i.e., mixture fraction) as a consequence of turbulent mixing.

Consider an analogy between the flow and the scalar; the scalar variance corresponds to the turbulent kinetic energy while the scalar mean to the mean velocity. Similar to the two-equation $k-\varepsilon$ turbulence model, the scalar dissipation rate, χ, is required and needs to be coupled with the scalar variance. The scalar dissipation rate also plays an important role in chemical reaction processes where it signifies the local mixing rate. $1/\chi$ is often interpreted as a characteristic turbulent diffusion or mixing time. The scalar dissipation rate is also involved in a steady laminar flamelet model, which can account for the non-equilibrium chemistry that is of particular importance for the formation of pollutants such as nitric oxides in turbulent combustion. It describes the influence of the turbulent flow field on the laminar flame structure and is an essential non-equilibrium parameter since it measures the degree of departure from chemical equilibrium.

As mentioned earlier, the present work is based on the conserved-scalar formalism with the presumed $\beta-$function PDF. Having said that the accurate description of local mixing depends on the accuracy of the $\beta-$function PDF, the scalar mean, the variance and its dissipation rate are required to be calculated accurately.

1.2 Literature review and motivation

LES has been developed and studied as a turbulent flow prediction tool for engineering applications during the past three decades. Significant progress has taken place more recently with advances in computer technology and the development of the dynamic SGS modelling procedure by Germano *et al.* [23]. With the dynamic procedure, model coefficients are automatically computed using information contained in the resolved turbulence scales, thereby eliminating the uncertainties associated with tunable model parameters. Reviews of LES are given by Lesieur and Métais [42] and Moin and Kim [53].

Techniques for computational modelling of turbulent combustion have been the subject of numerous studies, with significant advances attributable to the development of the laminar flamelet model by Peters [61, 62], the probability density function (PDF) transport method by Pope [68], the conditional moment closure modelling (CMC) by Klimenko and Bilger [38], and linear eddy modelling by Kerstein [36]. All of the aforementioned models can be regarded as advanced models capable of handling finite-rate chemistry or non-equilibrium chemistry effects. The pdf transport model is theoretically the most accurate and is capable of handling the reaction rate term without requiring any modelling assumptions. However, the model is very resource-intensive and its application to industrial calculations is still not widespread. The CMC model is a newer model which is currently gaining in popularity, but the model is again resource-intensive and its successful application to practical situations has yet to be assessed. The laminar flamelet model based on the conserved scalar formalism is the most popularly accepted due to its relative ease of implementation and its relatively low computational cost. All these combustion models have been successfully incorporated in RANS calculations for decades. Many of these established combustion-modelling approaches used previously in RANS calculations have recently been extended for use in LES.

The LES formalism introduces a filtering operation in space that is applied to the governing equations and flow variables to remove the unresolved small scales, i.e.,

subgrid-scales (SGS). Similarly, as in RANS-based combustion models, the direct modelling of a filtered chemical source term is a very challenging problem. Due to the strong non-linear dependence of the Favre-filtered mean chemical source term $\widetilde{\dot{\omega}_k}$ on the temperature (T) and the species mass fractions (Y_k) and on their strong fluctuations in turbulent flows, this source term cannot be easily calculated by the mean value of the species mass fraction and temperature. This means that

$$\widetilde{\dot{\omega}_k}(T, Y_1, \ldots, Y_N) \neq \dot{\omega}_k(\widetilde{T}, \widetilde{Y_1}, \ldots, \widetilde{Y_N}), \tag{1.2}$$

where N is the number of the species.

For non-premixed combustion, however, the treatment of the chemical source term can be avoided by employing the conserved scalar formalism. A transport equation for a single, strictly conserved scalar, which is the mixture fraction (Z), can be derived from the transport equations of element mass fractions. A detailed discussion of this will be presented in Sec. 2.2.2. The conserved scalar formalism is a reasonable approximation to conditions found in many practical combustion processes, where flames are essentially controlled by the large scale mixing rate at which the fuel and oxidant mix. LES resolves the large scale motions of turbulent flow and hence LES has potential advantage over the RANS-based calculation. In the conserved-scalar formalism, the description of the local thermo-chemical variables is uniquely related to the mixture fraction and their mean values are calculated through the PDF integration.

The extension of the conserved scalar formalism and the presumed PDF approach into LES has been the subject of recent studies. Many studies have been successfully performed especially in conjunction with laminar flamelet models. To the author's knowledge, Cook *et al.* [14] first proposed a presumed subgrid-scale PDF method of the mixture fraction in analogy to RANS calculations and showed that the results were in good agreement with DNS data obtained by *a priori* test in homogeneous turbulence. In a similar fashion, De Bruyn Kops *et al.* [17] performed a LES calculation and successfully reproduced the spatial average of the filtered species concentration obtained from DNS. Branley and Jones [6] performed a LES calculation of a hydrogen-air jet flame, in which various closure models for the the SGS stresses and fluxes were

tested. Kempf *et al.* [27, 33, 35] successfully incorporated a multi-step chemical mechanism in LES calculations. Pitsch and Steiner [66, 67] used the unsteady laminar flamelet model in LES simulation of a piloted jet diffusion flame (Sandia flame D). For a non-premixed bluff-body stabilized flame (Sandia flame HM1), Janicka and Kempf [34] had successfully performed a LES calculation with the steady laminar flamelet model, and Raman and Pitsch [71] achieved very impressive agreement with experimental data [16] by taking additional steps to ensure grid independence. Martinez and Kronenburg [52] reported good prediction of temperature and reactive species mass fractions using LES together with the CMC model.

The recent studies on LES applied to reacting flows [12, 27, 28, 29, 34, 64, 71] suggest that a description of the PDF of the mixture fraction at the SGS is important. It is generally agreed that the SGS statistics of the conserved scalar can be described by a β-function PDF that is parameterized by the scalar mean and the variance [29]. For RANS and LES, the scalar mean is commonly obtained by solving its own transport equation. However, approaches to obtaining the scalar variance and its dissipation rate differ for RANS and LES calculations.

In RANS, the scalar variance ($\widetilde{Z''^2}$) is commonly calculated by solving its own transport equation. The unclosed scalar dissipation rate ($\widetilde{\chi} = 2D\widetilde{\left(\frac{\partial Z''}{\partial x_j}\right)^2}$) in the scalar variance transport equation needs to be modelled [62], and the accuracy of the scalar variance prediction is influenced significantly by how the scalar dissipation rate is modelled. The scalar dissipation rate can be modelled by either using an algebraic expression or by solving its own transport equation. The algebraic model assumes that the mechanical time scale (τ_u) is linearly related to the scalar time scale (τ_s). Furthermore, the ratio of the two time scales ($R_\tau = \tau_u/\tau_s$) is often assumed to be constant for a given flow. Physically, R_τ expresses the ratio of the local turn-over time for the energy-containing velocity and scalar eddies. These energy-containing eddies are influenced significantly by the production mechanisms of the respective velocity and scalar fields. It is, therefore, reasonable to expect that R_τ depends on these production mechanisms, which could vary drastically among different flows [57]. It is our belief that, in the most general setting, it is necessary to obtain the scalar

dissipation rate by solving its own transport equation, which again involves several unclosed terms that need to be modelled (see Sections 3.1.2 and 3.2.2 later).

Unlike RANS, the SGS scalar variance[1] in LES has traditionally been obtained by using algebraic models, such as the scale similarity model [13] and the gradient-based model [64]. Cook and Riley [13] proposed a scale similarity model, by defining the scalar variance as

$$\widetilde{Z''^2} = C_{ss}\left(\widehat{\widetilde{Z}\widetilde{Z}} - \widehat{\widetilde{Z}}\widehat{\widetilde{Z}}\right), \tag{1.3}$$

where $\widehat{\cdot}$ is a test filter with the width $\widehat{\Delta} = 2\overline{\Delta}$. C_{ss} is the model constant and must be given prior to the calculation. The scale similarity model implicitly assumes that the smallest resolved scales are statistically similar to the largest unresolved scales. This simple assumption seems to be less feasible in the case of reacting flows because all chemical reactions occur at the smallest unresolved scales [67]. Furthermore, the model constant must be known prior to the calculation, and there is no reason to expect a universal value for the model constant.

Pierce and Moin [63] proposed an algebraic scaling formula for the scalar variance and computed its model constant (C_g) using the dynamic procedure [23, 47] following

$$\widetilde{Z''^2} = C_g\overline{\Delta}^2|\nabla\widetilde{Z}|^2. \tag{1.4}$$

The gradient-based model calculates the scalar variance based on the gradient of the scalar mean. Intuition seems to suggest that the scalar variance can be high in a region where the gradient of scalar mean is high. However, experimental data of the scalar mean shows low gradient but high scalar variance very close to the centerline. In this region, the predicted scalar variance is obviously erroneous when the gradient-based model is employed.

Although existing scalar variance models used in LES have performed relatively well, it should be pointed that all the existing models for the scalar variance are calculated

[1]The scalar variance at SGS is denoted hereafter 'scalar variance' in short throughout the study. The scalar variance in URANS and LES has the same form but one in URANS comes from the time-averaging and one in LES comes from the spatial filtering operation

independently. Having said that there is an analogy between the turbulent kinetic energy and the scalar variance and the turbulent kinetic energy dissipation rate and the scalar dissipation rate, the scalar variance should be obtained as a coupled system with the scalar dissipation rate. It is noted here that existing scalar variance and SGS scalar dissipation rate[2] modelling strategies are quite different. The scalar dissipation rate has usually been determined based on the local equilibrium assumption [13, 17, 64, 63], under which the production of the scalar variance by the resolved scale is equal in magnitude to its SGS dissipation rate. Thus, the local equilibrium assumption leads to a simple model which equates the scalar dissipation rate to the local scalar variance production rate. The scalar dissipation rate at the SGS level can be written as

$$\widetilde{\chi}_{sgs} = 2D_{sgs}|\nabla\widetilde{Z}|^2, \tag{1.5}$$

where D_{sgs} is the SGS diffusivity. This model has the same form as the leading term in a model proposed by Girimaji and Zhou [24], which is derived using the local equilibrium assumption as well.

However, this local equilibrium assumption is only strictly correct in an equilibrium flow. In general, it is not always true because the scalar variance and the scalar dissipation rate are strongly coupled together, affecting turbulent mixing mechanisms. Furthermore, the scalar transport equation has no sink or source terms under this assumption. That, as Jiménez *et al.* [28] reported, would lead to unphysical simulations in which the scalar variance would not decay and complete mixing of reacting species would not be attainable.

Alternatively, Jiménez *et al.* [28] suggested solving a scalar variance transport equation in a similar way to a RANS-based method. The unclosed scalar dissipation rate term is suggested to be closed using the algebraic model, which is also similar to the RANS-based method that is explained above.

$$\frac{\widetilde{\chi_{sgs}}}{\widetilde{Z'^2}} \sim C_{\widetilde{\chi}}\frac{\widetilde{\varepsilon}_{sgs}}{\widetilde{k}_{sgs}}, \tag{1.6}$$

[2]The SGS scalar dissipation rate is denoted hereafter 'scalar dissipation rate' in short throughout this study. Similar to the scalar variance, it has the same form for URANS and LES but has different definition.

where $\widetilde{k}_{sgs}$ is the SGS kinetic energy and $\widetilde{\varepsilon}_{sgs}$ is the SGS kinetic energy dissipation rate. An *a priori* test of this model in homogeneous isotropic turbulence [28] shows better agreement with DNS data than the two previous models, and Sun and Su [83] confirmed the superiority over the previous models through an *a priori* test with experimental data of a turbulent cross-flow jet.

However, measurements and predictions of turbulent jets and diffusion flames in the literature indicate that the mechanical and the scalar time scales are not always proportional; i.e., R_τ is not constant in the entire flow region. The measured Prandtl number in a heated round jet by Chevray and Tutu [11] was not constant and neither was the time scale ratio measured in a helium-air jet by Panchapakesan and Lumley [59]. If the time scale ratio is not constant, a transport equation for the scalar dissipation rate is required.

As pointed out earlier, the scalar variance and its dissipation rate have been independently calculated in LES primarily to reduce computational time. However, there is a strong need to solve for these variables in a coupled system in order to achieve both physical consistency of the scalar variance and its dissipation rate mechanism and more importantly to obtain accurate predictions.

1.3 Objectives

This study develops a large eddy simulation based prediction methodology for turbulent reacting flows with principal application to a non-premixed bluff-body stabilized flame. A bluff-body flame is a very challenging test case since the flame itself is stabilized by recirculation zones near the solid bluff body, with strong turbulent mixing initiating and maintaining the reactions. RANS calculations show deficiencies, and LES is expected to perform better.

There are two major objectives to this work: to compare the performance of different turbulence models in describing turbulent mixing mechanisms, and to examine the

predictability of scalar variance and scalar dissipation rate using Unsteady RANS (URANS) and LES. For the former objective, URANS with the standard $k-\varepsilon$ model and LES with the standard Smagorinsky SGS model are used. For the latter objective, the present study proposes a new algebraic and a new transport model for the scalar dissipation rate in LES, using a time scale consistent with the Smagorinsky SGS model. To this end, the transport equation for the scalar dissipation rate, which was proposed for RANS calculations by Jones and Musonge [31], is adopted. These models are used in conjunction with the scalar variance transport equation to study a bluff-body non-reacting flow, for which a wealth of experimental data is available [16].

The scalar variance equation is solved first using URANS in conjunction with two different scalar dissipation rate models, namely the algebraic model and the transport equation model. The URANS scalar dissipation rate models are then modified to fit into the present LES framework, in which no $\widetilde{k}-$ and $\widetilde{\varepsilon}-$transport equations are solved in order to reduce computational cost. While the new approach for the scalar variance and its dissipation rate at SGS level is implemented in LES, all existing scalar variance models are also simulated for comparison purpose. All calculations are conducted to simulate the non-reacting bluff-body (NRBB) case first and the reacting case (RBB) is pursued later.

As a milestone to achieve the objectives above, a LES code based on STREAM [44] has been developed and furthermore the code has been parallelized using MPI [51] in order to cope with the computational time required. The developed LES code is first validated by simulating a turbulent channel flow for $Re_\tau = 180$ [37]. The turbulent channel flow is a popular choice for code validation and is adequate in consideration of the bluff-body flow in this study because it also has a wall-boundary.

More clearly, the present work is expected to deliver the following contributions:

1. The development of new algebraic and transport models for the scalar dissipation rate in LES based on consistency with the Smagorinsky SGS model.
2. A comparative study on the scalar variance and the scalar dissipation rate in URANS and LES by performing tests at the same grid-resolution.

3. URANS and LES calculations for non-reacting and reacting bluff-body flows incorporating the scalar dissipation rate transport equation.

4. An in-depth study into the scalar variance and the scalar dissipation rate modelling in LES, which has potentially contributed to a comprehensive understanding of the local mixing state.

5. Successful extension of the well-established RANS-based method which is based on the conserved-scalar formalism and the presumed-PDF approach to LES combustion.

1.4 Outlines

The present work is organized into 8 chapters. Following the introduction, chapter 2 will present the mathematical foundations for URANS and LES respectively, including the introduction of the conserved-scalar formalism, which is a key frame for the subsequent discussion. Furthermore, the turbulence modelling techniques of URANS and LES will be presented, and the combustion models will follow.

Chapter 3 will present the comprehensive study on the modelling of the scalar variance and its dissipation rate at subgrid-scale, which is claimed as one of contributions in this study. Numerical method and code validation will be presented in chapter 4 and chapter 5. In chapter 4, the general and conventional finite volume discretization, boundary condition for the bluff-body simulation, and the parallelization will be presented. The turbulent channel flow as a code validation is discussed in chapter 5.

In chapter 6, the non-reacting bluff-body (NRBB) case is simulated by both URANS and LES and the results are discussed. The same approach used in the NRBB case is extended to simulate the reacting bluff-body (RBB) case in chapter 7. The URANS results are first obtained and discussed, and LES is left for future work. Chapter 8 summarizes the present work and presents potential work to be done in future.

Chapter 2

Mathematical Formulation

The starting point for the computational investigation is a statement of the governing equations of mass, momentum and energy for the phenomena under study. This chapter consists of two parts: the first is to present the governing equations for the flow and turbulence motions, and the second introduces the conserved scalar formalism and combustion models for the mixing state and reacting phenomena. URANS and LES formulations for turbulent flows are firstly derived by respectively applying an averaging operator and a filter to the governing equations. The arising Reynolds or subgrid-scale stresses must be modelled and are discussed in detail. Following the mathematical description of the flow motions and turbulence models, the conserved scalar formalism is introduced. In the frame of the conserved scalar formalism, the conserved scalar (the mixture fraction in this work) equation is solved and the local thermo-chemical variables of combustion models are integrated through the PDF approach [62]. The presumed β-function PDF approach, which requires the mean and the variance, is introduced and discussed.

2.1 Governing equations of Fluid Motion

2.1.1 Governing equations

The motion of a Newtonian fluid is governed by the Navier-Stokes equations. In Cartesian coordinates with the absence of body forces, these can be written as

$$\frac{\partial \rho}{\partial t} + \frac{\partial (\rho u_j)}{\partial x_j} = 0, \tag{2.1}$$

$$\frac{\partial (\rho u_i)}{\partial t} + \frac{\partial (\rho u_i u_j)}{\partial x_j} = -\frac{\partial p}{\partial x_i} + \frac{\partial}{\partial x_j}\left[\mu\left(\frac{\partial u_i}{\partial x_j} + \frac{\partial u_j}{\partial x_i} - \frac{2}{3}\delta_{ij}\frac{\partial u_l}{\partial x_l}\right)\right], \tag{2.2}$$

where μ is the fluid molecular viscosity.

In reacting flow simulation, the flow field is coupled to chemical reactions through updating the density using the equation of state (Eq. (2.6)). The temperature used to update the density is obtained by solving the energy equation. The energy equation in this study is written in terms of the total enthalpy [62]. With the gradient assumption for the molecular enthalpy flux and neglecting radiative heat transfer, the total enthalpy energy equation can be obtained as

$$\frac{\partial (\rho h)}{\partial t} + \frac{\partial (\rho u_j h)}{\partial x_j} = \frac{Dp}{Dt} + \frac{\partial}{\partial x_j}\left(\frac{\lambda}{c_p}\nabla h\right) + \sum_{k=1}^{N} h_k \frac{\partial}{\partial x_j}\left[\left(\frac{\lambda}{c_p} - \rho D_k\right)\nabla Y_k\right], \tag{2.3}$$

where the enthalpy h is defined as

$$h = \sum_{k=1}^{N} Y_k h_k = \sum_{k=1}^{N} Y_k \int_0^T c_{p,k}(T) dT. \tag{2.4}$$

$c_{p,k}$ is the specific heat at constant pressure of each species, which itself is a function of the temperature. The temperature dependence of the specific heat coefficients for each species can be represented by a polynomial fit with coefficients which may be obtained from the CHEMKIN database [32].

If a low Mach number approximation is applied, the acoustic interactions and the work of viscous forces in the energy equation are neglected so that variables such as density, temperature and enthalpy are decoupled from variations in pressure, δp, about a specified background pressure field, p_0.

This leads to

$$\rho(p_0 + \delta p, s) \simeq \rho(p_0, s) \longrightarrow \left(\frac{\partial \rho}{\partial p}\right)_s \simeq 0, \tag{2.5}$$

which implies that the speed of sound is nearly infinite. Under this assumption, only p_0 is coupled to the thermodynamic variables. Therefore the equation of state becomes

$$p_0 = \rho \sum_{k=1}^{N} \frac{Y_k}{W_k} RT. \tag{2.6}$$

For open systems such as the bluff-body flame in this study, it is also assumed that p_0 is uniform and constant so that the material derivative of pressure in Eq. (2.3) reduces to

$$\frac{Dp}{Dt} \simeq \frac{Dp_0}{Dt} = 0. \tag{2.7}$$

For simplicity, it is common practice to adopt the unity Lewis number assumption for large-scale transport problems. Since the Lewis number is defined by

$$Le_k = \frac{\lambda}{\rho c_p D_k}, \tag{2.8}$$

where λ is the thermal diffusivity and D_k is the molecular diffusivity, this assumption means that all mass diffusivities are proportional to the thermal diffusivity.

Applying all the assumptions above to Eq. (2.3), one obtains the energy equation as

$$\frac{\partial(\rho h)}{\partial t} + \frac{\partial(\rho u_j h)}{\partial x_j} = \frac{\partial}{\partial x_j}\left(\rho D \frac{\partial h}{\partial x_j}\right). \tag{2.9}$$

2.1.2 Unsteady Reynolds-Averaged Simulation

The idea of Reynolds-averaging is to decompose an instantaneous flow field into time-averaged mean and fluctuating velocities. Accordingly, in RANS approaches only the mean flow properties are computed, whereas all scales of fluctuation motions are modelled.

The decomposition of an instantaneous variable $\phi(\mathbf{x}, t)$ into its mean $\langle\phi(\mathbf{x}, t)\rangle$ and the fluctuation

$$\phi^{fluc}(\mathbf{x}, t) = \phi(\mathbf{x}, t) - \langle\phi(\mathbf{x}, t)\rangle \tag{2.10}$$

is called the Reynolds decomposition. The mean value $\langle\phi(\mathbf{x}, t)\rangle$ is a time-averaged value which is defined by

$$\langle\phi(\mathbf{x}, t)\rangle \equiv \overline{\phi}(\mathbf{x}) = \lim_{T\to\infty} \frac{1}{T} \int_{t_0}^{t_0+T} \phi(\mathbf{x}, t)dt, \tag{2.11}$$

where T is an averaging time interval. The interval must be larger than the largest time scale of the fluctuations.

For unsteady flows, the URANS approach has been often employed and the mean velocity $\overline{u}(\mathbf{x}, t)$ is considered as an ensemble average defined by

$$\overline{u}(\mathbf{x}, t) = \lim_{N\to\infty} \frac{1}{N} \int_{n=1}^{N} u_n(\mathbf{x}, t), \tag{2.12}$$

where N is the number of flow realizations.

In density variation problems such as reacting flows, a density-weighted averaging called Favre-averaging is applied. Using Favre-averaging, an instantaneous velocity is decomposed into the density-weighted mean

$$\tilde{u} = \frac{\overline{\rho u}}{\overline{\rho}} \tag{2.13}$$

and the fluctuation

$$u'' = u - \tilde{u}. \tag{2.14}$$

Note that ($''$) is used in this study to denote the fluctuating part of a Favre-averaged variable in URANS.

Applying Favre-averaging to the governing equations in the previous section, the averaged governing equations are obtained as

$$\frac{\partial \overline{\rho}}{\partial t} + \frac{\partial (\overline{\rho}\widetilde{u}_j)}{\partial x_j} = 0, \tag{2.15}$$

$$\frac{\partial (\overline{\rho}\widetilde{u}_i)}{\partial t} + \frac{\partial (\overline{\rho}\widetilde{u}_i\widetilde{u}_j)}{\partial x_j} = -\frac{\partial \overline{p}}{\partial x_i} + \frac{\partial}{\partial x_j}\left[\mu\left(\frac{\partial \widetilde{u}_i}{\partial x_j} + \frac{\partial \widetilde{u}_j}{\partial x_i} - \frac{2}{3}\frac{\partial \widetilde{u}_l}{\partial x_l}\delta_{ij}\right)\right] - \frac{\partial \tau_{ij}^R}{\partial x_j}, \tag{2.16}$$

where $\tau_{ij}^R = \widetilde{\overline{\rho}u_i''u_j''} = \overline{\rho}(\widetilde{u_iu_j} - \widetilde{u}_i\widetilde{u}_j)$ are called the Reynolds stresses and must be closed.

A fundamental problem of classical turbulence modeling is to relate the Reynolds stresses to the mean flow quantities and their gradients in some physically plausible manner. One popular approach to model these is to adopt the eddy viscosity concept. It was originally proposed by Boussinesq [4], and assumes a linear constitutive relationship between the Reynolds stresses and mean strain-rate tensors:

$$\tau_{ij}^R = -2\mu_t\widetilde{S}_{ij} + \frac{2}{3}\overline{\rho}\widetilde{k}\delta_{ij}, \tag{2.17}$$

where k is the turbulent kinetic energy. The strain-rate-tensor is

$$\widetilde{S}_{ij} = \frac{1}{2}\left(\frac{\partial \widetilde{u}_i}{\partial x_j} + \frac{\partial \widetilde{u}_j}{\partial x_i}\right). \tag{2.18}$$

Analogous to the effect of molecular viscosity in the molecular momentum equation (Eq. (2.2)), the eddy viscosity characterizes the effect of turbulent eddies on the transfer and mixing of momentum. Based on dimensional analysis [69], the kinematic eddy viscosity can be estimated from the product of length and velocity scales of turbulent eddies as

$$\nu_t = l_t v_t. \tag{2.19}$$

Although there are many different types of eddy viscosity models, in general, the two-equation $k-\varepsilon$ model is widely chosen, where ε is the dissipation rate of k, i.e., the amount of k per mass and time which is converted into internal energy of the fluid by viscous work. In this $k-\varepsilon$ turbulence model, the length scale (l_t) and the velocity scale (v_t) are determined as

$$l_t \sim k^{2/3}/\varepsilon, \quad v_t \sim k^{1/2}. \tag{2.20}$$

Using the proportional constant C_μ, the turbulent viscosity is now calculated by

$$\mu_t = \overline{\rho} C_\mu \frac{\widetilde{k}^2}{\widetilde{\varepsilon}}. \tag{2.21}$$

The transport equations for k and ε read

$$\frac{\partial \overline{\rho}\widetilde{k}}{\partial t} + \frac{\partial \overline{\rho}\widetilde{u}_j\widetilde{k}}{\partial x_j} = \frac{\partial}{\partial x_j}\left[\left(\mu + \frac{\mu_t}{\sigma_k}\right)\frac{\partial \widetilde{k}}{\partial x_j}\right] + P_k - \overline{\rho}\widetilde{\varepsilon}, \tag{2.22}$$

$$\frac{\partial \overline{\rho}\widetilde{\varepsilon}}{\partial t} + \frac{\partial \overline{\rho}\widetilde{u}_j\widetilde{\varepsilon}}{\partial x_j} = \frac{\partial}{\partial x_j}\left[\left(\mu + \frac{\mu_t}{\sigma_\varepsilon}\right)\frac{\partial \widetilde{\varepsilon}}{\partial x_j}\right] + \frac{\varepsilon}{k}\left(C_{\varepsilon_1}P_k - C_{\varepsilon_2}\varepsilon\right), \tag{2.23}$$

where $P_k = 2\mu_t \widetilde{S}_{ij}\widetilde{S}_{ij}$ is the production rate of turbulent kinetic energy. All the model constants for the standard $k-\varepsilon$ model are listed in Table 2.1.

2.1.3 Large Eddy Simulation

In LES, all of the field variables are decomposed into resolved (grid) scale and subgrid-scale (SGS) parts. As illustrated in Figure 2.1, the resolved, large-scale field is related

C_μ	$C_{\varepsilon 1}$	$C_{\varepsilon 2}$	σ_k	σ_ε
0.09	1.44	1.92	1.0	1.3

Table 2.1: Standard $k-\varepsilon$ model constants.

to the instantaneous full-scale field through a grid-filtering operation denoted by $(\overline{\cdot})$, which is not a time-averaging or an ensemble-averaging operation but a spatial filtering that removes scales too small to be resolved by the simulation. The influence of the filtered-out small-scale motions is fed back into the resolved motion through the SGS model.

The governing equations in LES can be obtained by applying a spatial filter to the continuity, momentum and scalar transport equations. The spatial filter of a function $f = f(\mathbf{x}, t)$ is defined as its convolution with a filter function, G, according to

$$\overline{f}(\mathbf{x}, t) = \int f(\mathbf{x} - \mathbf{y}, t)\ \ G(\mathbf{y}, \overline{\mathbf{\Delta}}) d\mathbf{y}, \tag{2.24}$$

where $G(\mathbf{y}, \overline{\Delta})$ is a three-dimensional spatial filter kernel with a filter width $\overline{\Delta}$. For variable density flows, a Favre-filtered function is defined as

$$\widetilde{f}(\mathbf{x}, t) = \frac{1}{\overline{\rho}} \int \rho f(\mathbf{x} - \mathbf{y}, t) G(\mathbf{y}, \overline{\mathbf{\Delta}}) d\mathbf{y}, \tag{2.25}$$

where $\overline{\rho}$ is a filtered density field.

In the present work, a top-hat filter, based on a computational grid cell of volume ΔV, is employed. This filter corresponds to the *Schumann filter* [80], which is implicitly applied in finite-volume methods (FVM) by approximating the values at the cell center with the mean over the entire cell. The filter width $\overline{\Delta} = (\Delta x \Delta y \Delta z)^{1/3}$ is defined as a characteristic length of the cell. In the FVM framework, the governing equations, which are either filtered implicitly in LES or Reynolds-averaged in URANS, have the same forms but with different meanings, and hence need to be modelled differently.

The continuity and momentum equations in LES can then be written as

$$\frac{\partial \overline{\rho}}{\partial t} + \frac{\partial \overline{\rho} \widetilde{u}_j}{\partial x_j} = 0, \tag{2.26}$$

$$\frac{\partial \overline{\rho} \widetilde{u}_i}{\partial t} + \frac{\partial \overline{\rho} \widetilde{u}_i \widetilde{u}_j}{\partial x_j} = -\frac{\partial \overline{p}}{\partial x_i} + \frac{\partial}{\partial x_j} \left[\mu \left(\frac{\partial \widetilde{u}_i}{\partial x_j} + \frac{\partial \widetilde{u}_j}{\partial x_i} - \frac{2}{3} \frac{\partial \widetilde{u}_l}{\partial x_l} \delta_{ij} \right) \right] - \frac{\partial \tau_{ij}^{sgs}}{\partial x_j}. \tag{2.27}$$

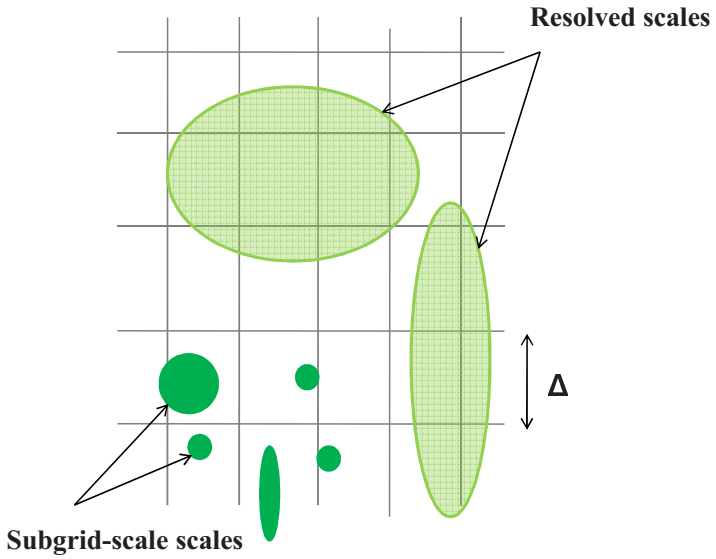

Figure 2.1: Resolved and unresolved subgrid scales for a given filter length $\overline{\Delta}$ when using the top-hat filter.

The unclosed SGS stresses in LES,

$$\tau_{ij}^{sgs} = \overline{\rho}\widetilde{u_i u_j} - \overline{\rho}\widetilde{u}_i\widetilde{u}_j, \tag{2.28}$$

must be modelled.

Following the energy cascade concept [69], in which energy is transferred from large scales to smaller and smaller scales where viscous dissipation takes place, the unresolved subgrid scales are primarily affected by viscous forces, dissipating turbulent kinetic energy from the resolved scales. The main role of a SGS-model is therefore to drain energy and to be dissipative. In gas kinetics theory, molecular agitation draws energy from the flow by way of molecular viscosity; the energy cascade mechanism is modelled by a term having a mathematical structure similar to that of molecular diffusion, but in which the molecular viscosity is replaced by a SGS viscosity μ_{sgs}. To author's knowledge, the most popular SGS model is the Smagorinsky model [82], a zero-equation eddy viscosity model based on a simple mixing length concept.

In the Smagorinsky model, the SGS stresses are modelled as

$$\tau_{ij}^{sgs} = -2\mu_{sgs}\widetilde{S}_{ij} + \frac{1}{3}\tau_{kk}^{sgs}\delta_{ij}, \tag{2.29}$$

where $\widetilde{S}_{ij}$ is the strain-rate-tensor similar to Eq. (2.18). The SGS viscosity following the Smagorinsky model reads

$$\mu_{sgs} = \overline{\rho}(C_S\overline{\Delta})^2|\widetilde{S}|, \tag{2.30}$$

where $|\widetilde{S}| = (2\widetilde{S}_{ij}\widetilde{S}_{ij})^{1/2}$. While the model constant C_S is commonly taken between 0.1 and 0.2 depending on the flow type [76], Deardorff [18] suggested $C_S = 0.1$ for plane channel flows and this value has been used for bluff-body flows in many recent works [10, 75, 86].

As mentioned above, the Smagorinsky model depends on the rate of the strain for the turbulent velocity scale and the filter width for the turbulent length scale. In particular, the model constant C_S is an ad-hoc adjustment of turbulent length scale which cannot be universal for different types of turbulent flows. Germano *et al.* [23] proposed a dynamic procedure to overcome this weakness of the Smagorinsky model, in which C_S is calculated dynamically at every grid point in space and at every time step [23]. However, the dynamic procedure requires longer calculation time and may result in large negative values for C_S which lead to numerical instability [76]. In this work, therefore, the Smagorinsky model with $C_S = 0.1$ is used for the bluff-body flows.

2.2 Governing Equations of Chemical Reactions

2.2.1 Conserved Scalar: Mixture Fraction Variable

Technical combustors may be very complex devices. In general the underlying physical process may be simplified to the mixing of fuel with an oxidizer. Therefore, a two

feed system, as shown schematically in Figure 2.2, is representative for many technical applications. This is even true for devices where an additional inlet recirculating fuel gas or a hot pilot gas stream is fed into the reaction zone, because the recirculated exhaust gases are simply the products of the given fuel and oxidizer.

For such a two feed system it is common to describe the mixing state by the mixture fraction Z. Assuming that every atom of the two mass streams, where $\dot{m}_1$ is the fuel stream and $\dot{m}_2$ is the oxidizer stream, could be marked with a conserved property such that the local mass of the atoms of the two streams, $\dot{m}_{1,l}$ and $\dot{m}_{2,l}$, is known at any time and location, then the mixture fraction may be defined as

$$Z = \frac{\dot{m}_{1,l}}{\dot{m}_{1,l} + \dot{m}_{2,l}}. \tag{2.31}$$

This dimensionless variable states that the mixture fraction represents the local instantaneous mass of the fuel stream atoms in the mixture. The mixture fraction is then bounded by $Z = 1$ in the pure fuel stream and by $Z = 0$ in the pure oxidizer stream. Following Bilger [3], the local value of any conserved scalar β in the mixture is then given by

$$\beta = Z\beta_1 + (1 - Z)\beta_2, \tag{2.32}$$

where β_1 and β_2 are the values of the conserved scalar in the fuel stream and in the oxidizer stream respectively.

If we rearrange Eq. (2.32), one gets the following fundamental equation for the mixture fraction

$$Z = \frac{\beta - \beta_2}{\beta_1 - \beta_2}. \tag{2.33}$$

It should be noted that any conserved scalar can be used for β to derive the mixture fraction Z. For instance, in a non-reacting mixing system any measured chemical species can be used. However, in a chemically reacting system it is not a trivial task to relate the chemical species to the mixture fraction, because species are not conserved during chemical reactions. Other scalars have to be used instead. One

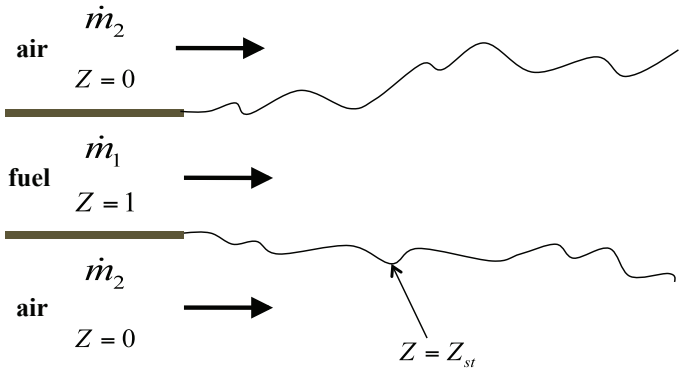

Figure 2.2: Two feed system of fuel and oxidizer. 1: fuel stream, 2: oxidizer stream.

possibility is the mass fraction of the elements, which are conserved even during combustion.

The mass fraction Z of an element α is related to the mass fraction Y_k of species k through

$$Z_\alpha = \frac{m_\alpha}{m} = \sum_{k=1}^{N} \frac{a_{k\alpha} W_\alpha}{W_k} Y_k, \tag{2.34}$$

where $a_{k\alpha}$ is the number of atoms of element α in the molecular of species k. W_α and W_k are the molecular weights of the elements α and species k respectively. In principle, any element may be used as a conserved scalar to compute the mixture fraction. However, the value of the mixture fraction may be different depending on the selected element because species in a reacting system may diffuse at different rates. This problem is known as preferential or differential diffusion. Here, the mixture fraction is defined on the basis of the sum of all fuel elements in the fuel stream. Thus, for a pure hydrocarbon fuel, the fuel element mass fraction is defined as the sum of the element mass fractions of carbon and hydrogen:

$$Z_F = \sum_{\alpha=1}^{M} Z_{\alpha,F} = Z_C + Z_H, \tag{2.35}$$

Inserting Eq. (2.35) into Eq. (2.33) gives the mixture fraction as a function of the fuel element mass fraction

$$Z = \frac{Z_F - Z_{F,2}}{Z_{F,1} - Z_{F,2}}. \tag{2.36}$$

In general, there is no fuel in the oxidizer stream of a non-premixed combustion flame, so $Z_{F,2} = 0$. Furthermore, in the pure fuel stream, the element mass fraction of the fuel is equal to the mass fraction of the fuel species, i.e., $Z_{F,1} = Y_{F,1}$. Eq. (2.36) reduces then to

$$Z = \frac{Z_F}{Z_{F,1}} = \frac{Z_F}{Y_{F,1}}. \tag{2.37}$$

Note that once the elements on which the mixture fraction is defined are chosen, the mixture fraction defines uniquely the mixing state. In this work the mixture fraction is always based on all elements of the fuel as given by Eq. (2.37).

An important quantity for the analysis of combustion is the value of the mixture fraction at stoichiometric conditions. It may be easily derived if one represents the chemistry by the following global one-step reaction, where fuel F and oxygen O_2 react to form a single product P,

$$\nu'_F F + \nu'_{O_2} O_2 \rightarrow \nu''_P P, \tag{2.38}$$

where ν'_F, ν'_{O_2} and ν''_P are the stoichiometric coefficients. The consumption of fuel is strongly coupled to the consumption of oxygen, as given by the following equation:

$$\frac{dn_F}{\nu'_F} = \frac{dn_{O_2}}{\nu'_{O_2}}, \tag{2.39}$$

where n_k is the number of moles of species k. With $m_k = n_k W_k$, which relates the number of moles of species k to its mass m_k, and taking into account that the total mass of the system is constant, the following equation is obtained:

$$\frac{dY_F}{\nu'_F W_F} = \frac{dY_{O_2}}{\nu'_{O_2} W_{O_2}}. \tag{2.40}$$

If the equation above is integrated from the unburned state with index u to an intermediate state during reaction, the result is

$$\frac{Y_F - Y_{F,u}}{\nu'_F W_F} = \frac{Y_{O_2} - Y_{O_2,u}}{\nu'_{O_2} W_{O_2}}. \tag{2.41}$$

Introducing the stoichiometric mass ratio

$$s = \left(\frac{Y_{O_2,u}}{Y_{F,u}}\right) = \frac{\nu'_{O_2} W_{O_2}}{\nu'_F W_F}, \tag{2.42}$$

which defines the mass of oxidizer required to burn a unit mass of fuel, Eq. (2.41) may be rewritten as

$$sY_F - Y_{O_2} = sY_{F,u} - Y_{O_2,u}. \tag{2.43}$$

As the intermediate burning state is arbitrary and the unburned state is a conserved property, Eq. (2.43) defines a new conserved scalar, which is known as Shavb-Zel'dovich coupling variable

$$\beta = Y_F - Y_{O_2}/s. \tag{2.44}$$

Inserting Eq. (2.44) into Eq. (2.33) and again taking into account that there is no fuel in the oxidizer stream and no oxygen in the fuel stream, i.e., $Y_{F,2} = 0$ and $Y_{O_2,1} = 0$, we obtain another relation to derive the mixture fraction:

$$Z = \frac{Y_F - Y_{O_2}/s + Y_{O_2,2}/s}{Y_{F,1} + Y_{O_2,2}/s}, \tag{2.45}$$

where $Y_{F,1}$ is the initial fuel mass fraction in the fuel stream and $Y_{O_2,2}$ is the initial oxygen mass fraction in the oxidizer stream. Eq. (2.45) is a simple expression to derive the mixture fraction. It is exact if the chemistry is complete and may be represented by a single global reaction step as given by Eq. (2.38), which is the case when the mass fractions of intermediate species are negligible as compared to the mass fractions of the stable species. For a stoichiometric mixture fraction, $sY_F = Y_{O_2}$ holds and the stoichiometric mixture fraction can be easily deduced from Eq. (2.45) and obtained as

$$Z_{st} = \frac{1}{1 + sY_{F,1}/Y_{O_2,2}} \quad . \tag{2.46}$$

2.2.2 Conserved Scalar Equation

All of the chemical reaction models in this work are based on the concept of the mixture fraction. A transport equation for the mixture fraction may be derived from an appropriate linear combination of the transport equations of the species mass fractions. Assuming that species obey Fick's law of diffusion, the mass fraction transport equation for species k can be written as

$$\frac{\partial \rho Y_k}{\partial t} + \frac{\partial \rho u_j Y_k}{\partial x_j} = \frac{\partial}{\partial x_j}\left(\rho D_k \frac{\partial Y_k}{\partial x_j}\right) + \dot{\omega}_k. \tag{2.47}$$

Using Eq. (2.34), the conserved scalar equation can be formally derived by summing up the species mass fraction equations in such a way that the reaction source term cancels:

$$\frac{\partial \rho Z_\alpha}{\partial t} + \frac{\partial \rho u_j Z_\alpha}{\partial x_j} = \frac{\partial}{\partial x_j}\left(\rho D \frac{\partial Z_\alpha}{\partial x_j}\right), \tag{2.48}$$

where the unity Lewis number assumption is employed. Eq. (2.48) has no chemical source terms since

$$\sum_{k=1}^{N} a_{k\alpha}\dot{\omega}_k = 0, \tag{2.49}$$

which shows that the element mass fraction is conserved during the combustion. As the mixture fraction itself is a conserved scalar as well, its transport equation can be written as

$$\frac{\partial \rho Z}{\partial t} + \frac{\partial \rho u_j Z}{\partial x_j} = \frac{\partial}{\partial x_j}\left(\rho D \frac{\partial Z}{\partial x_j}\right). \tag{2.50}$$

Therefore, in the local flow field, the mixture fraction can uniquely define the mixing state.

In the FVM framework, as shown earlier, the governing equations, which are either filtered implicitly in LES or Reynolds-averaged in URANS, have the same forms but

different meanings. This also applies to Eq. (2.50), the conserved scalar equation, and the Reynolds-averaged or filtered the conserved scalar equation is obtained as

$$\frac{\partial(\overline{\rho}\widetilde{Z})}{\partial t} + \frac{\partial(\overline{\rho}\widetilde{u}_j\widetilde{Z})}{\partial x_j} = \frac{\partial}{\partial x_j}\left(\rho D\frac{\partial\widetilde{Z}}{\partial x_j}\right) - \frac{\partial M_j}{\partial x_j}, \tag{2.51}$$

where the fluctuation of the diffusivity is ignored [62].

The unclosed term,

$$M_j = \overline{\rho}\widetilde{u_j Z} - \overline{\rho}\widetilde{u}_j\widetilde{Z}, \tag{2.52}$$

can be interpreted as the turbulent scalar fluxes in URANS or the SGS scalar fluxes in LES; both must be modelled. The eddy diffusivity concept is employed for both URANS and LES to model M_j. In URANS the turbulent scalar fluxes are modelled as

$$M_j = -\overline{\rho}D_t\frac{\partial\widetilde{Z}}{\partial x_j} = -\frac{\mu_t}{Sc_t}\frac{\partial\widetilde{Z}}{\partial x_j}, \tag{2.53}$$

where $D_t = \nu_t/Sc_t$ is the turbulent diffusivity and the turbulent Schmidt number is set to $Sc_t = 0.4$ in the present study. Using this model, one may obtain the Reynolds-averaged conserved scalar equation in URANS as

$$\frac{\partial(\overline{\rho}\widetilde{Z})}{\partial t} + \frac{\partial(\overline{\rho}\widetilde{u}_j\widetilde{Z})}{\partial x_j} = \frac{\partial}{\partial x_j}\left[\overline{\rho}\left(D + D_t\right)\frac{\partial\widetilde{Z}}{\partial x_j}\right]. \tag{2.54}$$

In a similar way, the SGS scalar fluxes in LES are modelled as

$$M_j = -\overline{\rho}D_{sgs}\frac{\partial\widetilde{Z}}{\partial x_j} = -\frac{\mu_{sgs}}{Sc_{sgs}}\frac{\partial\widetilde{Z}}{\partial x_j}, \tag{2.55}$$

where $D_{sgs} = \nu_{sgs}/Sc_{sgs}$ is the SGS diffusivity and the SGS Schmidt number is also set to $Sc_{sgs} = 0.4$. Finally the filtered conserved scalar equation in LES is written as

$$\frac{\partial(\overline{\rho}\widetilde{Z})}{\partial t} + \frac{\partial(\overline{\rho}\widetilde{u}_j\widetilde{Z})}{\partial x_j} = \frac{\partial}{\partial x_j}\left[\overline{\rho}\left(D + D_{sgs}\right)\frac{\partial\widetilde{Z}}{\partial x_j}\right]. \tag{2.56}$$

2.2.3 Combustion models

Burke-Shumann Solution

The simplest and probably the oldest description of the reacting structure of a diffusion flame is given by Burke and Shumann [7]. This model may be reformulated in terms of the mixture fraction, and it is known as the Burke-Shumann solution. The Burke-Shumann solution is a limiting description, which is based on the following three assumptions:

1. the chemistry is described by a single-step reaction.
2. the chemistry is infinitely fast.
3. the chemistry is complete, i.e., no backward reaction is possible.

The second and the third assumption imply that reactants cannot coexist at the same place and the same time, and that the reaction zone is infinitely thin, i.e., a reaction sheet separates the two reactants. For a single-step reaction,

$$\nu'_F F + \nu'_{O_2} O_2 \rightarrow \nu''_P P. \tag{2.57}$$

It is now possible to derive the species distribution in mixture fraction space. Following the assumptions above, it is obvious that in regions where the local mixture fraction is less than the stoichiometric value Z_{st} all the fuel is consumed $Y_{F,BS} = 0$ and one has an excess amount of oxygen. In what follows, the index BS stands for the fully burned state. By analogy, in the fuel rich region, i.e., $Z > Z_{st}$, all the oxygen is consumed, $Y_{O_2,BS} = 0$, and fuel excess exists.

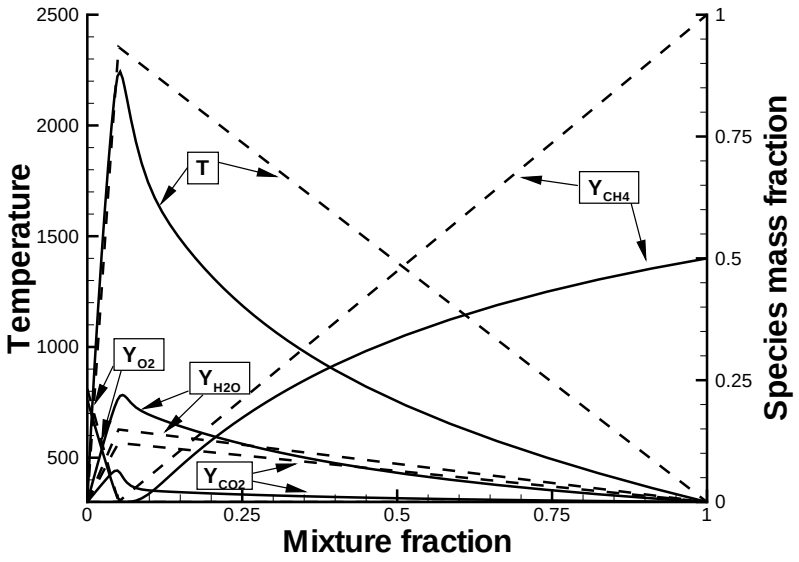

Figure 2.3: The Burke-Shumann solution (dashed) and the chemical equilibrium model (solid).

The linear composition can be obtained as follows.

$$Y_{F,BS} = \begin{cases} Y_{F,1}\left(\frac{Z-Z_{st}}{1-Z_{st}}\right) & Z \geq Z_{st} \\ 0 & Z \leq Z_{st} \end{cases} \tag{2.58}$$

$$Y_{O_2,BS} = \begin{cases} 0 & Z \geq Z_{st} \\ Y_{O_2,2}\left(1-\frac{Z}{Z_{st}}\right) & Z \leq Z_{st} \end{cases} \tag{2.59}$$

$Y_{F,1}$ is the fuel mass fraction at the fuel stream, and $Y_{O_2,2}$ is the oxygen mass fraction at the oxidizer stream, and Z_{st} is the stoichiometric mixture fraction.

Chemical Equilibrium Model

At high temperatures, combustion does not proceed to completion, and some reactions occur in the reverse direction. When the rate of reverse reaction equals the rate of

forward reaction, chemical equilibrium is reached. The chemical equilibrium model assumes that chemical equilibrium prevails at every point, which relaxes the constraint of complete combustion in the Burke-Shumman solution. The chemical equilibrium composition and temperature of the flame can be calculated as a function of the mixture fraction based on the Gibbs free energy [85]. The detailed chemical reactions follow the GRI-Mech 2.11 [5] and STANJAN software [72] is used to calculate the thermo-chemical values. Chemical reactions and related coefficients are tablized in Appendix B.

As shown in Figure 2.3, deviations exists between the Burke-Shumann solution and the chemical equilibrium model due to incomplete combustion. The chemical equilibrium model is able to include the intermediate species and the predicted peak temperature is lower than that of the Burke-Shumann solution due to the inclusion of chemical dissociation, incomplete combustion and the formation of radicals. It should be noted, however, that for more complicated reacting mixtures, not all the species may reach chemical equilibrium and then the model may lead to the large deviations from measurements. Furthermore, in the chemical equilibrium model any interaction between turbulence and chemical reaction is neglected.

Steady Laminar Flamelet Model

The steady laminar flamelet model has been successfully used during the last decades since it has both the advantage of decoupling the flow field and chemical kinetics calculations and the ability to handle detailed chemical reactions.

In the laminar flamelet theory, a flame can be viewed as an ensemble of thin locally one-dimensional structures embedded within the flow field. Physically, the flame structure is considered locally one-dimensional and only depends on time and the coordinate normal to the flame front. It is now possible to introduce a coordinate system attached to a surface element of constant mixture fraction and replace the coordinate perpendicular to the surface of the sheet-like element by the mixture fraction.

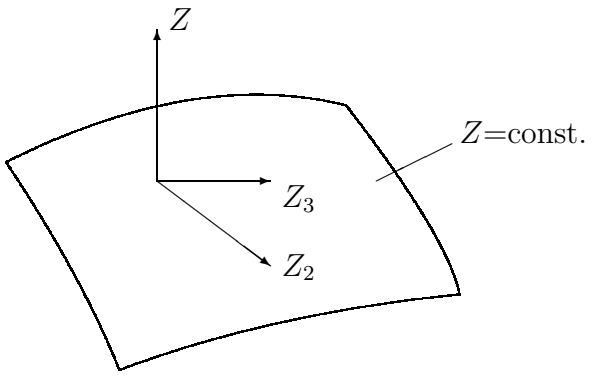

Figure 2.4: Coordinate system attached to a Z iso-surface.

Inherent in this formulation is the assumption that there is just one direction of large mixture fraction gradient, which is correct if curvature effects may be neglected [15].

By definition, the coordinate Z is locally normal to the iso-surface of the mixture fraction shown in Figure 2.4. With the unity Lewis number assumption and neglecting radiation heat transfer, the transformed equations for the species mass fractions and temperature at steady state are written as

$$\begin{aligned} \frac{\chi}{2}\left(\frac{\partial^2 Y_k}{\partial Z^2}\right) + \frac{\dot{\omega}_k}{\rho} &= 0, \\ \frac{\chi}{2}\left(\frac{\partial^2 T}{\partial Z^2}\right) - \frac{1}{\rho c_p}\sum_{k=1}^{N} h_k \dot{\omega}_k, &= 0, \end{aligned} \tag{2.60}$$

where χ is the instantaneous scalar dissipation rate. The scalar dissipation rate in the flamelet equations is defined by

$$\chi = 2D\left(\frac{\partial Z}{\partial x_j}\right)^2. \tag{2.61}$$

The influence of the scalar dissipation rate χ on the structure of diffusion flames was extensively discussed by Peters [62]. The scalar dissipation rate describes the influence

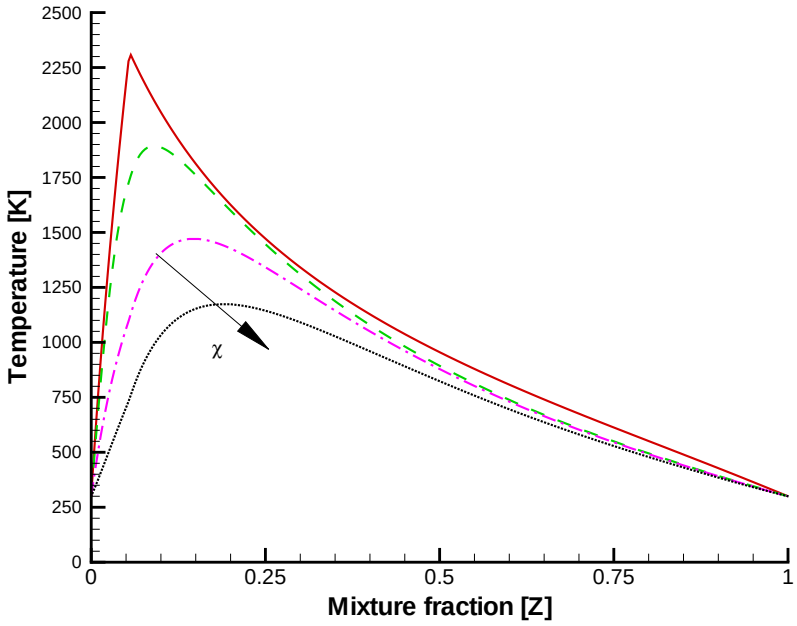

Figure 2.5: Temperature profile changes according to the increase of the scalar dissipation rate in the steady laminar flamelet solutions.

of the flow field on the laminar flame structure and is an essential non-equilibrium parameter since it measures the degree of the departure from chemical equilibrium. The scalar dissipation rate is commonly expressed as

$$\chi = \chi_{st} f(Z), \tag{2.62}$$

where χ_{st} is the scalar dissipation rate at stoichiometric mixture. The functional dependence on the mixture fraction is expressed by the log function [67]

$$f(Z) = \frac{Z^2 \, lnZ}{Z_{st}^2 \, lnZ_{st}}, \tag{2.63}$$

where Z_{st} is the stoichiometric mixture fraction. It is common practice to ignore the fluctuations of the scalar dissipation rate since they are very small in reactions [14].

Flamelet profiles with scalar dissipation rate corresponding to the mean value $\widetilde{\chi}$, which is found locally in the turbulent flows, are therefore used. The instantaneous scalar dissipation rate can be expressed by

$$\chi = \frac{\widetilde{\chi}}{\int_0^1 f(Z)\widetilde{P}(Z)dZ} f(Z) \tag{2.64}$$

The solutions from the steady laminar flamelet equations depend on the mixture fraction and the scalar dissipation rate, i.e., $Y_k = Y_k(Z, \chi)$. In principle, both variables Z and χ are instantaneous quantities and their statistical distribution needs to be considered in order to calculate the mean values of thermo-chemical compositions such as temperature and the species mass fractions. Therefore, knowing the joint Favre probability density function $\widetilde{P}(Z, \chi)$ of Z and χ is required to obtain the mean value.

$$\widetilde{Y_k} = \int_0^1 \int_0^\infty Y_k(Z, \chi)\widetilde{P}(Z, \chi)d\chi dZ. \tag{2.65}$$

To calculate this integral, statistical independence of Z and χ is assumed; i.e., $\widetilde{P}(Z, \chi) \approx \widetilde{P}(Z)\widetilde{P}(\chi)$. Though different approaches exist in the literature for both PDFs, it is common practice, as mentioned earlier, to neglect the small fluctuation of the scalar dissipation rate [14]. Therefore, the Favre-averaged species mass fraction can be integrated by,

$$\widetilde{Y_k} = \int_0^1 Y_k(Z, \widetilde{\chi})\widetilde{P}(Z)dZ. \tag{2.66}$$

Eq. (2.60) in the steady laminar flamelet model can be shown to be one-dimensional ordinary differential equations (ODEs). In the solution procedure of these ODEs, equations are discretized in mixture fraction space by finite differences and then solved with boundary condition at $Z = 0$ and $Z = 1$. The two-point boundary value solver (TWOPNT), which is based on a modified damped Newton algorithm [25], is used. The detailed chemical reactions follow the GRI-Mech 2.11 [5], and the CHEMKIN-II package [32] is utilized to deal with the chemical kinetics and thermodynamic

relations. As reviewed in Peters [62], the temperature is lowered by increasing the scalar dissipation rate. Figure 2.5 presents similar changes in the temperature profiles obtained from the steady laminar flamelet solver developed in this study. When the scalar dissipation approaches zero, which means that the influence of flow gets smaller, the local composition comes closer to the chemical equilibrium profile.

2.2.4 Presumed PDF Approach

The probability density function (PDF) completely characterizes a random variable and it serves to represent a probability distribution in terms of integrals. As mentioned earlier, the presumed β-function PDF, which is parameterized by the mean and the variance, is used to integrate the mean temperature and the species mass fractions. The presumed β-function PDF is written as

$$P(Z) = \frac{Z^{a-1}(1-Z)^{b-1}}{\int_0^1 Z^{a-1}(1-Z)^{b-1}dZ}, \tag{2.67}$$

and

$$a = \widetilde{Z}\gamma, \qquad b = (1-\widetilde{Z})\gamma,$$

$$\gamma = \frac{\widetilde{Z}(1-\widetilde{Z})}{\sigma} - 1,$$

where $\sigma = \widetilde{Z''^2}$ is for URANS and $\sigma = \widetilde{Z'^2}$ is for LES. Some shapes of the β-function PDF are presented in Figure 2.6.

The numerical integration of the β-function PDF encounters mainly two difficulties. One is a singularity problem at either the oxidizer side ($Z = 0$) or the fuel side ($Z = 1$), depending on the β-function PDF parameters, and the other is a overflow problem taking place when the PDF parameters are sufficiently large [9, 41, 48]. These difficulties in the numerical integration are addressed by following treatments

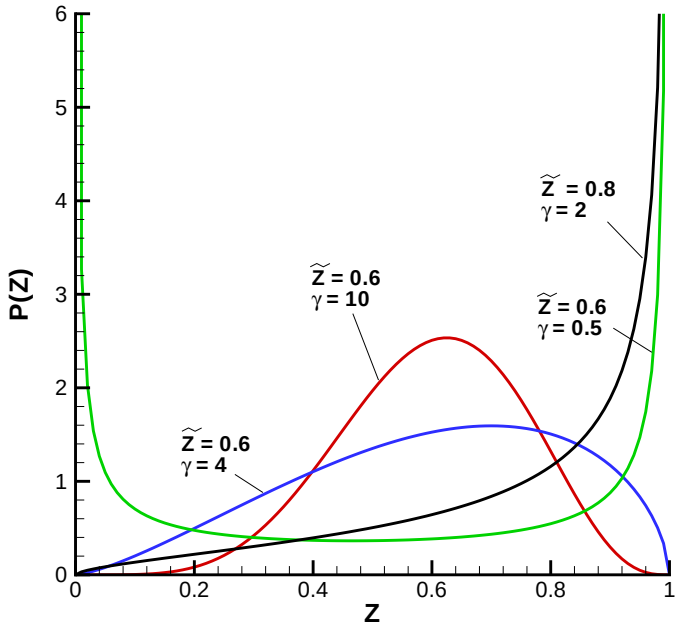

Figure 2.6: Shapes of the β-function PDF for different $\widetilde{Z}$ and γ.

suggested by Chen *et al.* [9] and others [46, 48]. Firstly, both the extreme fuel and oxidizer only cases are dealt with by applying a δ-function:

$$\begin{aligned}
\widetilde{\phi} &\approx \phi(Z=0) \qquad \text{if } a<1 \text{ and } a<b, \\
\widetilde{\phi} &\approx \phi(Z=1) \qquad \text{if } a>b \text{ and } b<1, \\
\widetilde{\phi} &\approx \frac{1}{2}(\phi(Z=0)+\phi(Z=1)) \qquad \text{if } a<1 \text{ and } b<1.
\end{aligned}$$

Secondly, the over-flow problem is avoided through clipping the large value between a and b. Then, the parameters remain under a certain large value (here, 500) while maintaining the ratio a/b.

Using the conserved-scalar formalism and the presumed PDF approach, the mean values of the thermo-chemical variables are obtained by PDF-weighted integration of

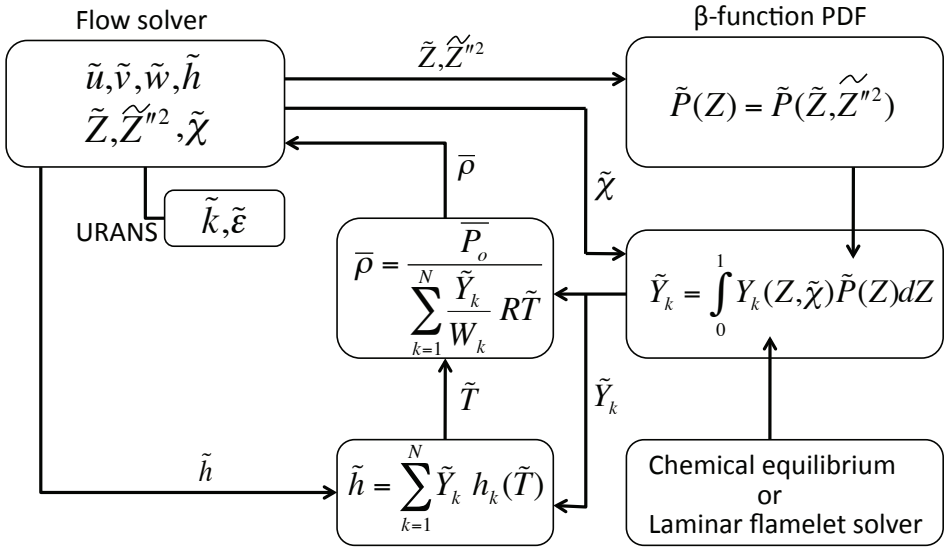

Figure 2.7: Code structure of the present study.

the local values;

$$\widetilde{Y}_k = \int_0^1 Y_k(Z)\widetilde{P}(Z)dZ, \tag{2.68}$$

where $\widetilde{P}(Z)$ describes the local mixing state. As introduced above, the presumed $\beta-$function PDF is adopted in this study.

The simulation flow chart is presented in Figure 2.7 in order to explain how the flow field is coupled with the chemical reaction. It is clear that there is the benefit of using the conserved scalar formalism because it separates the chemical reactions from the flow solver. It should be noted that only the density needs to be updated using the species mass fraction and mean temperature. In the chart, the PDF-weighted integration for the mean species mass fraction must be performed for every iteration, every grid cell, and for all chemical species. This could potentially require a prohibitive amount of computational time. For efficiency, the integration in this study is calculated prior to the main simulation using a separate code. In this separate code,

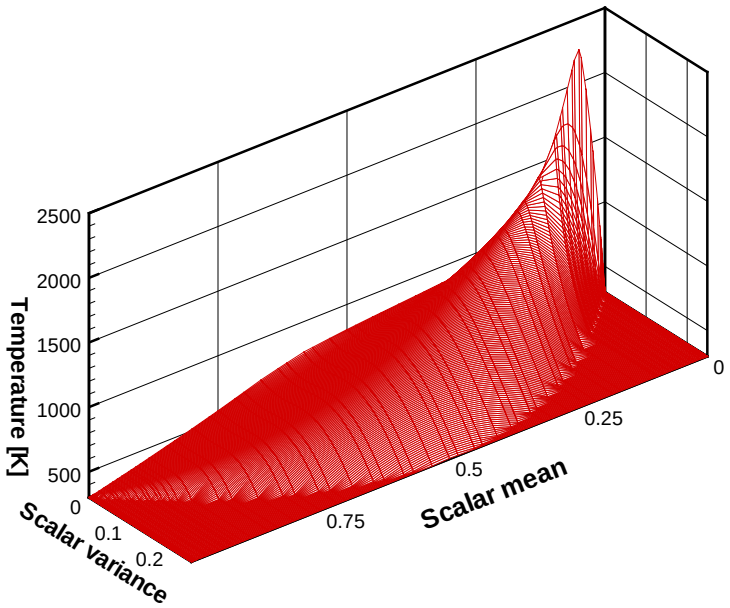

Figure 2.8: A lookup-table of chemical equilibrium model.

the scalar mean and its variance are discretized over their ranges of possible values. Using the trapezoidal rule [70], all integrations are performed and results are stored in look-up table files. The procedure is summarized as follows.

1. Generate local thermo-chemical variable profiles by executing either the chemical equilibrium model or the steady laminar flamelet model.
2. Construct $\beta-$function PDF with possible scalar mean and variance values.
3. Integrate Eq. (2.68) using the combustion data and the PDF data.

The size of the look-up table is (# scalar mean $\times$ # scalar variance)=(100 $\times$ 100). This table size was determined to give reasonable accuracy in the interpolation. For the steady laminar flamelet model which is a function of the scalar dissipation rate, a total of thirteen look-up tables for the steady laminar flamelet model were made

using scalar dissipation rates from 0 to 40. The functional dependency on the scalar mean (mixture fraction) is considered, as mentioned above, a log-relation.

A snapshot of the look-up table, whose the temperature is already integrated using the $\beta-$function PDF, is shown in Figure 2.8. Note that the mean temperature is not obtained through interpolation in this study, though. Given the scalar mean and the variance, the mean species mass fractions in this study are simply interpolated bilinearly or trilinearly inside the flow solver. The equilibrium model look-up table involves the scalar mean and the scalar variance only, so mean values are obtained by bilinear interpolation. The laminar flamelet model look-up table contains the scalar dissipation rate as well, so the values are calculated using the trilinear interpolation. Once the mean species mass fraction is obtained from the procedure above, the mean temperature is calculated through Eq. (2.4) in conjunction with the enthalpy obtained by solving the energy equation (Eq. (2.9)).

Chapter 3

Scalar variance and scalar dissipation rate modelling

Using the conserved scalar formalism, the local mixing state is described by a presumed $\beta-$function PDF, the accuracy of which relies heavily on the accuracy of the scalar mean and the scalar variance. Therefore, it is natural to seek a way to improve the accuracy of the $\beta-$function PDF and so our interest moves to how to predict the scalar mean and the variance accurately.

For the scalar mean, it has been common practice for both URANS and LES to solve its own transport equation, whose turbulent or SGS scalar fluxes are closed by the eddy-diffusivity concept. However, URANS and LES use quite different approaches to obtain the scalar variance, mainly due to computational cost considerations. Therefore, the present study focuses on the modelling of the scalar variance and the scalar dissipation rate. In this matter, existing methodologies for URANS and LES are reviewed first and a new approach will be proposed later.

3.1 Scalar variance and scalar dissipation rate modelling in URANS

3.1.1 Scalar variance modelling

The Favre-averaged mean of the scalar (mixture fraction) can be obtained using the first moment:

$$\widetilde{Z} = \int Z\widetilde{P}(x)dx. \tag{3.1}$$

The variance of the scalar can be obtained using the second moment:

$$\begin{aligned} \widetilde{Z''^2} &= \int (Z-\widetilde{Z})^2\widetilde{P}(x)dx \\ &= \widetilde{Z^2} - \widetilde{Z}^2, \end{aligned} \tag{3.2}$$

where $Z'' = Z - \widetilde{Z}$ is the fluctuation part of the scalar in this study according to the Reynolds decomposition (i.e., time-averaging).

Given the definition of the scalar variance in Eq. (3.2), the scalar variance equation can be obtained by manipulating Eq. (2.54) as

$$\begin{aligned} \frac{\partial\overline{\rho}\widetilde{Z''^2}}{\partial t} + \frac{\partial\overline{\rho}\widetilde{u}_j\widetilde{Z''^2}}{\partial x_j} &= -\frac{\partial}{\partial x_j}\left(\overline{\rho}\widetilde{u_j''Z''^2}\right) - 2\overline{\rho}\widetilde{u_j''Z''}\frac{\partial\widetilde{Z}}{\partial x_j} \\ &\quad + \frac{\partial}{\partial x_j}\left(\overline{\rho}D\frac{\partial\widetilde{Z''^2}}{\partial x_j}\right) - 2\overline{\rho}D\frac{\partial\widetilde{Z''}}{\partial x_j}\frac{\partial\widetilde{Z''}}{\partial x_j}. \end{aligned} \tag{3.3}$$

The unclosed terms are closed using the eddy diffusivity concept [62]:

$$\widetilde{u_j''Z''} = -\overline{\rho}D_t\frac{\partial\widetilde{Z}}{\partial x_j}, \tag{3.4}$$

$$\widetilde{u_j''Z''^2} = -\overline{\rho}D_t\frac{\partial\widetilde{Z''^2}}{\partial x_j}. \tag{3.5}$$

In the semi-closed form, the scalar variance equation can be written as

$$\frac{\partial \overline{\rho}\widetilde{Z''^2}}{\partial t} + \frac{\partial \overline{\rho}\widetilde{u}_j\widetilde{Z''^2}}{\partial x_j} = \frac{\partial}{\partial x_j}\left[\overline{\rho}\left(D + D_t\right)\frac{\partial \widetilde{Z''^2}}{\partial x_j}\right] + 2\overline{\rho}D_t\left(\frac{\partial \widetilde{Z}}{\partial x_j}\right)^2 - \overline{\rho}\widetilde{\chi}, \tag{3.6}$$

where the scalar dissipation rate,

$$\widetilde{\chi} = 2D\frac{\partial \widetilde{Z''}}{\partial x_j}\frac{\partial \widetilde{Z''}}{\partial x_j}, \tag{3.7}$$

needs to be closed. It should be noted that the scalar variance and its dissipation rate must be solved via a coupled system.

3.1.2 Scalar dissipation rate modelling

The scalar dissipation rate in URANS has been commonly modelled through an algebraic model assuming that the ratio, R_τ, of mechanical and scalar time scales is constant. The mechanical time and length scales in URANS can be written as

$$\tau_u \sim \widetilde{k}/\widetilde{\varepsilon}, \tag{3.8}$$

$$\ell_u \sim \widetilde{k}^{3/2}/\widetilde{\varepsilon}. \tag{3.9}$$

By dimensional analysis [69], the scalar time and length scales can be written as

$$\tau_s \sim \widetilde{Z''^2}/\widetilde{\chi}, \tag{3.10}$$

$$\ell_s \sim \widetilde{Z''^2}^{3/2}\widetilde{\varepsilon}^{1/2}/\widetilde{\chi}^{3/2}. \tag{3.11}$$

Setting $\tau_u \simeq \tau_s$ or $\ell_u \simeq \ell_s$ gives the algebraic model:

$$R_\tau = \frac{\widetilde{k}/\widetilde{\varepsilon}}{\widetilde{Z''^2}/\widetilde{\chi}} \rightarrow \widetilde{\chi} = R_\tau\frac{\widetilde{\varepsilon}}{\widetilde{k}}\widetilde{Z''^2}, \tag{3.12}$$

which describes the scalar dissipation rate by relating the scalar variance linearly to the large eddy turnover time. $R_\tau = 2.0$ has been commonly used according to the experiment of Beguier *et al.* [2]. As mentioned earlier, it has been reported that the ratio R_τ is not always constant in many different turbulent flows but there is evidence to believe that the time scale ratio varies for different flows [11, 59]. Therefore, a transport equation for the scalar dissipation rate is required.

Several transport equations for the scalar dissipation rate have been published in the literature and a summary of the existing models is provided in the study by Sanders and Gokalp [78]. In the present study, the equation proposed by Jones and Musonge [31] is introduced as

$$\begin{aligned}\frac{\partial \overline{\rho}\widetilde{\chi}}{\partial t} + \frac{\partial \overline{\rho}\widetilde{u}_j\widetilde{\chi}}{\partial x_j} &= \frac{\partial}{\partial x_j}\left[\left(\frac{\mu}{Sc} + \frac{\mu_t}{Sc_t}\right)\frac{\partial \widetilde{\chi}}{\partial x_j}\right] - C_1\overline{\rho}\frac{\widetilde{\chi}^2}{\widetilde{Z''^2}} - C_2\overline{\rho}\frac{\widetilde{\varepsilon}}{\widetilde{k}}\widetilde{\chi} \\ &\quad - C_3\overline{\rho}\frac{\widetilde{\varepsilon}}{\widetilde{k}}\underbrace{\widetilde{u_j''Z''}\frac{\partial \widetilde{Z}}{\partial x_j}}_{-P_f} - C_4\overline{\rho}\frac{\widetilde{\chi}}{\widetilde{k}}\underbrace{\widetilde{u_i''u_j''}\frac{\partial \widetilde{u}_i}{\partial x_j}}_{-P_k},\end{aligned} \tag{3.13}$$

where P_k is the production of turbulent kinetic energy, P_f is the production of scalar fluctuations, and $C_1,\ C_2,\ C_3,\ C_4$ are model constants. It is well-established that in an inhomogeneous flow, the transport equation for the scalar dissipation rate should contain production terms, due to scalar and velocity gradients, and dissipation terms, due to scalar as well as mechanical destruction of fluctuations [31]. Using the gradient-diffusion hypothesis and the turbulent eddy viscosity concept, the unclosed terms in Eq. (3.13) are modelled as

$$\widetilde{u_j''Z''} = -D_t\frac{\partial \widetilde{Z}}{\partial x_j}, \tag{3.14}$$

$$\widetilde{u_i''u_j''}\frac{\partial \widetilde{u}_i}{\partial x_j} = -\nu_t|\widetilde{S}|^2. \tag{3.15}$$

Finally, the transport equation for scalar dissipation rate is written as

$$\frac{\partial \overline{\rho}\widetilde{\chi}}{\partial t}+\frac{\partial \overline{\rho}\widetilde{u}_j\widetilde{\chi}}{\partial x_j} = \frac{\partial}{\partial x_j}\left[\left(\frac{\mu}{Sc}+\frac{\mu_t}{Sc_t}\right)\frac{\partial \widetilde{\chi}}{\partial x_j}\right] - C_1\underbrace{\overline{\rho}\frac{\widetilde{\chi}^2}{\widetilde{Z''^2}}}_{(I)} - C_2\underbrace{\overline{\rho}^2\frac{C_\mu \widetilde{k}}{\mu_t}\widetilde{\chi}}_{(II)} + C_3\underbrace{\frac{\overline{\rho}C_\mu\widetilde{k}}{Sc_t}\left(\frac{\partial \widetilde{Z}}{\partial x_j}\right)^2}_{(III)} + C_4\underbrace{\mu_t\frac{\widetilde{\chi}}{\widetilde{k}}|\widetilde{S}|^2}_{(IV)}. \tag{3.16}$$

This equation contains production terms, due to scalar and velocity gradients [(III), (IV)], and dissipation terms, due to scalar and mechanical destruction of fluctuations [(I), (II)].

3.2 Scalar variance and scalar dissipation rate modelling in LES

3.2.1 Scalar variance modelling

Following Jiménez *et al.* [28], the SGS scalar variance[1] in LES is defined as

$$\widetilde{Z''^2} = \widetilde{Z^2} - \widetilde{Z}^2, \tag{3.17}$$

where $Z' = Z - \widetilde{Z}$ is the fluctuation part of the scalar at subgrid-scale in this study for LES. It should be noted that the scalar mean and variance for URANS and LES have same forms. See Appendix A for details.

While a transport equation is solved for the scalar variance in URANS, the scalar variance in LES has commonly been obtained by algebraic models, such as the scale

[1]It is not a trivial to remind that the SGS scalar variance is denoted 'scalar variance' in short.

similarity model and the gradient-based model, mainly in order to reduce computational time. Since one of objectives in the present work is to propose a new approach to calculate the scalar variance in LES, it is worth reviewing the existing models.

The scale similarity model [13, 14] assumes that the behavior of SGS energy is self-similar over the turbulent scales and it reads

$$\widetilde{Z''^2} = C_{ss}\left(\widehat{\widetilde{Z}\widetilde{Z}} - \widehat{\widetilde{Z}}\widehat{\widetilde{Z}}\right), \tag{3.18}$$

where $\widehat{\cdot}$ is a test filter. In this study the test filter is taken as $\widehat{\Delta} = 2\overline{\Delta}$. C_{ss} is a model constant that must be given prior to the calculation.

However, two potential problems arise with this model. One is that the scale similarity model is formulated for a well-developed scalar spectrum following turbulent inertial behavior which might be not applicable to all turbulent flows. The other, and perhaps the more important, is that the model constant has to be specified prior to the calculation. It has been argued that the constant is a flow dependent variable [30]. Moreover, there is no reason to expect that a universal value for the model constant exists.

The gradient-based model [64] reads

$$\widetilde{Z''^2} = C_g\overline{\Delta}^2|\nabla\widetilde{Z}|^2, \tag{3.19}$$

where the model constant C_g needs to be determined. In this model the scalar variance is calculated based on the gradient of the scalar mean, which is the production mechanism of the scalar variance. The local filter width, $\overline{\Delta}$, serves as the length scale of the SGS turbulence and is adjusted to estimate the length scale of the SGS fluxes through C_g using a dynamic procedure [23].

Although existing scalar variance models for LES have been incorporated with combustion models and have demonstrated successful results, it should be noted that these existing models calculate the scalar variance *independently*, viz., there is no direct interaction between the scalar variance and its dissipation rate. In contrast, the

present work proposes to add a transport equation for the scalar variance to the LES system of the equations, so that only a single model is needed to represent dissipation and effects of mixing in the evolution of the scalar variance.

Similar to Eq. (3.6) in URANS, the filtered scalar variance transport equation in LES can be written as

$$\frac{\partial \overline{\rho}\widetilde{Z''^2}}{\partial t} + \frac{\partial \overline{\rho}\widetilde{u}_j\widetilde{Z''^2}}{\partial x_j} = \frac{\partial}{\partial x_j}\left[\overline{\rho}(D + D_{sgs})\frac{\partial \widetilde{Z''^2}}{\partial x_j}\right] + 2\overline{\rho}D_{sgs}\left(\frac{\partial \widetilde{Z}}{\partial x_j}\right)^2 - \overline{\rho}\widetilde{\chi}_{sgs}, \tag{3.20}$$

where the unclosed SGS scalar dissipation rate[2],

$$\widetilde{\chi}_{sgs} \equiv 2D\widetilde{\frac{\partial Z'}{\partial x_j}\frac{\partial Z'}{\partial x_j}}, \tag{3.21}$$

needs to be modelled.

3.2.2 Scalar dissipation rate modelling

The scalar dissipation rate in LES has been modelled using the local equilibrium assumption in previous studies [14, 34, 63]. By equating the production term to the scalar dissipation rate in Eq. (3.20), one may obtain

$$\widetilde{\chi}_{sgs} = 2D_{sgs}\left(\frac{\partial \widetilde{Z}}{\partial x_j}\right)^2. \tag{3.22}$$

Under this local equilibrium assumption, Eq. (3.20) becomes a simple convection-diffusion equation which has no production or dissipation terms. As explained earlier, this is problematic because the SGS scalar variance does not decay and thus complete mixing of reacting species is not attainable [28].

[2]The SGS scalar dissipation rate is denoted 'scalar dissipation rate' in this study.

Alternatively, Jiménez *et al.* [28] proposed to solve the scalar variance transport equation (Eq. (3.20)) in conjunction with an algebraic model for the scalar dissipation rate based on the ratio of the mechanical and the scalar time scales, similar to that used in URANS (Eq. (3.12)). The scalar dissipation rate by Jiménez *et al.* reads

$$\widetilde{\chi}_{sgs} = \frac{1}{Sc}\frac{\widetilde{\varepsilon}_{sgs}}{\widetilde{k}_{sgs}}\widetilde{Z''^2} = \frac{\left[\nu + (C_S\overline{\Delta})^2|\widetilde{S}|\right]}{Sc\, C_I\overline{\Delta}^2}\widetilde{Z''^2}, \tag{3.23}$$

where the SGS kinetic energy ($\widetilde{k}_{sgs}$) and its dissipation rate ($\widetilde{\varepsilon}_{sgs}$), which are not readily available in standard LES (viz., $\widetilde{k}_{sgs}$ and $\widetilde{\varepsilon}_{sgs}$ are not required to determine SGS scales), are modelled as

$$\widetilde{\varepsilon}_{sgs} = 2\left[\nu + (C_S\overline{\Delta})^2|\widetilde{S}|\right]\widetilde{S}_{ij}\widetilde{S}_{ij}\ , \quad \widetilde{k}_{sgs} = 2C_I\overline{\Delta}^2\widetilde{S}_{ij}\widetilde{S}_{ij}, \tag{3.24}$$

where C_S is the Smagorinsky SGS model constant and C_I is a model constant suggested to 0.07 by Jiménez *et al.*.

It should be noted that the inclusion of the molecular viscosity ($\nu = \mu/\rho$) in Eq. (3.24) seems to be inadequate to model the fluctuating part. Furthermore, this model may not be suitable for application to complex flows because the turbulent scalar time scale is not necessarily linearly related to the mechanical time scale in such flows, as discussed in Section 3.1.2. Therefore, solving a model transport equation to obtain the scalar dissipation rate, $\widetilde{\chi}_{sgs}$, is important for obtaining credible mixing results using LES.

3.2.3 New scalar dissipation rate modelling

Similar to the URANS models described in Section 3.1.2, a new algebraic LES model and a new transport LES model for the scalar dissipation rate are proposed in this study. Both new models for the scalar dissipation rate require a formulation of the

mechanical time scale, which is obtained using the SGS kinetic energy ($\widetilde{k}_{sgs}$) and its dissipation rate ($\widetilde{\varepsilon}_{sgs}$). Since $\widetilde{k}_{sgs}$ and $\widetilde{\varepsilon}_{sgs}$ are not readily available in the standard LES approach, both variables must be defined first.

At high Reynolds numbers, $\widetilde{\varepsilon}_{sgs}$ can be scaled reasonably well by

$$\widetilde{\varepsilon}_{sgs} = C_{\varepsilon}\frac{\widetilde{k}_{sgs}^{3/2}}{\overline{\Delta}}, \tag{3.25}$$

where $\overline{\Delta}$ is the filter length and $C_{\varepsilon} = 0.7$ is taken from Pope [69]. By assuming a local equilibrium flow, one may obtain

$$\widetilde{\varepsilon}_{sgs} = -\tau_{ij}\widetilde{S}_{ij} = \nu_{sgs}|\widetilde{S}|^2, \tag{3.26}$$

where $\nu_{sgs} = (C_S\overline{\Delta})^2|\widetilde{S}|$.

Using Eqs. (3.25) and (3.26), $\widetilde{\varepsilon}_{sgs}/\widetilde{k}_{sgs}$ can be obtained as

$$\frac{\widetilde{\varepsilon}_{sgs}}{\widetilde{k}_{sgs}} = C_D|\widetilde{S}|, \tag{3.27}$$

where $C_D = (C_{\varepsilon}C_S)^{2/3} = 0.17$ with $C_S = 0.1$. $\widetilde{\varepsilon}_{sgs}/\widetilde{k}_{sgs}$ can be interpreted as the turbulence frequency.

As discussed in Eq. (3.12), the turbulence frequency (Eq. (3.27)) is commonly used to estimate the turbulent scalar frequency ($\widetilde{\chi}_{sgs}/\widetilde{Z''^2}$). Therefore, a new algebraic model based on this ratio is proposed:

$$R_{\tau} = \frac{\widetilde{k}_{sgs}/\widetilde{\varepsilon}_{sgs}}{\widetilde{Z''^2}/\widetilde{\chi}_{sgs}} \rightarrow \widetilde{\chi}_{sgs} = R_{\tau}C_D|\widetilde{S}|\widetilde{Z''^2}. \tag{3.28}$$

Alternatively, another new model for the dissipation rate in LES is proposed based on the transport equation model of Jones and Musonge [31] (Eq. (3.13)). The new

model utilizes a time scale consistent with the Smagorinsky SGS model. A new scalar dissipation rate equation can be derived combined with the SGS time scale from Eq. (3.27). The semi-closed scalar dissipation rate equation can be written as

$$\begin{aligned}\frac{\partial\overline{\rho}\widetilde{\chi}_{sgs}}{\partial t}+\frac{\partial\overline{\rho}\widetilde{u}_j\widetilde{\chi}_{sgs}}{\partial x_j} &= \frac{\partial}{\partial x_j}\left[\left(\frac{\mu}{Sc}+\frac{\mu_{sgs}}{Sc_{sgs}}\right)\frac{\partial\widetilde{\chi}_{sgs}}{\partial x_j}\right]-C_1\overline{\rho}\frac{\widetilde{\chi}^2_{sgs}}{\widetilde{Z''^2}}-C_2\overline{\rho}\frac{\widetilde{\varepsilon}_{sgs}}{\widetilde{k}_{sgs}}\widetilde{\chi}_{sgs}\\ &\quad -C_3\overline{\rho}\frac{\widetilde{\varepsilon}_{sgs}}{\widetilde{k}_{sgs}}\widetilde{u'_jZ'}\frac{\partial\widetilde{Z}}{\partial x_j}-C_4\overline{\rho}\frac{\widetilde{\chi}_{sgs}}{\widetilde{k}_{sgs}}\widetilde{u'_iu'_j}\frac{\partial\widetilde{u}_i}{\partial x_j}. \qquad (3.29)\end{aligned}$$

The unclosed terms can be modelled using the eddy diffusivity concept and the Smagorinsky SGS model as

$$\begin{aligned}\widetilde{u'_jZ'} &= -D_{sgs}\frac{\partial\widetilde{Z}}{\partial x_j},\\ \widetilde{u'_iu'_j}\frac{\partial\widetilde{u}_i}{\partial x_j} &= -\nu_{sgs}|\widetilde{S}|^2. \qquad (3.30)\end{aligned}$$

Finally, the new scalar dissipation rate equation can be written as

$$\begin{aligned}\frac{\partial\overline{\rho}\widetilde{\chi}_{sgs}}{\partial t}+\frac{\partial\overline{\rho}\widetilde{u}_j\widetilde{\chi}_{sgs}}{\partial x_j} &= \frac{\partial}{\partial x_j}\left[\left(\frac{\mu}{Sc}+\frac{\mu_{sgs}}{Sc_{sgs}}\right)\frac{\partial\widetilde{\chi}_{sgs}}{\partial x_j}\right]-C_1\overline{\rho}\frac{\widetilde{\chi}^2_{sgs}}{\widetilde{Z''^2}}-C_2C_D\overline{\rho}|\widetilde{S}|\widetilde{\chi}_{sgs}\\ &\quad +C_3C_D\frac{\mu_{sgs}}{Sc_{sgs}}|\widetilde{S}|\left(\frac{\partial\widetilde{Z}}{\partial x_j}\right)^2+C_4C_D\overline{\rho}|\widetilde{S}|\widetilde{\chi}_{sgs}, \qquad (3.31)\end{aligned}$$

where C_1, C_2, C_3, C_4 are the model constants.

Chapter 4

Numerical Methods I: Discretization and Parallelization

The governing equations are discretized and implemented in the STREAM code [44] using the finite-volume method. The STREAM code is based on general non-orthogonal coordinates and employs a collocated storage arrangement for all transport variables. The Semi-Implicit Method for Pressure-Linked Equations (SIMPLE) algorithm [60] is used to enforce mass conservation and to solve the pressure-velocity coupling. A well-known checker-board oscillation problem, which can occur in the collocated storage arrangement, is resolved by adopting Rhie and Chow interpolation [73] that interpolates the cell face velocities from the adjacent nodal velocities at the cell centers. All the spatially discretized equations are integrated in time using a second-order three-level time-stepping method. It should be noted that the general aspects of numerical methods used for URANS and LES are same but it is mentioned if necessary.

In order to deal with long computing times, especially those required for LES, the STREAM code is parallelized using MPI [51]. The domain-decomposition method is employed and the parallelized code is optimized to run on the distributed memory systems by minimizing communication overhead.

In the first section of this chapter, the discretization schemes in the finite volume method and the boundary conditions are presented, and the code parallelization and its performance are discussed later.

4.1 Finite Volume Discretization

The coordinate transformation, which maps the physical domain into the computational domain such that the uniform rectangular grid in the computational domain corresponds to a non-uniform curvilinear grid in the physical domain, is first sought.

The variables (x, y, z) are transformed from physical space into (ξ, η, ζ) in the computational domain by the relationships:

$$\xi = \xi(x, y, z), \tag{4.1}$$
$$\eta = \eta(x, y, z), \tag{4.2}$$
$$\zeta = \zeta(x, y, z). \tag{4.3}$$

Following the transformation above, a transport equation governing a flow property ϕ can be written in terms of (ξ, η, ζ) as

$$\frac{\partial \rho \phi J}{\partial t} + \frac{\partial}{\partial \xi_j}\left[\rho U_j \phi - \rho \Gamma_\phi J q_{jj} \frac{\partial \phi}{\partial \xi_j}\right] = \rho J S_\phi, \tag{4.4}$$

where $U_1 = U, U_2 = V, U_3 = W$ and $\xi_1 = \xi, \xi_2 = \eta, \xi_3 = \zeta$ for the index $j = 1, 2, 3$.

The contravariant velocities (U, V, W), which satisfy the mass continuity equation, are defined as

$$U = J(u\xi_x + v\xi_y + w\xi_z), \tag{4.5}$$
$$V = J(u\eta_x + v\eta_y + w\eta_z), \tag{4.6}$$
$$W = J(u\zeta_x + v\zeta_y + w\zeta_z), \tag{4.7}$$

where $\xi_x = \partial\xi/\partial x$ and so on.

The Jacobian matrix $[J]$ for the transformation is defined as

$$[J] = \frac{\partial(x, y, z)}{\partial(\xi, \eta, \zeta)} = \begin{bmatrix} x_\xi & x_\eta & x_\zeta \\ y_\xi & y_\eta & y_\zeta \\ z_\xi & z_\eta & z_\zeta \end{bmatrix}$$

and J is defined as the determinant of the transformation matrix. The coefficients q_{11}, q_{22}, q_{33} are

$$q_{11} = \xi_x\xi_x + \xi_y\xi_y + \xi_z\xi_z, \tag{4.8}$$

$$q_{22} = \eta_x\eta_x + \eta_y\eta_y + \eta_z\eta_z, \tag{4.9}$$

$$q_{33} = \zeta_x\zeta_x + \zeta_y\zeta_y + \zeta_z\eta_z, \tag{4.10}$$

and these require the inverse matrix of the Jacobian,

$$[J^{-1}] = \begin{bmatrix} \xi_x & \xi_y & \xi_z \\ \eta_x & \eta_y & \eta_z \\ \zeta_x & \zeta_y & \zeta_z \end{bmatrix} = \frac{1}{J} \begin{bmatrix} y_\eta z_\zeta - y_\zeta z_\eta & x_\zeta z_\eta - x_\eta z_\zeta & x_\eta y_\zeta - x_\zeta y_\eta \\ y_\zeta z_\xi - y_\xi z_\zeta & x_\xi z_\zeta - x_\zeta z_\xi & x_\zeta y_\xi - x_\xi y_\zeta \\ y_\zeta z_\eta - y_\eta z_\xi & x_\eta z_\xi - x_\xi z_\eta & x_\xi y_\eta - x_\eta y_\xi \end{bmatrix}.$$

On the assumption that $\Delta\xi = \Delta\eta = \Delta\zeta = 1$ in the computational domain, J is, in fact, the volume of a cell over which the flow-governing equations are integrated. In the finite volume method, the solution domain is divided into a finite number of small control volumes. In a collocated grid system which is used in this study, all the flow variables are calculated and stored at the center of each control volume.

All the transport equations are integrated over the volume shown in Figure 4.1 and the application of the Gauss divergence theorem results in a balance of convective and diffusive cell face fluxes and volume-integrated net sources:

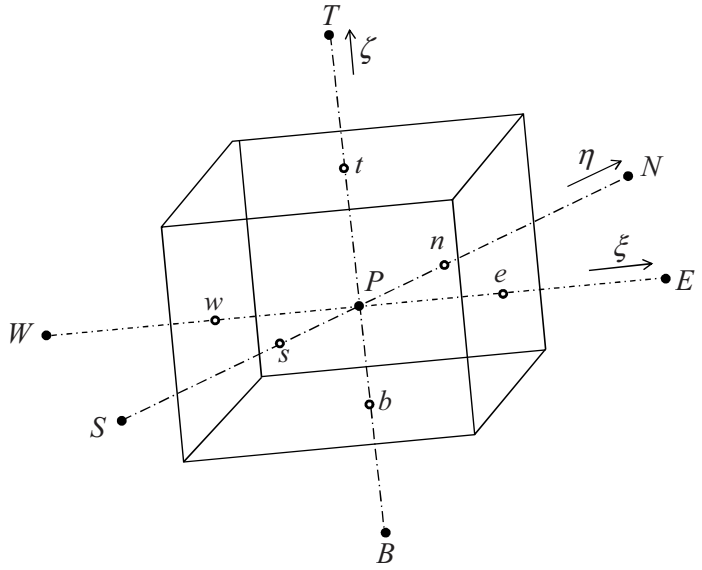

Figure 4.1: Finite volume and storage arrangement.

$$\begin{aligned}\int_{cv}\frac{\partial\rho\phi J}{\partial t} &+ \frac{1}{\Delta\xi}\left[\left(\rho U\phi-\rho\Gamma_\phi Jq_{11}\frac{\partial\phi}{\partial\xi}\right)_e-\left(\rho U\phi-\rho\Gamma_\phi Jq_{11}\frac{\partial\phi}{\partial\xi}\right)_w\right]\\ &+ \frac{1}{\Delta\eta}\left[\left(\rho V\phi-\rho\Gamma_\phi Jq_{22}\frac{\partial\phi}{\partial\eta}\right)_n-\left(\rho V\phi-\rho\Gamma_\phi Jq_{22}\frac{\partial\phi}{\partial\eta}\right)_s\right]\\ &+ \frac{1}{\Delta\zeta}\left[\left(\rho W\phi-\rho\Gamma_\phi Jq_{33}\frac{\partial\phi}{\partial\zeta}\right)_t-\left(\rho W\phi-\rho\Gamma_\phi Jq_{33}\frac{\partial\phi}{\partial\zeta}\right)_b\right]=\overline{S}_\phi+J\overline{S}_{CD},\end{aligned} \tag{4.11}$$

where $\overline{S_\phi}$ is the average value of the source term over the control volume and $\overline{S}_{CD}$ is the cross-diffusion term. Nodal variables are noted by the upper case subscripts P, E, W, N, S, T, B while values at control volume faces are denoted with the lower case subscripts, e, w, n, s, t, b. Note that in the current collocated grid arrangement variables are only stored at the nodes, thus all face values are obtained by interpolating nodal values [73] .

The time derivative term in Eq. (4.11) is integrated using a three-level time-stepping

scheme [21]

$$\int_{CV} \frac{\partial \rho \phi J}{\partial t} \approx \left(\frac{3\phi^{n+1} - 4\phi^n + \phi^{n-1}}{2\Delta t} \right) \rho^n J V_P, \tag{4.12}$$

where V_P is the volume of cell. The superscripts $n+1$, n, $n-1$ represent the current, one-step previous and two-step previous times, respectively.

Sources are discretized via a single-point quadrature and are linearized as follows:

$$\overline{S_\phi} = S_P \phi_P + S_C \tag{4.13}$$

with S_P being so chosen as to be unconditionally negative.

As shown in Eq. (4.11), the normal diffusion terms are treated implicitly. For example, the normal diffusive flux at the east face is approximated using the second-order Central Difference Scheme (CDS) [21]:

$$\left(\rho \Gamma_\phi J q_{11} \frac{\partial \phi}{\partial \xi} \right)_e = \left(\frac{\rho \Gamma_\phi J q_{11}}{\Delta \xi} \right)_e (\phi_E - \phi_P). \tag{4.14}$$

While normal diffusion is discretized implicitly, the cross-diffusion terms, which are evaluated by trilinear interpolation, are explicitly treated as source terms.

Application of the above approximations into the volume-integrated equation gives

$$A_P \phi_P = \sum_{m=E,W,N,S,T,B} A_m \phi_m + S_C + \left(\rho^n J \frac{4\phi^n - \phi^{n-1}}{2\Delta t} \right)_P, \tag{4.15}$$

where

$$\begin{aligned}
A_E &= (\Gamma_\phi J q_{11})_e - \langle |(\rho^n U)_e, 0| \rangle, \\
A_W &= (\Gamma_\phi J q_{11})_w - \langle |(\rho^n U)_w, 0| \rangle, \\
A_N &= (\Gamma_\phi J q_{22})_n - \langle |(\rho^n U)_n, 0| \rangle, \\
A_S &= (\Gamma_\phi J q_{22})_s - \langle |(\rho^n U)_s, 0| \rangle, \\
A_T &= (\Gamma_\phi J q_{33})_t - \langle |(\rho^n U)_t, 0| \rangle, \\
A_B &= (\Gamma_\phi J q_{33})_b - \langle |(\rho^n U)_b, 0| \rangle, \\
A_P &= A_E + A_W + A_N + A_S + A_T + A_B - S_P + \left(\frac{3\rho^n J}{2\Delta t} \right)_P.
\end{aligned} \tag{4.16}$$

The face value of ϕ is initially approximated in Eq. (4.16) using the first-order upwind scheme [21].

Pursuing higher accuracy in handling the convective fluxes, the second-order Upstream Monotonic Interpolation for Scalar Transport (UMIST) scheme, which is a total variation diminishing (TVD) scheme, is adopted for the URANS calculations. Full details are described in Lien [43]. For a flow moving in the positive $x-$direction where the convecting velocity $u_e > 0$,

$$\phi_e = \phi_P + \frac{1}{2}\psi(r)(\phi_E - \phi_P), \tag{4.17}$$

where

$$r = \frac{\phi_P - \phi_W}{\phi_E - \phi_P}, \tag{4.18}$$

and

$$\psi(r) = max[\ 0,\ min(2r,\ 0.25 + 0.75r,\ 0.75 + 0.25r,\ 2)\ ]. \tag{4.19}$$

It is known that CDS tends to produce spurious oscillations (or wiggles) when the local cell Peclet number, a measure of the relative strength of advection to diffusion, is large as reported in Versteeg *et al.* [84]. TVD schemes are formulated to provide oscillation-free solutions, but they are more numerically dissipative than CDS. A TVD scheme can be used in Monotonically Integrated LES (MILES) [76] as a combination of CDS with an additional numerical dissipation term to damp out the potential spurious oscillations.

In order to avoid excessive damping of the turbulent fluctuations in the flow simulation, CDS, which is less numerically dissipative than a TVD scheme, is widely used for LES. Therefore, CDS is adopted for LES calculations in the present study. The cell face value of any variable using CDS is obtained by

$$\phi_e = \frac{1}{2}\left(\phi_P + \phi_E\right). \tag{4.20}$$

In this study, the pressure, which is shown in the momentum equation (Eq. (2.2)), is calculated by solving the pressure-correction equation following the SIMPLE algorithm [60] and thus the pressure is governed indirectly through the continuity equation. The pressure-correction equation is derived by combining the discretized forms

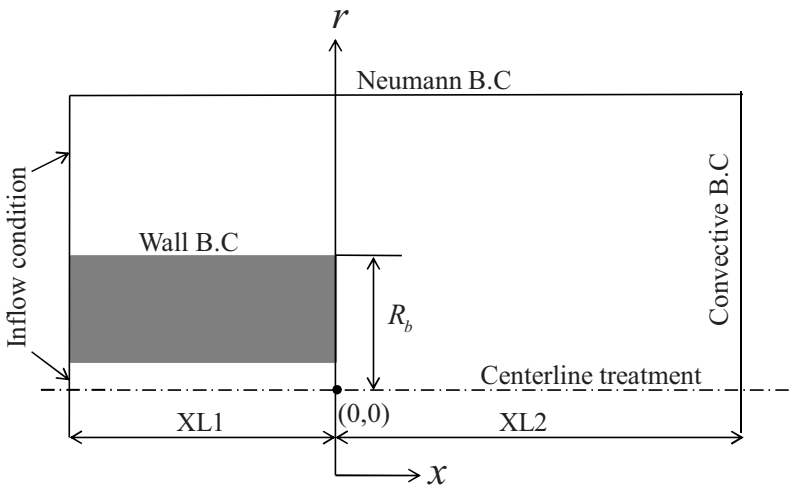

Figure 4.2: Boundary condition in the near-wall region.

of the momentum and continuity equations to give an equation linking the pressure correction at a node to its neighbours. Because of the collocated grid arrangement used in this study, a simple interpolation of nodal velocities to the control volume faces can lead to a decoupling between the velocity and pressure fields [60], in which the velocity field cannot sense a pressure difference on the order of the mesh spacing. This so-called *checker-board* situation leads to grid-scale oscillations. Following Rhie and Chow [73] this study uses a nonlinear interpolation scheme, in which an additional pressure smoothing term is included in the calculation of the face velocities. See [43] for details.

4.2 Boundary conditions

4.2.1 Inflow and outflow

The inflow condition for URANS is specified by the Dirichlet condition, in which a mean velocity profile normal to the inlet is prescribed and the lateral velocity is assumed to be zero. Furthermore, the turbulent variables are prescribed following

experimental data. The inflow condition is more problematic in LES calculations. LES of a spatially inhomogeneous flow, such as the bluff-body flow in this study, requires turbulent boundary conditions which must reflect the three-dimensional and unsteady nature of turbulence. This feature makes the results strongly depend on the velocity data prescribed at the inflow and constitutes a vicious circle: turbulence has to be prescribed at the inflow in order to simulate turbulence. The most desirable method for the inflow condition would be conducting a separate LES simulation to generate inflow condition data with sufficient turbulent kinetic energy; however, this simulation is also a full-scale and therefore requires additional time. Instead, the present study uses a so-called *white noise* inflow condition in which random fluctuations are added to a uniform velocity profile at the inflow plane. Furthermore, the inlet plane location is moved back to give the flow room to develop.

At the outflow plane, a Neumann boundary condition is given in URANS:

$$\frac{\partial \phi}{\partial n} = 0, \tag{4.21}$$

where n is the coordinate in the direction of the outward normal at boundary. For LES, a convective boundary condition is specified:

$$\frac{\partial \phi}{\partial t} + c\frac{\partial \phi}{\partial n} = 0, \tag{4.22}$$

where c is the convecting velocity.

The ambient pressure is set on the shell of the domain, and the pressure at the inflow and outflow planes are specified by using the Neumann condition. The Reynolds-averaged (Eq. (2.54)) or filtered scalar equation (Eq. (2.56)) is solved with the Dirichlet condition at the inflow plane and the Neumann condition specified at the outflow boundaries. The simulation details of URANS and LES are summarized in Table 4.1.

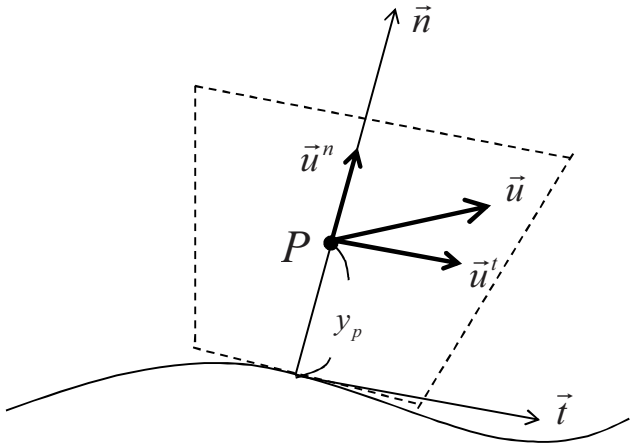

Figure 4.3: Boundary condition in the near-wall region.

4.2.2 Wall

The wall is the most common boundary type of solid encountered in confined flow problems. A no-slip Dirichlet condition is generally applied to all the velocity components at solid walls. For turbulent boundary layers, modelling the viscous sublayer adjacent to the wall is very difficult due to the small thickness of this layer. In order to resolve all of the viscous sublayer, buffer layer and log-law region we require very fine grid points in the near-wall region. At high Reynolds numbers, it is computationally expensive to resolve these viscous small-scale motions near the wall due to the fine-grid resolution near the wall. In order to reduce the computational cost in the near-wall regions, a wall function, based on the logarithmic law-of-the-wall, is

	URANS	LES
Turbulence model	$k-\varepsilon$ model	Smagorinsky SGS model
Convection scheme	UMIST [44]	CDS
Inflow condition	Uniform velocity	Uniform velocity+10% random
Outflow condition	Neumann	Convecting BC

Table 4.1: Simulation details in URANS and LES.

often used to mimic the effects of near-wall turbulence. The wall function allows the viscous sublayer adjacent to the wall to be bridged through a mathematical model.

The log-law is given by

$$u^+ = \begin{cases} \frac{1}{\kappa} ln(y^+) + B & \text{if } y^+ > 11.63 \\ \\ y^+ & \text{if } y^+ \leq 11.63 \end{cases}, \tag{4.23}$$

where

$$\begin{aligned} u^+ &= \overline{u}/u_\tau, \\ u_\tau &= \sqrt{\tau_w/\rho}, \\ y^+ &= \rho u_\tau y/\mu. \end{aligned} \tag{4.24}$$

u_τ is the friction velocity and y^+ is a viscous unit coordinate. The von Karman constant κ is set to 0.41 and $B = 5.5$ for a smooth wall. Using Eq. (4.23) in $k - \varepsilon$ model, the log-law is modified as

$$k = \frac{u_\tau^2}{\sqrt{C_\mu}}, \quad \varepsilon = \frac{u_\tau^3}{\kappa y}. \tag{4.25}$$

Although the wall function is applied at the first grid node adjacent to the wall and this node should lie in the logarithmic layer ($y^+ > 30$) where the log-law is valid, it is a common practice that the first node can be placed at $y^+ > 11.6$ following Versteeg *et al.* [84], where $y^+ = 11.6$ represents the intersection of the linear sublayer law (i.e., $u^+ = y^+$) and the log-law.

For the first grid point adjacent to the wall, the wall shear stress τ_w is calculated in URANS using:

$$\tau_w = \begin{cases} \frac{\rho C_\mu^{1/4} k^{1/2}}{u^+} u_p^t & \text{if } y^+ > 11.63 \\ \\ \mu \frac{u_p^t}{y_p} & \text{if } y^+ \leq 11.63 \end{cases}, \tag{4.26}$$

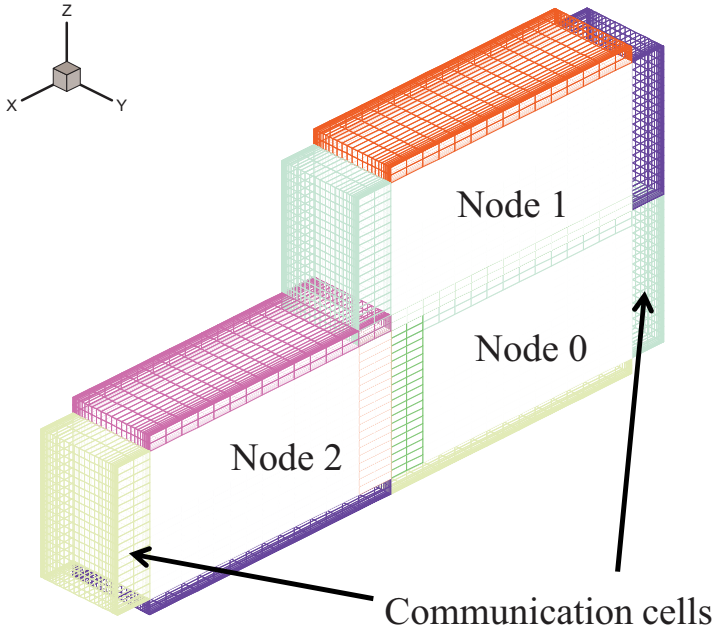

Figure 4.4: Domain decomposition and communication cells.

where u_p^t is the tangential velocity at node P.

For the bluff-body LES calculations, the wall boundary condition needs to be redefined simply because the turbulent kinetic energy in LES is not available in this study. The wall boundary condition in LES reads

$$\tau_w = \begin{cases} \rho u_\tau^2 \frac{u_p^t}{|u_p|} & \text{if } y^+ > 11.63 \\ \mu \frac{u_p^t}{y_p} & \text{if } y^+ \leq 11.63 \end{cases} \tag{4.27}$$

4.3 Code Parallelization

There are two methods commonly used to parallelize a code; either the code is written as a number of separate programs that communicate with each other via message

passing, or the program is written as a conventional program with a single thread of control, and a compiler converts the code into an program that operates on its data in parallel [58]. In this study, the STREAM code is parallelized by the message passing technique using the MPI library [51]. A single computational domain is divided into several sub-domains, which are processed while the exchange of information between sub-domains is achieved through message passing. In the present study, the SPMD (Single Program Multiple Data) model is used for the parallelization. This means that the parallelized code is same for all involved processors, but each processor has different boundary conditions and thus gives different results. In developing the parallel STREAM code, the following key ideas are considered:

1. The parallelized code should give the same result with the serial code no matter how the computational domain is divided.
2. Each code on each processor is the same but has different boundary conditions.
3. Message passing is hardware independent and achieved by using a standard message passing library such as MPI.
4. Sub-domains are best divided to place equal load on each processor.
5. Communication overhead including idle time, which occurs when the processor waits for receiving data from another, needs to be minimized.

As shown in Figure 4.4, the computational domain for turbulent channel flow, which will be discussed in Sec. 5.1, is divided into several sub-domains and each sub-domain has communication cell (ghost cell) for sending and/or receiving boundary data from the neighbouring sub-domain.

Figure 4.5 presents a closer look at the boundary communication between sub-domains. Boundary values in a sub-domain are updated at every time step through the boundary communication. To this end, as shown in the figure, the values at each sub-domain boundary are passed into the ghost cell in the neighbouring sub-domain and

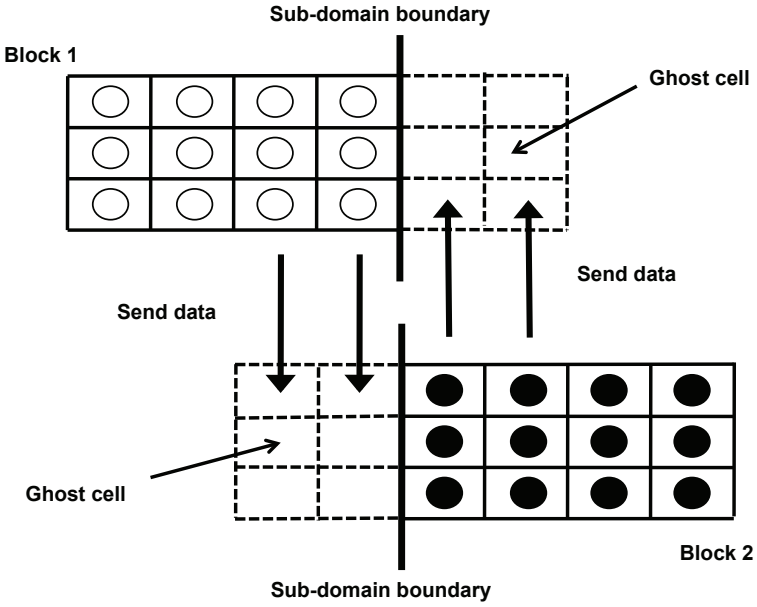

Figure 4.5: Data exchange between sub-domains.

vice versa. The exchange of the boundary values is thus conducted at every computational boundary which has a neighbouring sub-domain.

The parallelized STREAM code is tested by measuring the speed-up and the parallel efficiency, which are quite common practices in parallelization performance testing. The speed-up ratio is defined by

$$S_P = \frac{T_1}{T_P}, \tag{4.28}$$

where T_1 is the elapsed time of the simulation with one processor and T_P is the elapsed time with multiple processors. Figure 4.6(a) shows the speed-up ratio up to 16 processors on AMD Opteron machines with a Myrinet interconnection; the parallelized STREAM code runs about 14 times faster while using 16 processors. This speed-up ratio, which gives an idea about the code scalability, increases linearly with the number of processors for the problem of interest. Therefore, it can be said that the parallelized STREAM code shows great scalability up to 16 processors.

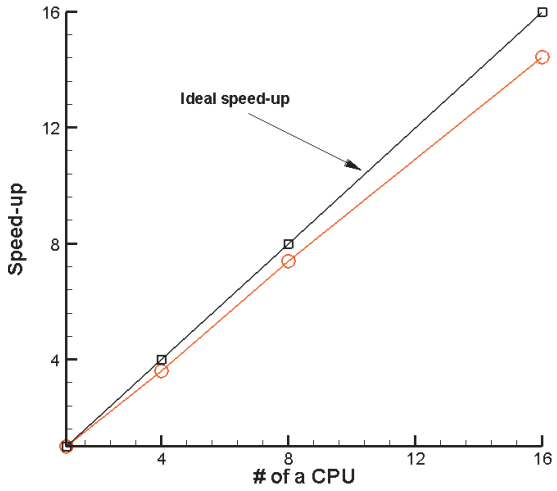

(a) Parallel speed-up

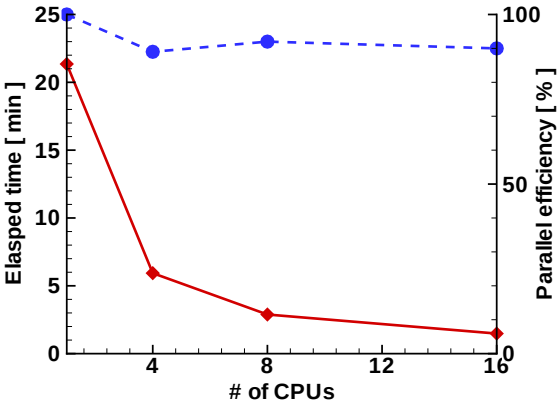

(b) Parallel efficiency

Figure 4.6: Parallel efficiency (dash line) and speed-up ratio (solid line) using 16 processors.

The parallel efficiency E_P, which shows how well the processors are utilized while running in parallel, is defined as

$$E_P(\%) = \frac{S_P}{nP} \times 100, \tag{4.29}$$

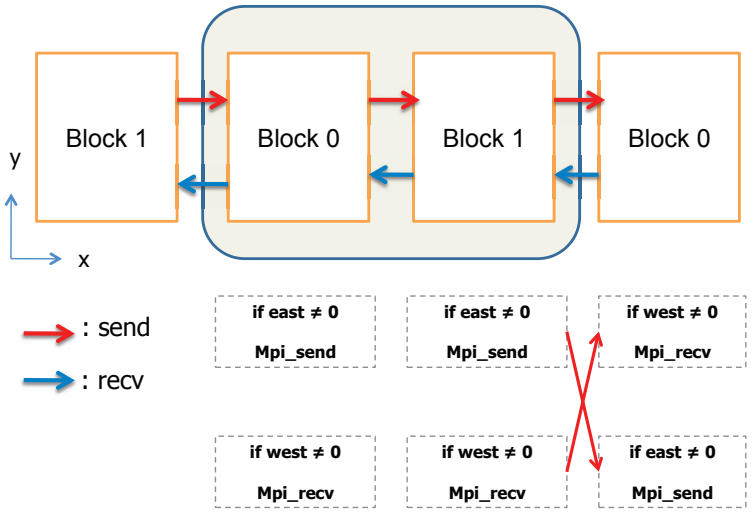

Figure 4.7: MPI deadlock case and resolution.

where nP is the number of processors. In general the parallel efficiency is less than 1, and so doubling the number of processors decreases the runtime by less than half. The parallelized STREAM code is run on up to 16 processors. As seen in Figure 4.6(b), the STREAM code gives about 90% parallel efficiency and so the processors involved are well-utilized. This also shows that the computational domain is appropriately divided and distributed to each processor while minimizing communication overhead. The overhead would be large if the allocated sub-domain on each processor took a relatively short time to finish the calculation compared to the communication time.

Using blocking communication in MPI ensures the completion of communications. Details of implementation are not presented here. Instead, one issue and resolution of blocking communication that was encountered in the process of parallelization is explained as follows. The periodic boundary condition is adopted in simulating a turbulent channel flow in Section 5 in order to reduce the computational cost because it simulates a small part of large domain assuming the small part is replicated. When blocking communications such as *MPI_Send()* and *MPI_Recv()* in MPI library are

applied to this boundary condition, a well-known MPI-deadlock problem occurs.

The function *MPI_Send()* does not complete until the memory buffer is empty (i.e., the receiver has received all data). For example, the computational domain is divided into two sub-domains such as block 0 and block 1 . In the periodic boundary condition, block 0 has block 1 as the left-side neighbour and block 1 has block 0 as the right-side neighbour. For right-side boundary value communication, block 0 does *MPI_Send()* to block 1. However, this communication would not complete because block 1 is also sending its right-side boundary value to block 0 due to the periodic boundary condition. Note that the STREAM code is parallelized using SPMD model so that it has same code for each processor. This situation is called MPI-deadlock and the code is not running anymore but just waiting.

Even though there are many different solutions to this problem, in author's opinion, it seems easiest to require that the order of communications be slightly modified to avoid this simultaneous sending or receiving situation; in the modification, block 1 does *MPI_Recv()* first and *MPI_Send()* later as illustrated in Figure 4.7. This helps MPI-deadlock to disappear so that the periodic boundary condition works without difficulty.

Chapter 5

Numerical methods II: Code validation

Validation of the implementation of LES and its parallelization is a very important step in establishing trust in the results of the present study. The implementation of the Smagorinsky SGS model is validated and the capability of the model is analyzed through the investigation of a turbulent channel flow, which has become a benchmark test case in the field of LES. Since the present study aims to simulate bluff-body flow, channel flow is an appropriate validation case because both of flows involve walls. However, the detail turbulent structure of bluff-body wall is not an interest.

In this chapter a brief introduction to the physics of turbulent channel flow is first presented and a short review of related work is provided. Aspects related to the set-up of the simulations are described and the results are discussed by comparison to DNS data [37].

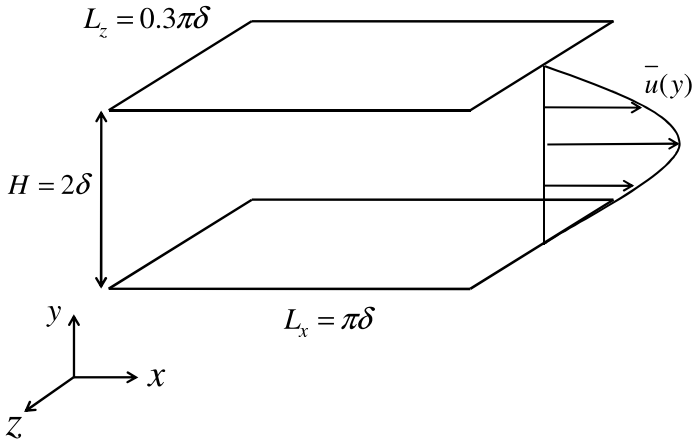

Figure 5.1: Geometry for fully developed plane channel flow.

5.1 Turbulent channel flow

Fully developed channel flow is a well-known test case and is chosen for several reasons. Firstly, it is probably the simplest and the most idealized wall-bounded flow imaginable which illustrates important effects of mean shear and wall influence. The flow is statistically homogeneous in the streamwise and spanwise directions. Which decreases the computational cost and allows for some important analytical relations that aid in the interpretation of the results. Secondly, the channel flow is a very sensitive test case for LES and accurate prediction of turbulent channel flow remains a great challenge in spite of its geometrical simplicity.

The turbulence in the channel flow is characterized by the wall-friction Reynolds number $Re_\tau = \delta u_\tau/\nu$, where δ is half the channel width and $u_\tau = (\nu|\frac{du}{dy}|_w)^{1/2}$ is the wall friction velocity. Several authors have investigated turbulent channel flow; to the author's knowledge, the most well-known is probably the DNS study by Kim *et al.* [37]. The computational domain employed by Kim *et al.* was $4\pi\delta \times 2\delta \times 2\pi\delta$ in the streamwise, wall-normal and spanwise directions, and was concluded to be sufficient to yield results unaffected by the periodic boundaries. A standard pseudo-spectral code was utilized with a resolution of $192 \times 129 \times 160$ mesh points, which, for the

Reynolds number $Re_\tau = 180$, was concluded to yield a well-resolved flow and accurate results. Recently, a DNS simulation with $Re_\tau = 590$ has been presented by Moser *et al.* [55] obtained with the same numerical method.

Through the years, several investigations of channel flow using LES have been presented. The first computation of turbulent channel flow was actually a LES at $Re_\tau = 180$ performed by Deardoff [18]. Here, a log-layer assumption was applied for the wall boundary condition and a total of 6720 uniform grid points were utilized. Later, in the LES of Moin and Kim [54], the boundary layer was fully resolved to yield information about the turbulent structures in the near-wall area. The near-wall region of the channel contains flow structures called streaks that are responsible for a major portion of the turbulence energy production [74], and these structures must be resolved in order to obtain accurate results. The Reynolds number has in recent LES simulations of Sarghini and Piomelli [79] been increased to $Re_\tau = 1050$.

Plane channel flow has become a benchmark test case in LES for presenting new models by Germano *et al.* [23] or for evaluating the performance of existing models. In the study of Härtel and Kleiser [26] a pseudo-spectral method was used for investigating the behaviour of the Smagorinsky SGS model at different Reynolds numbers $Re_\tau = 115, 210$ and 300. For $Re_\tau = 180$, $32 \times 32 \times 64$ mesh of points was employed. It was concluded that errors compared to a DNS in the same study were mainly caused by the deficiencies of the model in the buffer layer and that these errors were reduced with increasing Reynolds number. The influence of applying a second-order numerical method was analyzed by Sagaut *et al.* [77]. Several SGS models were tested in a finite difference code at $Re_\tau = 180$ and 400. The level of errors was found not to differ from those reported using higher-order numerical methods and the main flaws were attributed to the basic SGS model and not to the dynamic procedure applied.

Present simulations are performed for $Re_\tau = 180$ using the *minimal channel* flow. It has a domain $\pi\delta \times 2\delta \times 0.3\pi\delta$ in the streamwise, wall-normal and spanwise directions. It is much smaller than the one used by Kim *et al.* [37]. The term *minimal channel* refers to the smallest flow unit that has been found able to sustain turbulence for a given Reynolds number [30]. While it is not large enough to provide a realistic

description of the dynamics of the region in the middle of the channel flow, Jiménez *et al.* [30] has shown that it provides a valid representation of the near-wall region. Hence it is often used in studies of near-wall turbulence. In the present study, the focus is not on the physics of the flow itself but on the capability of the SGS model and the parallel performance of the developed code. By simulating the minimal channel flow, computational time can be saved due to the smaller domain and the SGS models in LES can be tested for its main functionality; dissipating turbulence fluctuations. Therefore, the minimal channel flow is adequate for the purpose of code validation in the present study.

5.2 Shear stress balance

The fully developed plane channel flow has three homogeneous directions including time; i.e., directions along which statistics do not change, and there are no issues regarding inflow conditions, which can be problematic in LES. There are also some analytical results for this flow, which are useful for interpretation. One of the most useful is the shear stress balance that will be derived below.

The only assumption necessary is that of statistical homogeneity in x, z and t. This implies that

$$\frac{\partial \overline{\cdot}}{\partial x} = \frac{\partial \overline{\cdot}}{\partial z} = \frac{\partial \overline{\cdot}}{\partial t} = 0 \tag{5.1}$$

for all quantities except the streamwise mean pressure gradient.

The mean pressure gradient is necessary to drive the flow as shown in Figure 5.2. The pressure can be decomposed into two parts:

$$p(x, y, z, t) = P(x) + p^{periodic}(x, y, z, t), \tag{5.2}$$

and the gradient can be obtained as

$$\frac{\partial \overline{p}}{\partial x} = \frac{dP}{dx}, \tag{5.3}$$

$$\frac{\partial \overline{p}^{periodic}}{\partial x} = 0. \tag{5.4}$$

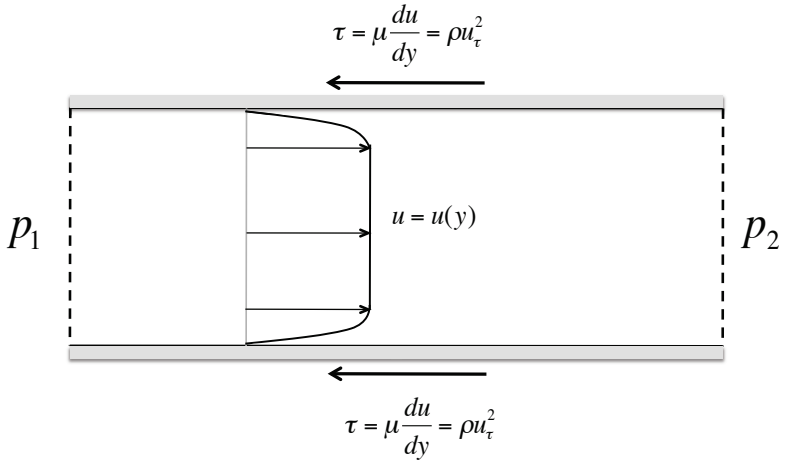

Figure 5.2: Balancing forces for plane channel flow.

By using Eq. (5.1), the continuity equation Eq. (2.1) for the mean flow becomes

$$\frac{\partial \overline{u}}{\partial x} = \frac{\partial \overline{v}}{\partial y} = 0. \tag{5.5}$$

Integrating this from the lower wall to the other wall with no-slip boundary conditions yields $\overline{v} = 0$ everywhere.

Averaging the streamwise momentum equation Eq. (2.2) using the conditions developed so far yields

$$0 = -\frac{1}{\rho}\frac{\partial P}{\partial x} + \nu \frac{\partial^2 \overline{u}}{\partial y^2} - \frac{\partial \overline{u'v'}}{\partial y} - \frac{\partial \overline{\tau_{12}}}{\partial y}. \tag{5.6}$$

In a similar way, integrating from the lower wall to y, and making the boundary conditions $u = v = 0$ at walls, yields

$$0 = -\frac{1}{\rho}\frac{\partial P}{\partial x} y + \nu \frac{\partial \overline{u}}{\partial y}|_{wall} - \overline{u'v'} - \overline{\tau_{12}} + \overline{\tau_{12}}\,|_{wall}\,. \tag{5.7}$$

The average wall shear stress is

$$\nu \frac{\partial \overline{u}}{\partial y}\,|_{wall} \equiv u_\tau^2, \tag{5.8}$$

which defines the friction velocity u_τ.

The average residual stress tensor ($\overline{\tau_{12}}\,|_{wall}$) is zero at the wall due to the boundary conditions, and hence consistent models for τ_{ij} should satisfy this as well. One then gets

$$0 = -\frac{1}{\rho}\frac{\partial P}{\partial x}y + \nu\frac{\partial \overline{u}}{\partial y} - \overline{u'v'} - \overline{\tau_{12}} - u_\tau^2. \tag{5.9}$$

With δ denoting the channel half width, setting $y = 2\delta$ and making use of the boundary conditions yields

$$-\frac{1}{\rho}\frac{dP}{dx} = \frac{u_\tau^2}{\delta}, \tag{5.10}$$

which is simply a balance between the pressure gradient and the wall friction. Substituting this into Eq. (5.9) yields,

$$\nu\frac{\partial \overline{u}}{\partial y} - \overline{u'v'} - \overline{\tau_{12}} = u_\tau^2\left(1 - \frac{y}{\delta}\right), \tag{5.11}$$

which shows the necessary balance between the different shear stresses in fully developed channel flow. Note that this is an exact solution assuming statistically homogeneous flow, and it is valid for all turbulence models for τ_{ij} that satisfy the proper boundary condition for the stress tensor. With the eddy viscosity hypothesis, the shear stress balance becomes

$$\nu\frac{\partial \overline{u}}{\partial y} - \overline{u'v'} + \overline{\nu_t\left(\frac{\partial u}{\partial y} + \frac{\partial v}{\partial x}\right)} = u_\tau^2\left(1 - \frac{y}{\delta}\right). \tag{5.12}$$

If the fluctuations of ν_t and the strain rate are assumed to be uncorrelated, the equation above becomes

$$(\nu + \nu_t)\frac{\partial \overline{u}}{\partial y} - \overline{u'v'} \approx u_\tau^2\left(1 - \frac{y}{\delta}\right). \tag{5.13}$$

Assuming $u_\tau = 1$ the total shear stress should have a linear distribution along the transverse coordinate.

5.3 Simulation details

The flow geometry and the coordinate are shown in Figure 5.1. The channel size in the present simulations is taken as a minimal flow unit [30], which is a very effective domain size to obtain low moment statistics. Here $L_x = \pi\delta$ and $L_z = 0.3\pi\delta$ are chosen to meet the minimal flow unit. Given this channel domain, two different grid resolutions (Grid A and Grid B) are simulated; Grid B has a finer wall-normal resolution than Grid A as shown in Table 5.1. The grid arrangement is uniformly spaced in the streamwise (x) and spanwise (z) directions respectively. In this study $\Delta x^+ \approx 23$ and $\Delta z^+ \approx 10$ are used in wall unit.

A stretched non-uniform mesh is used in the wall-normal direction as shown in Figure 5.3. The grid coordinates in this direction are given by

$$y^l = 1 + \frac{\tanh \Gamma(2l/N_y - 1)}{\tanh(\Gamma)}, \quad l = 0, \ldots, N_y, \tag{5.14}$$

where y^l is the y-coordinate of the lth grid line, and Γ is a stretching factor. A stretching factor is chosen to fulfill the criteria by Zang [88] for achieving a reliable LES; $\Delta x^+ < 80$ and having $\Delta z^+ < 30$ and at least 3 points in the sublayer $0 < y^+ < 10$. Although the non-uniformity of the computational mesh can reduce the accuracy of the differencing scheme, grid stretching is necessary to achieve an effective resolution of the boundary layer.

Fully developed turbulent channel flow is homogeneous in the streamwise and spanwise directions; the periodic boundary condition is employed in these directions. At the wall a no-slip boundary condition is imposed for all velocity components and the wall function, which is described in Section 4.2.2, is implemented without applying

Case	(N_x, N_y, N_z)	Δx^+	y_1^+	Δy^+_{min}	Δy^+_{max}	Δz^+
Grid A	$(24, 32, 16)$	23	1.01	0.95	30.12	10
Grid B	$(24, 64, 16)$	23	0.66	0.42	14.68	10

Table 5.1: Grid resolutions for the turbulent channel flow simulations.

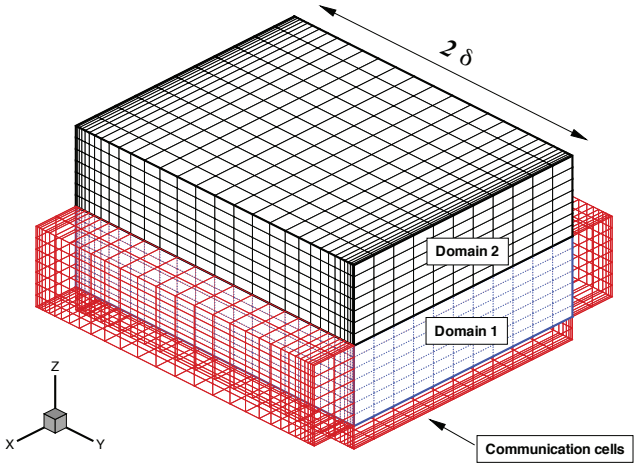

Figure 5.3: Computational domain decomposition with communication cells.

the log-law wall function. Instead, in order to achieve some kind of asymptotic behaviour in the near-wall area, the length scale is multiplied by a van Driest damping factor to account for the reduced growth of small scales and to force the SGS viscosity to vanish at the solid boundary. This explicit wall damping factor is seen to depend on the non-dimensional wall distance y^+. Its importance is reduced throughout the boundary layer and effectively vanishes for $y^+ > 100$;

$$D_{wall} = 1 - exp\left(-\frac{y+}{A^+}\right), \tag{5.15}$$

where A^+ is a constant of 25. Note that this wall damping is not used for the Smagorinsky SGS model with the dynamic procedure.

The flow is statistically stationary, so the physics of the initial condition is relatively unimportant and the simulation results should be independent of the initial condition. However, in practice the initial condition is important because it takes a long time to obtain enough fluctuations starting from a laminar flow; furthermore, the flow is easily re-laminarized due to excessive dissipation. Therefore, a so-called coarse-grid DNS calculation, which has no SGS model, is first performed to generate the initial

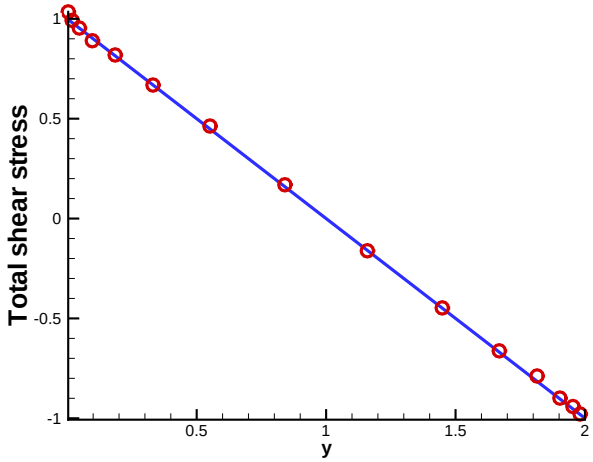

Figure 5.4: Total shear stress balance. o: Smagorinsky SGS model (symbol skipped by 4), solid line: analytical solution.

.

field and all LES simulations are restarted from this coarse-grid DNS data as the initial condition. Simulations are run for $t = 500U_b/\delta$ before beginning to collect statistics and a linear variation of the time-averaged total shear stress is examined. The total shear stress obtained from the Smagorinsky SGS model with Grid B is compared with the analytical solution (Eq. (5.13)) in Figure 5.4.

Statistics are collected over same period after running for $t = 500U_b/\delta$, where U_b is a bulk velocity. Statistics of the flow are then averaged over the horizontal plane ($x - z$ plane) parallel to the channel wall and in time. The time step $\Delta t^* = 0.005$ for Grid A and $\Delta t^* = 0.002$ for Grid B, where $t^* = t/(\delta u_\tau)$, is carefully chosen to satisfy $CFL \equiv u\Delta t/\Delta x \leq 1$ throughout the computational domain for each grid resolution. For most of the calculation time, the CFL number is below 0.5. In Figure 5.5, the energy spectrum of the channel flow in time is shown. The turbulent channel flow is fully developed after a certain amount of time integration and the energy spectrum of the streamwise velocity exhibits a slope close to the Kolmogorov $-5/3$. This implies that the LES simulation has adequately resolved most of the energy present in the

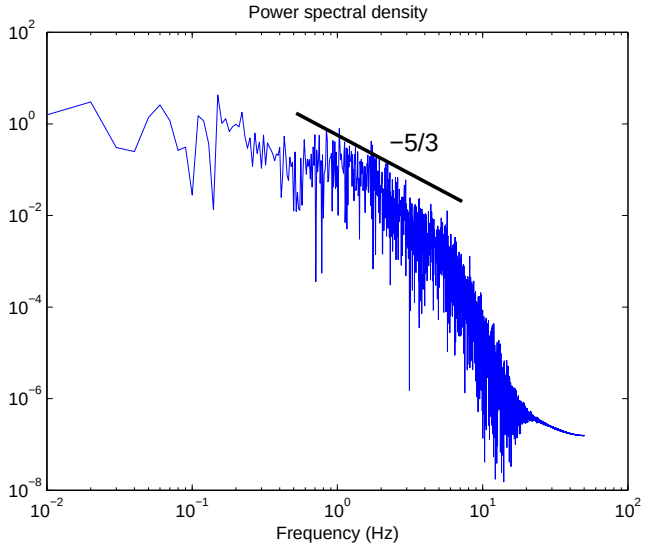

Figure 5.5: Time energy spectra of the channel flow.

turbulent scales of the flow for the streamwise velocity. Because most of the energy in the flow has been resolved, it is expected that the characteristics of the dominant flow features predicted by the LES simulation should be nearly independent of the details of the SGS closure.

Three different simulations varying the SGS model are performed first with Grid A; no SGS model (NM), a dynamic Smagorinsky SGS model (DM) and a Smagorinsky SGS model (SM). While the model constant C_S is fixed in the SM, the model constant C_S in the DM varies throughout the flow and is determined by the dynamic procedure [23]. The effects of the Smagorinsky SGS models are compared to results obtained without a SGS model, so-called coarse-grid DNS.

The SM employs the van Driest damping function of Eq. (5.15):

$$\mu_t = \overline{\rho}\left[C_S(1-(e^{-y^+/A+}))\overline{\Delta}\right]^2 |\widetilde{S}|. \tag{5.16}$$

5.4 Results

All simulation results are compared with DNS data from Kim and Moin [37]. As shown in Figure 5.6(a), the mean velocity profiles for all SGS models Grid A show quite similar to each other and are in good agreement with the DNS data. A closer look at these mean velocity profiles tells that the no SGS model (NM) gives the best agreement with DNS data particularly in the region after $y^+ = 20$. It is not surprising that a numerical code can produce good results without a SGS model [50] and the SGS model results are in fact not a large deviation from this state. The log-law line, which is seen as a dashed line in Figure 5.6(a), follow Eq (4.23). All mean velocity profiles follow the trend of the logarithmic law but all experience a bump in the vicinity of the core flow. This bump seems to be attributed to the channel configuration; the minimal channel. It is towards the center that the presence of the missing outer flow is felt [37].

In Figure 5.6(a) it is also found for all SGS models that the slope of the logarithmic law is well-predicted but that the logarithmic law is over-predicted after $y^+ = 20$. This means that the viscous sub-layer is too thick [81]. The skin friction coefficient,

$$c_f = \frac{\tau_w}{\frac{1}{2}\rho U_b^2}, \tag{5.17}$$

is also under-predicted and the results for each case are shown in Table 5.2. The streamwise velocity fluctuations shown in Figure 5.6(b) are too high, while the vertical and spanwise fluctuations are too low. The peak location and magnitude are better predicted by the NM than others. In the Smagorinsky SGS model, the eddy viscosity damps the flow and the wall stresses decrease; the eddy viscosity seems to be over-predicted and thus excessively dissipates turbulent energy. These results are typical at such low grid resolution [39]. If near-wall flow structures are not properly resolved, the effective shear stress on the wall is reduced. The fluctuations normal to the wall are under-predicted, which decreases the momentum transfer between the wall and the core flow. The dominant streamwise fluctuations grow and so does the resolved turbulent kinetic energy.

The dynamic Smagorinsky SGS model (DM) shows similar but better results than the Smagorinsky SGS model (SM). Since the DM does not adopt the wall function but uses a dynamic procedure by applying a test-filtering operation, it would be considered that the test-filtering implementation works well. The DM takes a much longer time to give a converged solution compared to the SM due to the test-filtering operation. Since the channel flow is simulated only for code validation, the DM is not re-simulated with Grid B. However, it is worth noting that the dynamic procedure is re-utilized to simulate the scale similarity model in predicting LES scalar variance in Section 6.3.2.

The NM and the SM are simulated again on the higher resolution Grid B whose mesh density is doubled in the wall-normal direction. The mean and rms of the velocities are presented in Figure 5.7. The mean velocity profiles shown in Figure 5.7(a) are improved over the results obtained using Grid A. The streamwise fluctuation and the shear stresses for both models are better predicted than with Grid A. However, the wall-normal and the spanwise fluctuations are still under-predicted and the peak location is still not predicted correctly. As seen in the Grid A calculation, it is also found that there is a bump near the center of the flow.

Having said that the NM shows better results than other Smagorsinky SGS models in the Grid A calculation, all models with Grid B show very similar results to each other and are in good agreement with DNS data. This seems reasonable and was also observed by Majander *et al.* [50] because the eddy viscosity is quite dependent

Case	Skin friction c_f	c_f error
DNS [37]	8.18×10^{-3}	–
NM [Grid A]	6.667×10^{-3}	18.4%
DM [Grid A]	6.024×10^{-3}	26%
SM [Grid A]	6.515×10^{-3}	20%
NM [Grid B]	7.34×10^{-3}	10%
SM [Grid B]	6.86×10^{-3}	16%

Table 5.2: Skin friction coefficients for the turbulent channel flow.

on the grid resolution. The finer grid simulation predicts all the monitored turbulent quantities well. However, the over-prediction of the streamwise fluctuation and under-prediction in the wall-normal and spanwise directions are still observed. The skin friction coefficients for both models are compared in Table 5.2. Similar to the Grid A simulation, the mean velocity profiles are over-predicted and the skin friction coefficient is still under-predicted.

5.5 Summary and conclusion

Turbulent channel flow for $Re_\tau = 180$ is simulated for the purpose of code validation. The STREAM code [44], which has been developed for LES calculation and parallelized using MPI in this study, is used for the validation. The domain decomposition method is successfully employed to decompose the computational domain into sub-domains and all necessary information is exchanged among the sub-domains using MPI communications. Simulations have been conducted with two different grid resolutions (Grid A and Grid B) and three different SGS models (no-SGS-model, dynamic Smagorinsky SGS, Smagorinsky SGS). The channel flow is initialized by turning off the SGS model (no-SGS-model) and then SGS model simulations are restarted from there in order to avoid re-laminarization. The Smagorinsky SGS model works well with either the dynamic procedure or the wall function near the wall. By increasing wall-normal resolution in Grid B, the mean velocity and the shear stress predictions are improved but still the streamwise fluctuation is over-predicted and the fluctuations in the wall-normal and the spanwise directions are under-predicted. These results are typical at such low grid resolutions. However, these are satisfactory for now since the purpose of this chapter is to check all the components necessary in LES and parallelization.

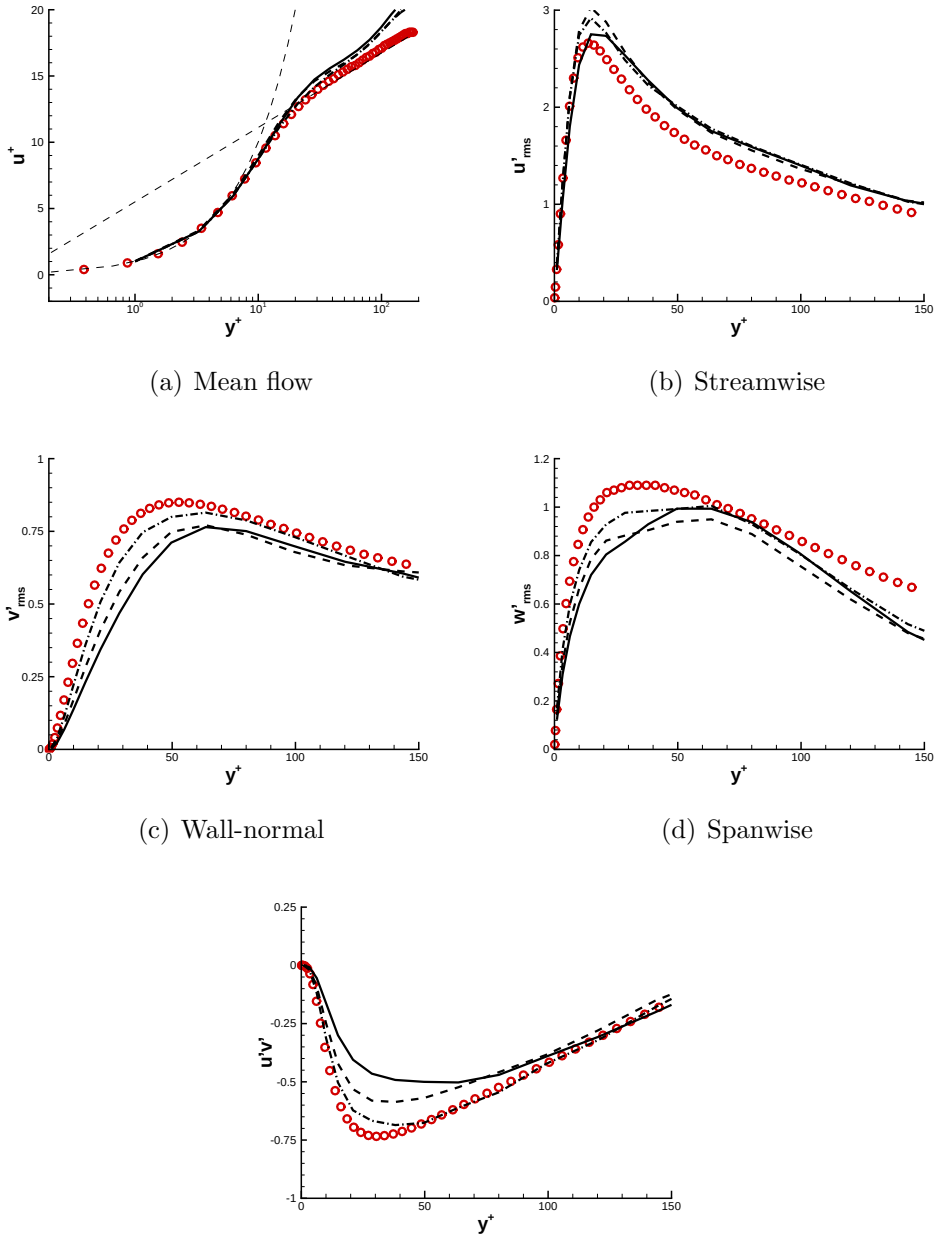

(a) Mean flow

(b) Streamwise

(c) Wall-normal

(d) Spanwise

(e) Shear stress

Figure 5.6: Turbulent statistics (Grid A). dash-dot: NM, dash: DM, solid line: SM, o: DNS data [37].

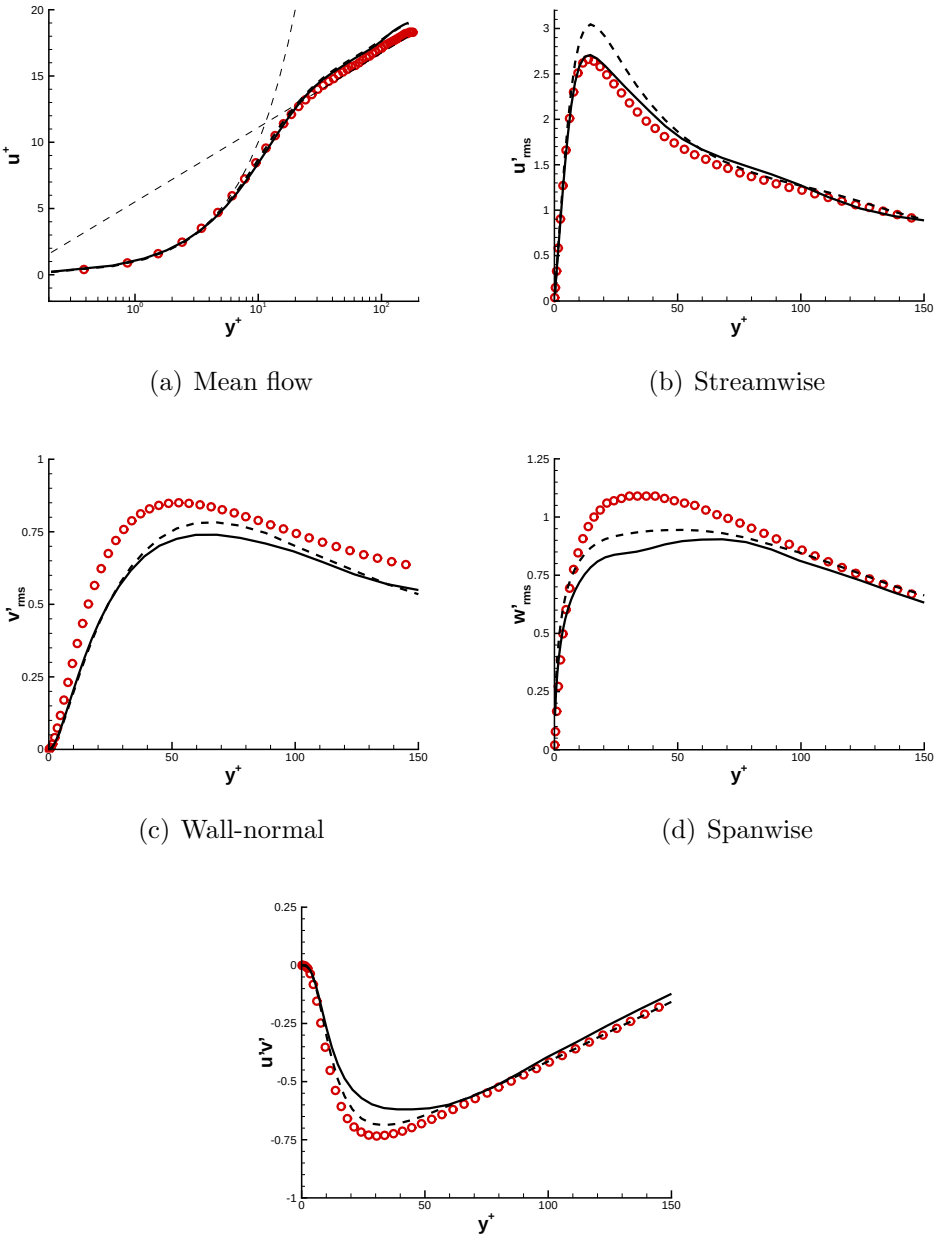

(a) Mean flow

(b) Streamwise

(c) Wall-normal

(d) Spanwise

(e) Shear stress

Figure 5.7: Turbulent statistics (Grid B). dash line: NM, solid line: SM, o: DNS data [37].

Chapter 6

Non-Reacting Bluff-Body flow

Large-eddy simulation (LES) and unsteady Reynolds-averaged Navier-Stokes (URANS) calculations have been performed to investigate the effects of models for scalar variance and its dissipation rate (which were introduced in Chapter 3) as applied to a non-reacting bluff-body turbulent flow. In our new approach, the scalar variance and its dissipation rate are obtained via a coupled system in which the unclosed scalar dissipation rate in the scalar variance equation is modelled either algebraically or by a transport equation. All velocity, time and length scales required to model the scalar dissipation rate are determined using the $k-\varepsilon$ turbulence model for URANS and the Smagorinsky SGS model for LES. The proposed method is first applied to URANS and later to LES.

6.1 Sydney bluff-body non-reacting flow

In consideration of the extension to a reacting case, a non-reacting Sydney bluff-body flow at $Re = 33,333$, which is studied experimentally at the University of Sydney and at Sandia National Laboratories [16], is chosen and simulated using both URANS and LES. The Sydney burner has complex recirculating flows, similar to those found in

practical combustors but with much simpler and well-defined boundary and initial conditions. The Sydney burner has a cylindrical bluff-body with radius $R_b = 25$ mm (or $D_b = 50$ mm) located in a coaxial flow. Along the centerline, a nozzle of radius $R_j = 1.8$ mm ejects air into the recirculation zone. The geometry is shown in Figure 6.1(a). The air speed in the nozzle is $U_{jet} = 61$ m/s and in the coflow is $U_{coflow} = 20$ m/s. As described in [16], the velocity profiles are measured using two-color Laser Doppler Velocimetry (LDV). The experiment reported that the error due to the presence of more than one particle in the measurement volume is believed to be 4% for the mean and 7% for the rms velocity.

The Sydney bluff-body has a very complex flow pattern. A recirculation zone is formed immediately behind the bluff-body wall and it is found that two vortices co-exist in the recirculation zone: an outer vortex close to the air coflow and an inner vortex located between the outer vortex and the jet. Since it is well-known that the standard $k-\varepsilon$ turbulence model fails to predict complex recirculating flows satisfactorily, it will be worthwhile comparing the results of URANS and LES to investigate the potential advantages of using LES in this case.

6.2 Simulation details

The experimental configuration [16] is discretized over a cylindrical computational domain of diameter $10R_b$ and length $6R_b$. To reduce the influence of the boundaries, the computational domain is chosen to be significantly larger than the area of interest. A computational mesh containing $(n_x, n_r, n_\theta) = (75, 45, 34)$ grids in the streamwise, radial and azimuthal directions is initially used for both URANS and LES. By adopting implicit filtering in LES, URANS codes based on the finite volume method can

	LES-A	LES-B	LES-C
$(n_x \times n_r \times n_\theta)$	$75 \times 45 \times 34$	$150 \times 45 \times 34$	$150 \times 60 \times 34$

Table 6.1: Test cases with different grid resolutions for LES.

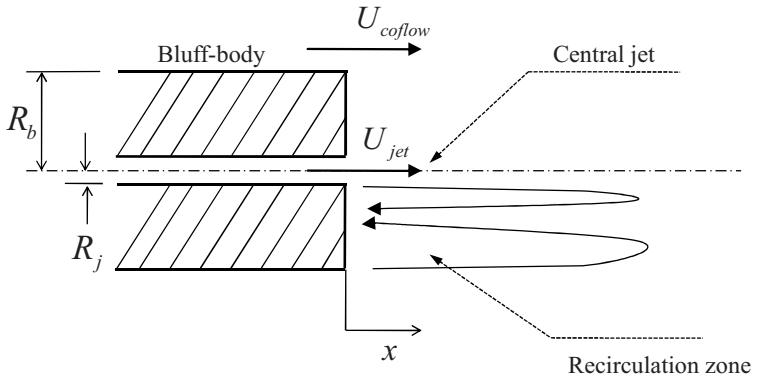

(a) Configuration

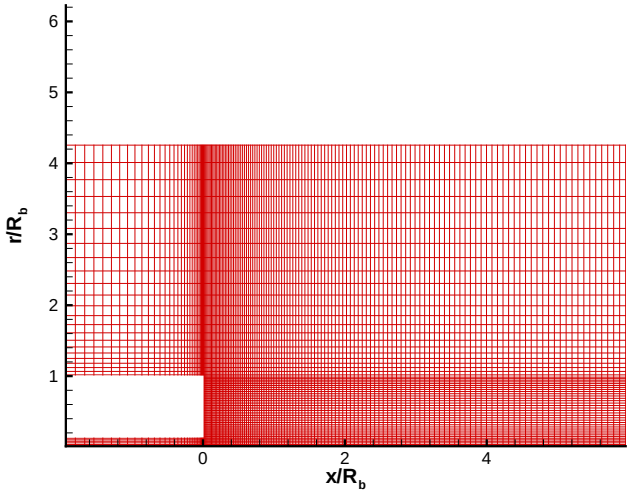

(b) Grid system

Figure 6.1: Configuration of the cylindrical bluff-body burner and grid system.

be easily modified to become LES codes. Hence, the comparative study performed in this work is done using the same grid resolution for both URANS and LES. Although it would not be possible to simulate as many as 3.4 million cells following [71] using the present computational resources in our research group, the effect of different grid resolutions on LES predictions is examined later by varying the grid size along each axis. Test grid resolutions are given in Table 6.1.

A Dirichlet condition is specified at the inflow plane for URANS. For LES, random fluctuations at 10% of the mean flow velocities are added to a uniform velocity profile at the inflow plane, which is placed at $x = -50$ mm (cf. Figure 6.1a) in order to give the flow enough distance to develop. At the outflow plane, a convecting boundary condition for LES and a Neumann condition for URANS are specified. The ambient pressure is set at the shell of the domain, and the pressures at the inflow and outflow planes are specified using the Neumann condition. The Reynolds-averaged or filtered scalar equation (2.54) is solved with the Dirichlet condition specified at the inflow plane and the Neumann condition specified at the lateral and outflow boundaries.

The governing equations are discretized and implemented in the STREAM code [44] using the finite-volume method and the code is parallelized using MPI [87]. While Unsteady RANS (URANS) is performed to capture the unsteadiness at the edge of the bluff-body using the UMIST convection scheme [44], the energy-preserving central difference scheme (CDS) is employed to discretize the convection term in LES. The standard $k - \varepsilon$ turbulence model is used in URANS to close Reynolds stresses, and the Smagorinsky SGS model with the model constant $C_S = 0.1$ is used in LES to model the SGS motions. Although many advanced turbulence models exist in the RANS and LES categories, the standard models for both are used here in order to minimize effects arising from the turbulence modelling which might obscure the behaviour of the scalar variance and its dissipation rate models. Details regarding the boundary/initial conditions and code parallelization can be found in Chapter 4.

6.3 Results

6.3.1 URANS calculation

Previous studies [34, 71] have shown that the burner geometry induces a very complex flow field, and the non-reacting bluff-body (NRBB) case is thus simulated initially.

The predicted radial profiles of the mean and rms velocities at different axial locations ($x/D_b \in 0.2, 0.4, 0.6, 0.8, 1.0, 1.2, 1.4, 1.8, 2.4, .3.4, 4.4, 5.2$) using the standard $k-\varepsilon$ turbulence model are shown in Figures 6.5 to 6.12 and are compared with experimental data [16].

The axial mean velocities in Figures 6.5 and 6.6 show excellent agreement between the predicted and the experimental data up to $x/D_b = 0.6$. However, the mean centerline velocities quickly diffuse, leading to under-prediction further downstream. The reason for the underprediction of the centerline velocity is possibly due to the overestimation of radial diffusion as a result of the $k-\varepsilon$ model being an eddy-viscosity-based turbulence model. The mean radial velocity profiles are presented in Figures 6.7 and 6.8. Similar to the axial mean velocity profiles, the predictions up to $x/D_b = 0.6$ seem fine but severe under-prediction result downstream. Figures 6.9 and 6.10 show a comparison of rms velocity components plotted in the radial direction from the centerline at the same axial locations shown in previous figures. The prediction of the axial and radial rms velocities are arguably satisfactory. Careful inspection reveals that the axial rms velocity is slightly under-predicted but the radial is over-predicted. This is mainly due to the *isotropic assumption* employed in the linear $k-\varepsilon$ model (viz., $\overline{u''^2} = \overline{v''^2} = \frac{2}{3}k$), which is incorrect in complex recirculating flows. As seen in Figures 6.9 and 6.11, there are basically two peaks in velocity; one is along the outer shear layer between the co-flow and outer vortex and the other is along the shear layer between the jet and the inner vortex in the recirculation zone. All figures related to mean and rms velocity profiles collectively demonstrate that the essential features of mean flow field are reasonably captured by the present method.

As seen in Figure 6.2(a), snapshots of the scalar field taken from URANS and LES look quite different, which is expected because most of the turbulence scales in LES are resolved while, in contrast, most of the scales in URANS are modelled. While LES predicts the scalar mean field successfully as shown in Figure 6.2(b), URANS under-predicts it, particularly along the centerline of the nozzle and it becomes worse downstream as shown in Figure 6.13. This under-prediction in URANS is likely caused by the over-estimation of the eddy viscosity in the standard $k-\varepsilon$ model, a

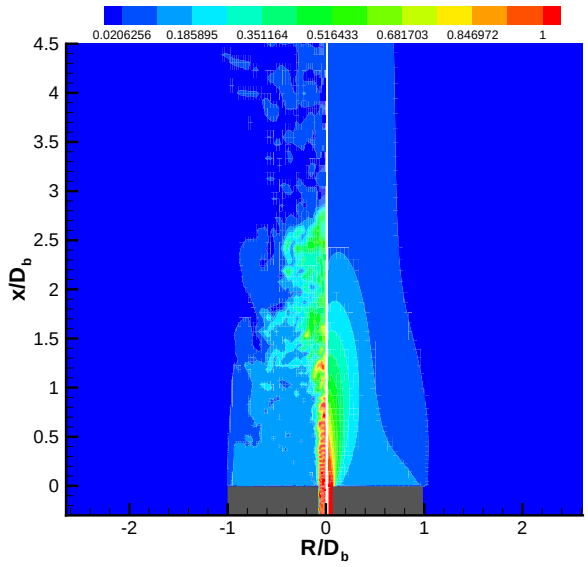

(a) Scalar mean field

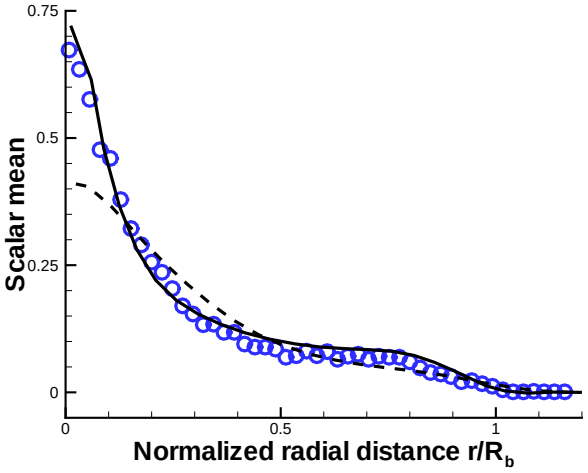

(b) $x/D_b = 0.6$

Figure 6.2: Scalar mean field comparison of URANS and LES. (a) left: LES, right: URANS (b) o: experimental data [16], dash: URANS, solid: LES.

well-known deficiency associated with most eddy-viscosity-based RANS models.

The scalar variance equation (Eq. (3.6)) is solved in conjunction with two different scalar dissipation rate models. One is the algebraic model, Eq. (3.12), and the other is the transport equation model, Eq. (3.16), which involves four empirical constants. The initial model constants referred to as Case 1 in Table 6.2 are taken from Jones and Musonge [31]. As shown in Figure 6.14, Case 1 significantly over-predicts the scalar variance. One possible explanation for this over-prediction is that the model constants were originally calibrated for a homogeneous turbulent flow. Therefore, the model constants need to be re-calibrated in the present study due to the non-homogeneity of the target flow. Only C_1 and C_3, which are associated with scalar production and destruction, are re-calibrated, as shown in Table 6.2. The rationale for this approach is that gradients of mean velocity field and gradients of scalar mean field differ greatly between homogeneous and inhomogeneous flows. Since, in Eq. (3.16), the production term (III) is closely coupled to the gradients of scalar mean field and the destruction term (I) is sensitive to the scalar variance field, the associated model constants C_1 and C_3 require re-calibration.

Figure 6.14 shows the scalar variance predictions at four different locations ($x/D_b =$ 0.4, 0.6, 0.8 and 1.0) with different sets of model constants. It is observed that Case 1 significantly over-predicts scalar variance and Case 2 conforms the best with the experimental data. Case 3, which doubles the scalar production term compared to Case 1, and Case 4, which halves the scalar destruction term compared to Case 1, yield very similar results, which are approximately an average of the results for Cases

	C_1	C_2	C_3	C_4
Case 1	2.0	1.8	1.7	1.4
Case 2	1.0	1.8	3.4	1.4
Case 3	2.0	1.8	3.4	1.4
Case 4	1.0	1.8	1.7	1.4

Table 6.2: Test cases with different model constants for the scalar dissipation rate transport equation.

1 and 2. In this manner, one may conclude that decreasing the destruction term (I) or increasing the production term (III) in Eq. (3.16) has similar effects on the generation of the scalar variance.

In order to see how each source/sink term contributes to Eq. (3.16), the magnitude of each source/sink term in the equation is compared in Figure 6.3. Obviously Case 2 predicts a higher scalar dissipation rate than Case 1. This explains why Case 2 predicts lower scalar variance than Case 1, as shown in Figure 6.14. In Figure 6.3, Case 2 predicts the peak value of the scalar dissipation rate to be about 22% higher than Case 1. This difference in turn leads to approximately 40% difference in peak values of the scalar variance. In this regard, it can be said that the scalar variance prediction is quite sensitive to the value of the scalar dissipation rate, which requires accurate modelling.

The algebraic model shows relatively good results in Figure 6.15, but it is obvious that the prediction worsens downstream. This under-prediction seems to be attributed to the flow prediction by the two-equation model. As shown in Figures 6.5 to Figure 6.9, the mean and rms results under-predict experimental data. It is well known that the two-equation model over-predicts the spreading rate of the round-jet so that the solution of the two-equation model becomes more diffusive. This flow field prediction actually affects the scalar mean field seen in Figure 6.13, where the scalar mean is under-predicted particularly along the centerline.

The scalar variances predicted by the algebraic model and the transport equation model (Case 2) are compared in Figure 6.15. Overall, prediction using both the algebraic and transport-model predictions agree reasonably well with experimental data. Careful examination reveals that predictions using the algebraic model deviate more from the experiment in the range $0 \leq r/R_b \lesssim 0.5$ close to the centerline, particularly at downstream locations (at $x/D_b = 0.8$ and 1.0). This under-prediction appears to be attributed to the well-known weaknesses of the two-equation $k - \varepsilon$ RANS model. Basically, the algebraic model assumes that the scalar time scale is proportional to the mechanical time scale. Therefore, under-prediction of the mechanical time scale

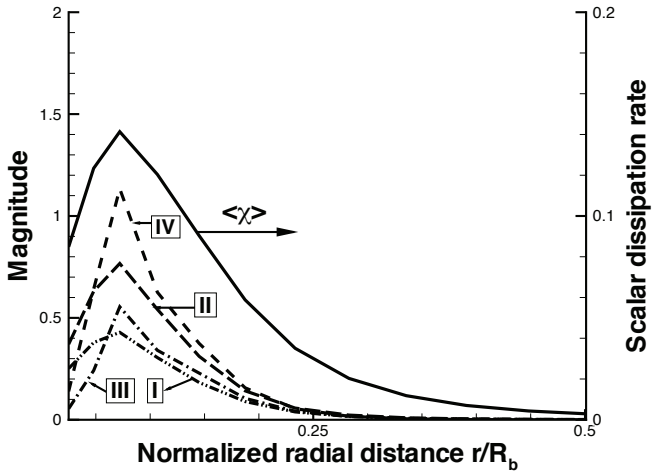

(a) Case 1

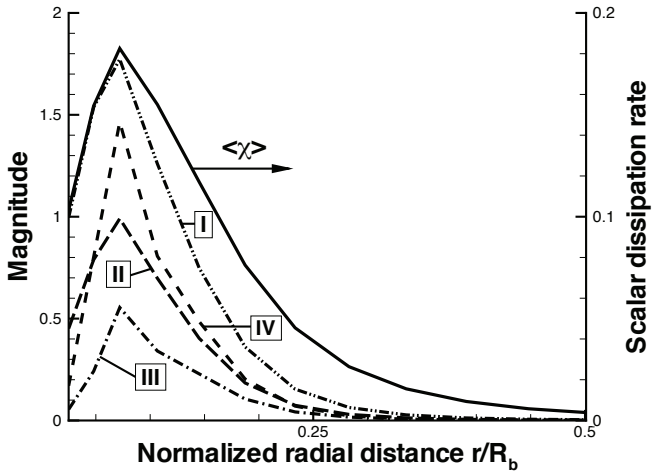

(b) Case 2

Figure 6.3: Comparison of time-averaged individual term contribution in the scalar dissipation rate transport equation at $x/D_b = 0.4$ using URANS. dash-dot-dot: scalar destruction (I), long-dash: turbulence destruction (II), dash-dot: scalar production (III), dash: turbulence production (IV), solid: scalar dissipation rate.

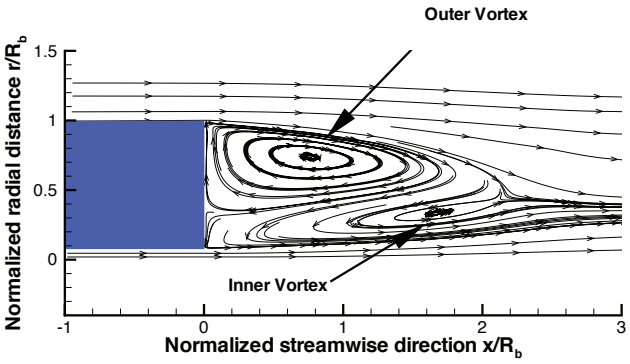

Figure 6.4: Streamline patterns close to the edge of a bluff-body burner predicted by URANS.

leads to over-prediction of the scalar dissipation rate and, hence, under-prediction of the scalar variance.

As expected, the transport equation model shows its strength in better predicting the scalar variance at downstream locations (at $x/D_b = 0.8$ and 1.0). At the stations close to the edge of a bluff-body burner (at $x/D_b = 0.4$ and 0.6; cf. Figure 6.4), however, both models over-predict the scalar variance, especially in the range $0.2 \lesssim r/R_b \lesssim 0.7$. As a result, the distribution of scalar variance is still not properly captured by either of the scalar dissipation rate models used in URANS.

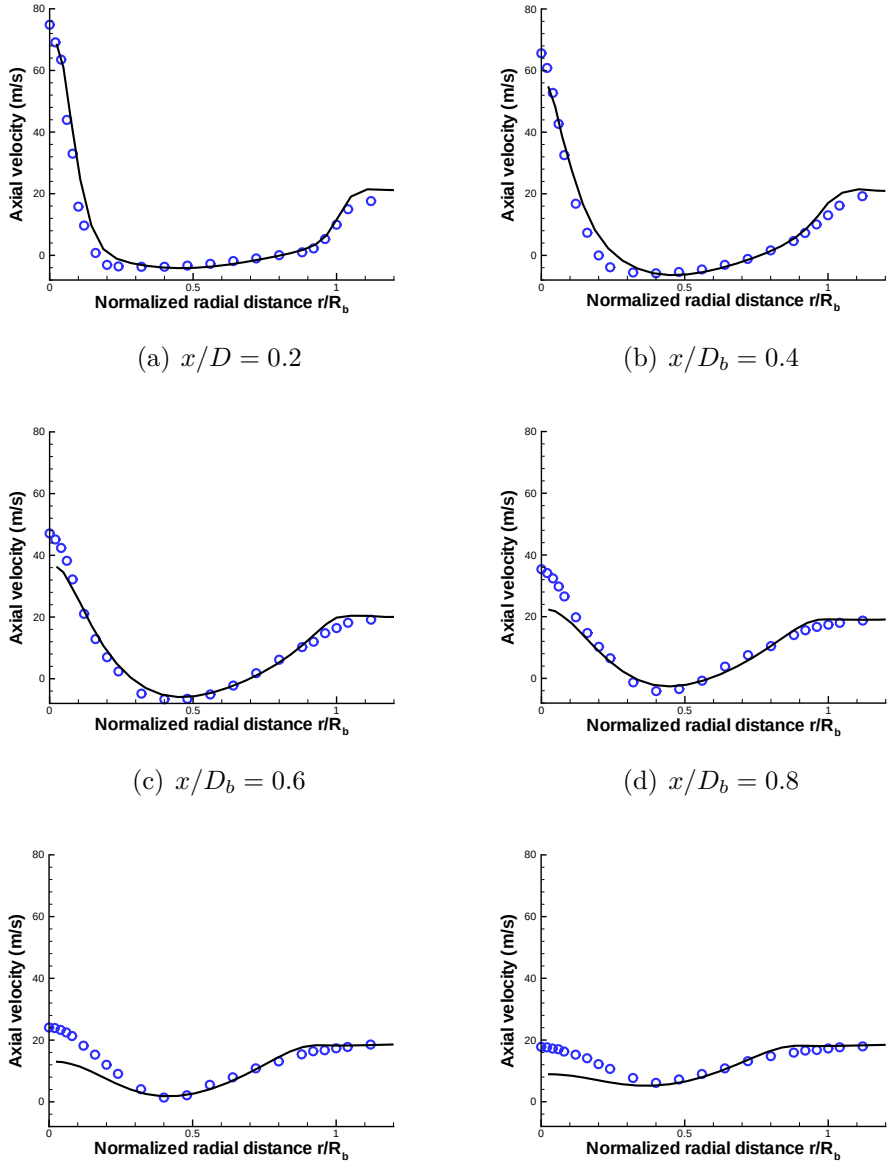

(a) $x/D = 0.2$ (b) $x/D_b = 0.4$

(c) $x/D_b = 0.6$ (d) $x/D_b = 0.8$

(e) $x/D_b = 1.0$ (f) $x/D_b = 1.2$

Figure 6.5: Comparison of axial mean velocities at $x/D_b = 0.2, 0.4, 0.6, 0.8, 1.0, 1.2$ in the NRBB case using URANS. o: experimental data [16], solid: URANS calculation.

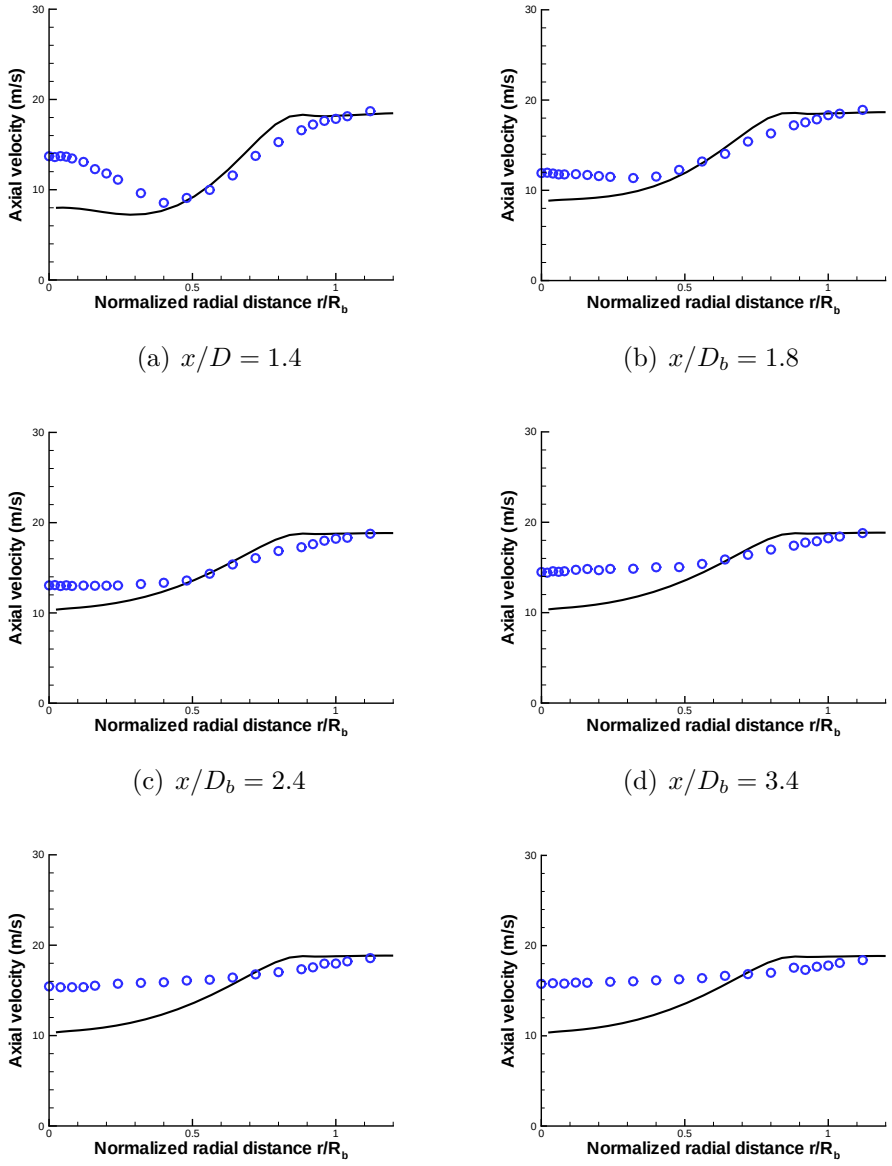

(a) $x/D = 1.4$ (b) $x/D_b = 1.8$

(c) $x/D_b = 2.4$ (d) $x/D_b = 3.4$

(e) $x/D_b = 4.4$ (f) $x/D_b = 5.2$

Figure 6.6: Comparison of axial mean velocities at $x/D_b = 1.4, 1.8, 2.4, 3.4, 4.4, 5.2$ in the NRBB case using URANS. o: experimental data [16], solid: URANS calculation.

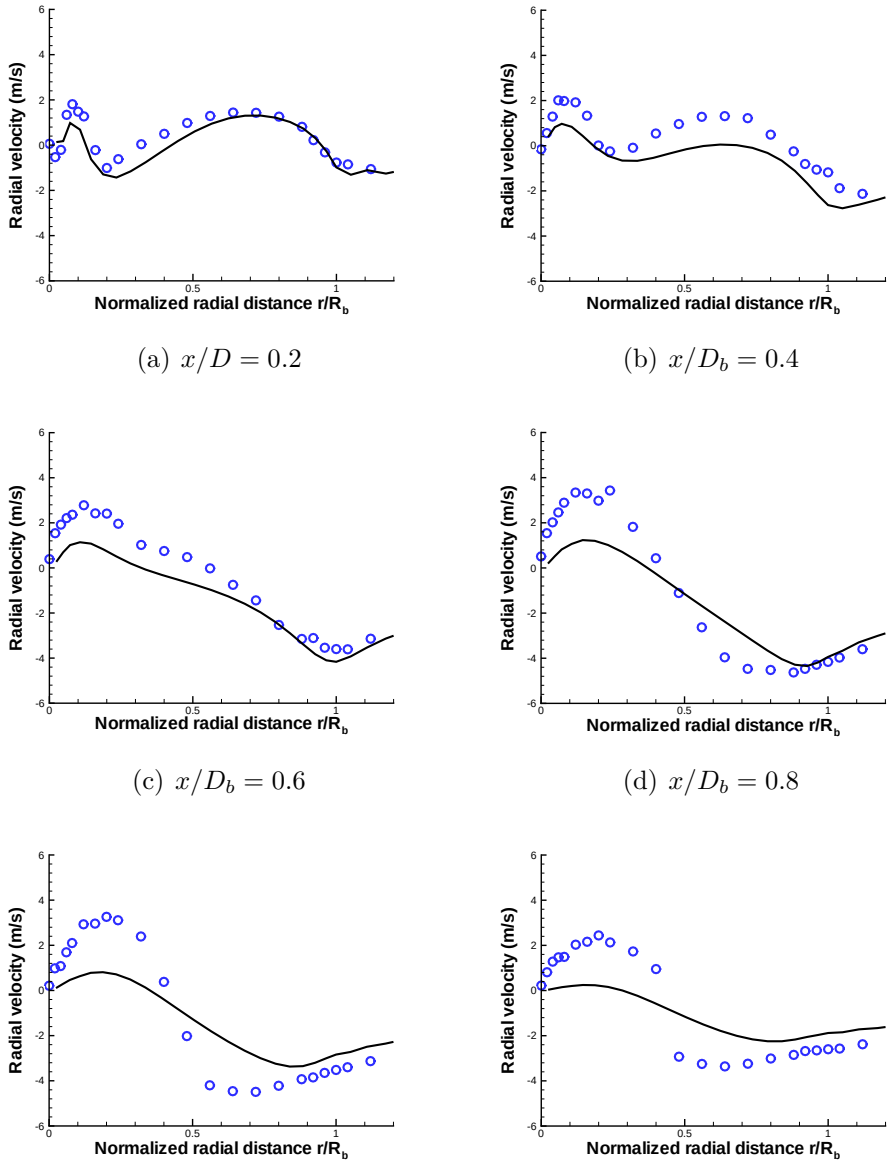

(a) $x/D = 0.2$ (b) $x/D_b = 0.4$

(c) $x/D_b = 0.6$ (d) $x/D_b = 0.8$

(e) $x/D_b = 1.0$ (f) $x/D_b = 1.2$

Figure 6.7: Comparison of radial mean velocities at $x/D_b = 0.2, 0.4, 0.6, 0.8, 1.0, 1.2$ in the NRBB case using URANS. o: experimental data [16], solid: URANS calculation.

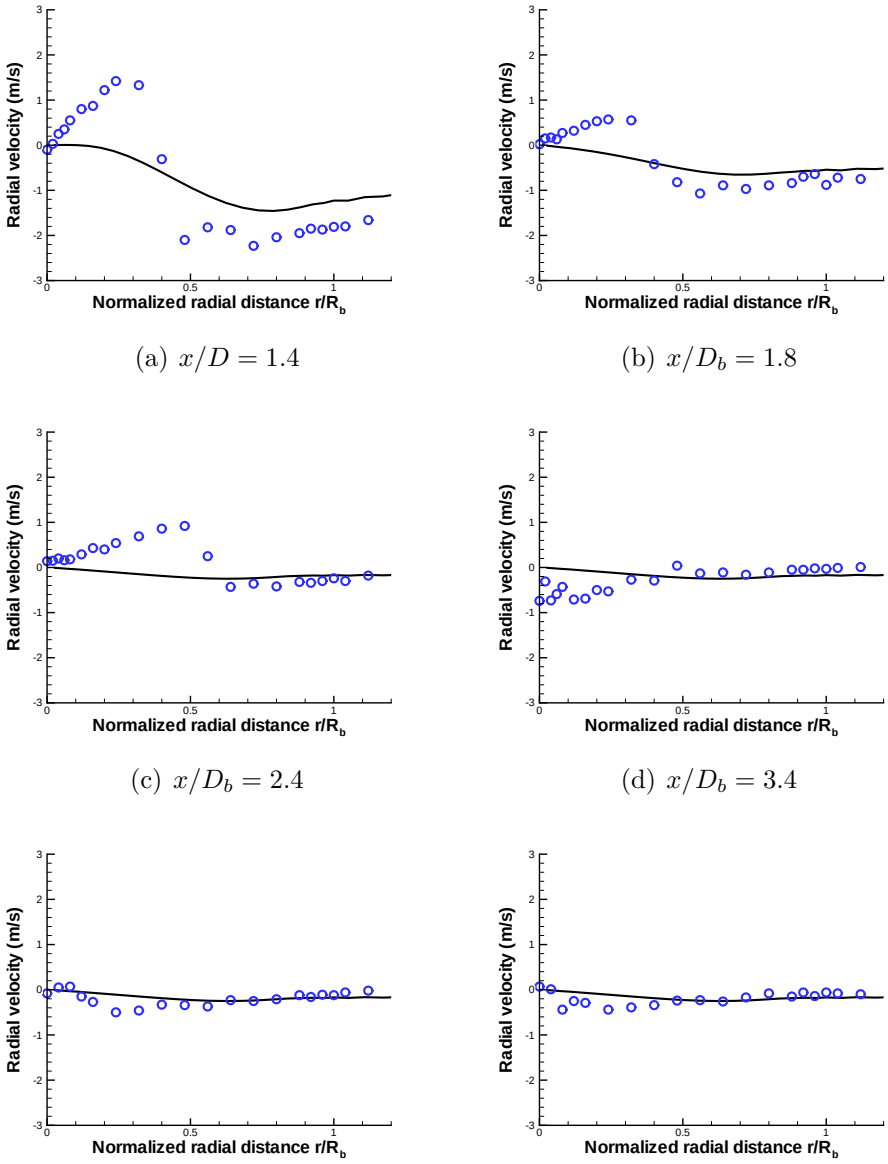

(a) $x/D = 1.4$ (b) $x/D_b = 1.8$

(c) $x/D_b = 2.4$ (d) $x/D_b = 3.4$

(e) $x/D_b = 4.4$ (f) $x/D_b = 5.2$

Figure 6.8: Comparison of radial mean velocities at $x/D_b = 1.4, 1.8, 2.4, 3.4, 4.4, 5.2$ in the NRBB case using URANS. o: experimental data [16], solid: URANS calculation.

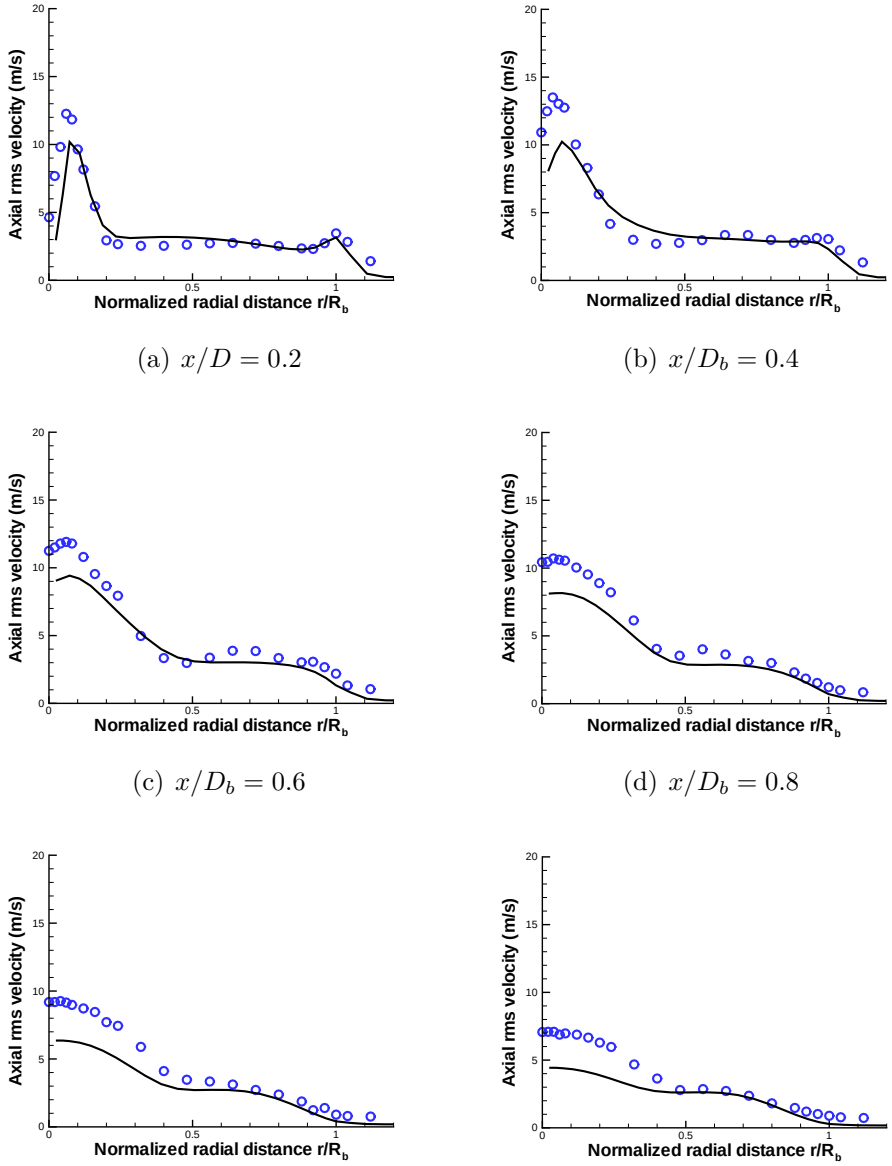

(a) $x/D = 0.2$

(b) $x/D_b = 0.4$

(c) $x/D_b = 0.6$

(d) $x/D_b = 0.8$

(e) $x/D_b = 1.0$

(f) $x/D_b = 1.2$

Figure 6.9: Comparison of axial rms velocities at $x/D_b = 0.2, 0.4, 0.6, 0.8, 1.0, 1.2$ in the NRBB case using URANS. o: experimental data [16], solid: URANS calculation.

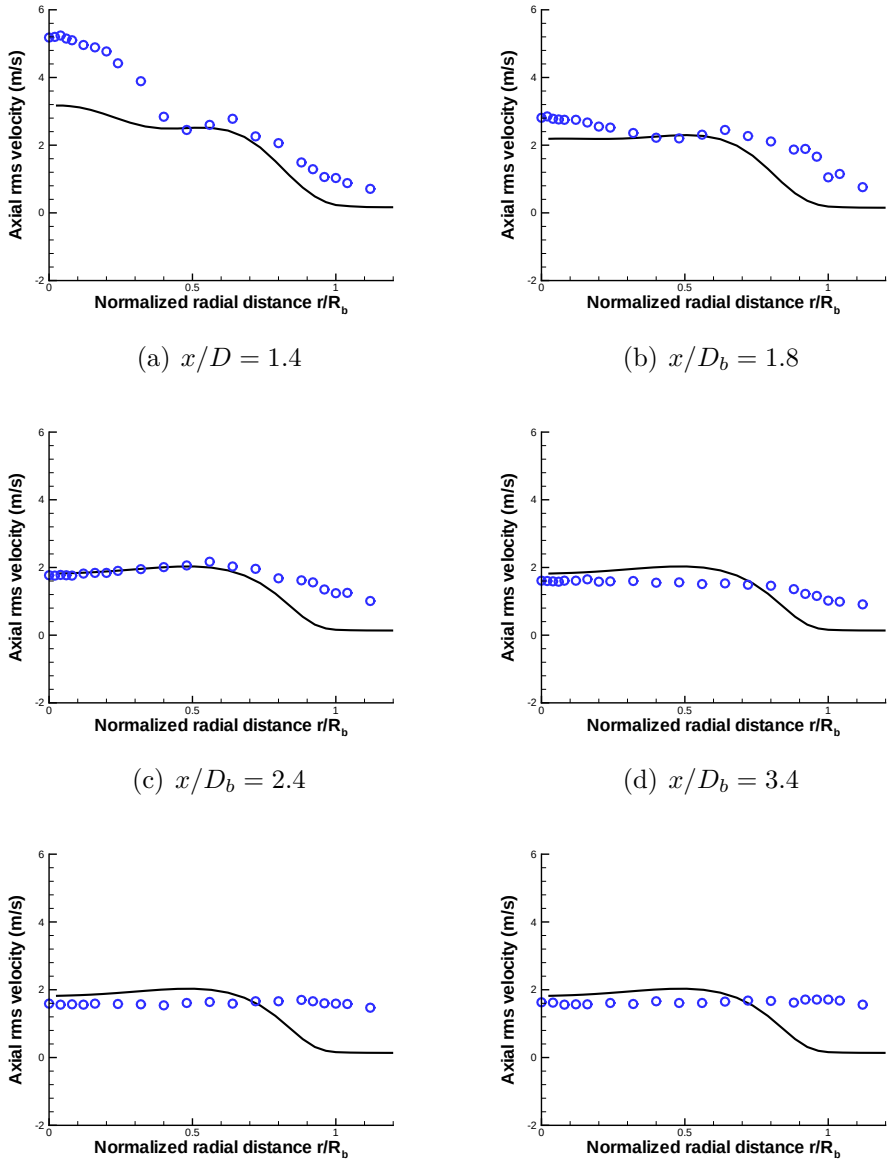

(a) $x/D = 1.4$ (b) $x/D_b = 1.8$

(c) $x/D_b = 2.4$ (d) $x/D_b = 3.4$

(e) $x/D_b = 4.4$ (f) $x/D_b = 5.2$

Figure 6.10: Comparison of axial rms velocities at $x/D_b = 1.4, 1.8, 2.4, 3.4, 4.4, 5.2$ in the NRBB case using URANS. o: experimental data [16], solid: URANS calculation.

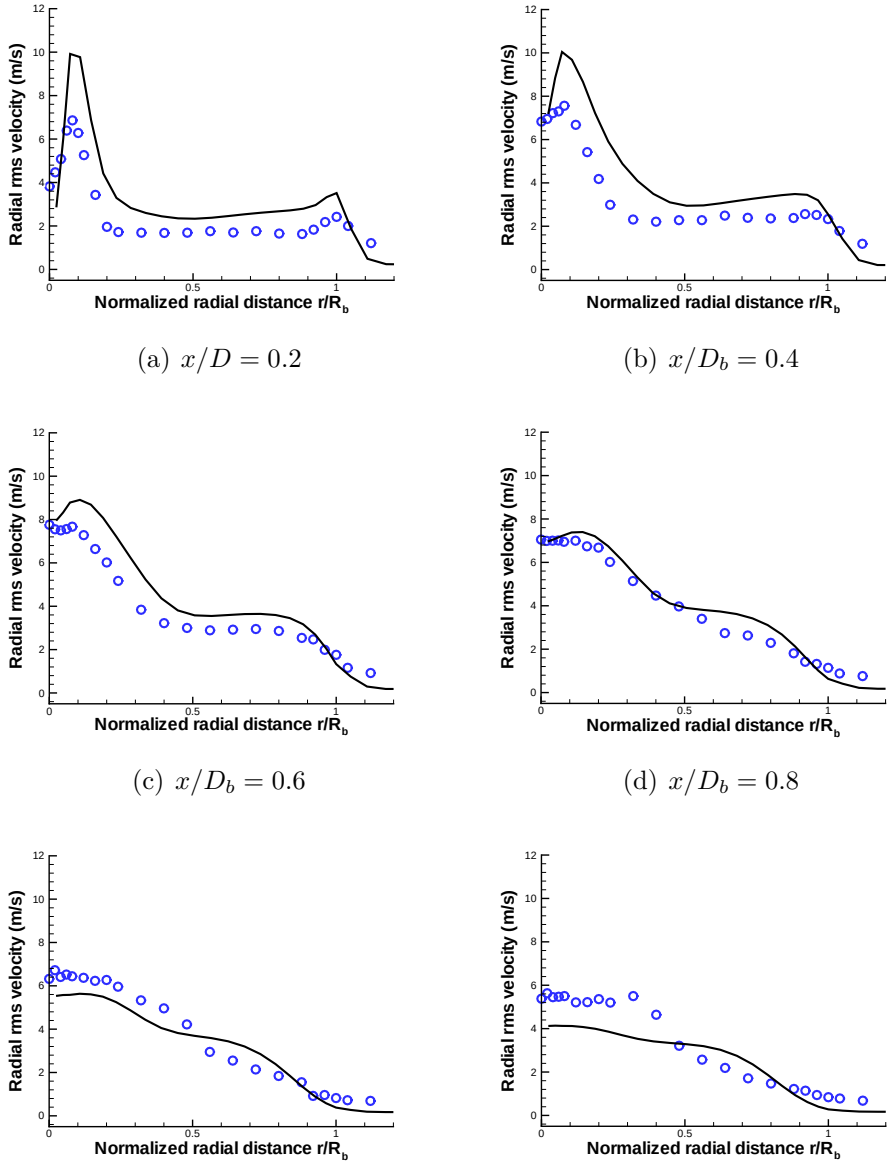

(a) $x/D = 0.2$

(b) $x/D_b = 0.4$

(c) $x/D_b = 0.6$

(d) $x/D_b = 0.8$

(e) $x/D_b = 1.0$

(f) $x/D_b = 1.2$

Figure 6.11: Comparison of radial rms velocities at $x/D_b = 0.2, 0.4, 0.6, 0.8, 1.0, 1.2$ in the NRBB case using URANS. o: experimental data [16], solid: URANS calculation.

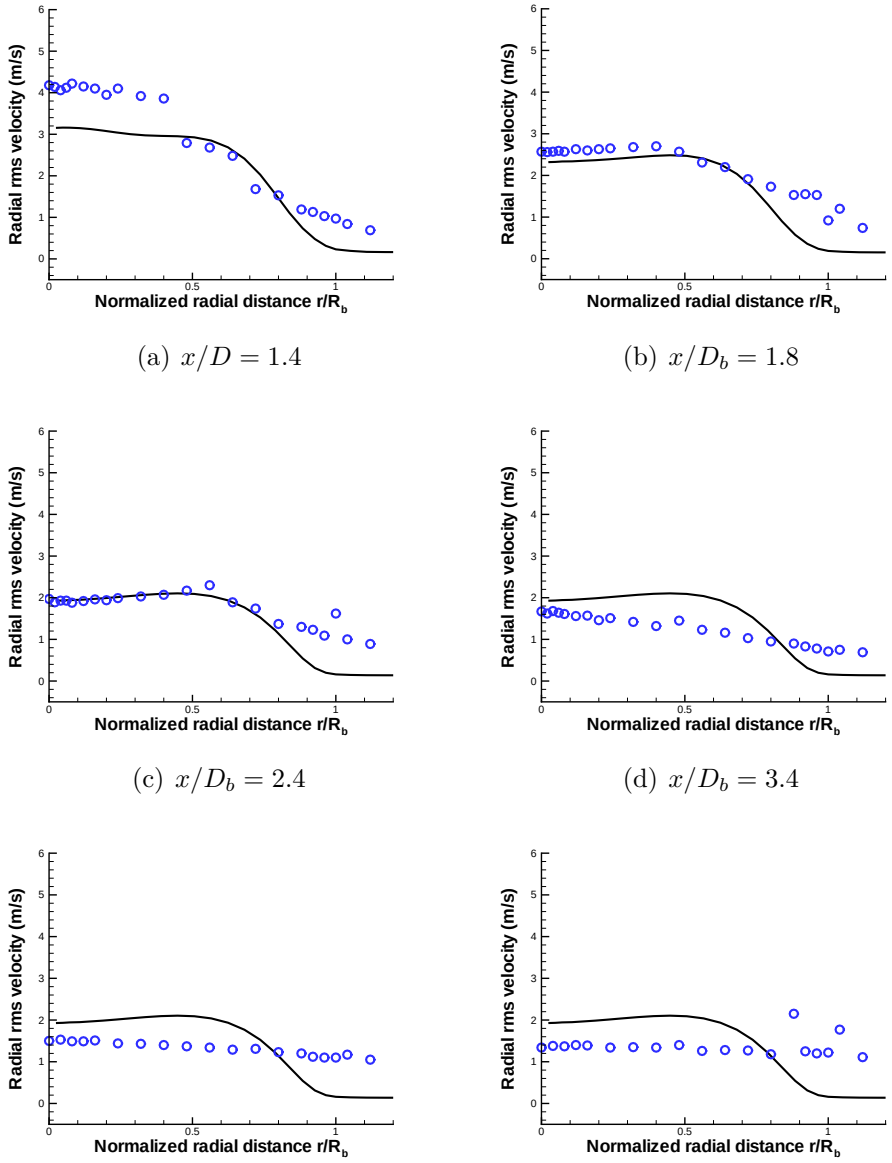

(a) $x/D = 1.4$ (b) $x/D_b = 1.8$

(c) $x/D_b = 2.4$ (d) $x/D_b = 3.4$

(e) $x/D_b = 4.4$ (f) $x/D_b = 5.2$

Figure 6.12: Comparison of radial rms velocities at $x/D_b = 1.4, 1.8, 2.4, 3.4, 4.4, 5.2$ in the NRBB case using URANS. o: experimental data [16], solid: URANS calculation.

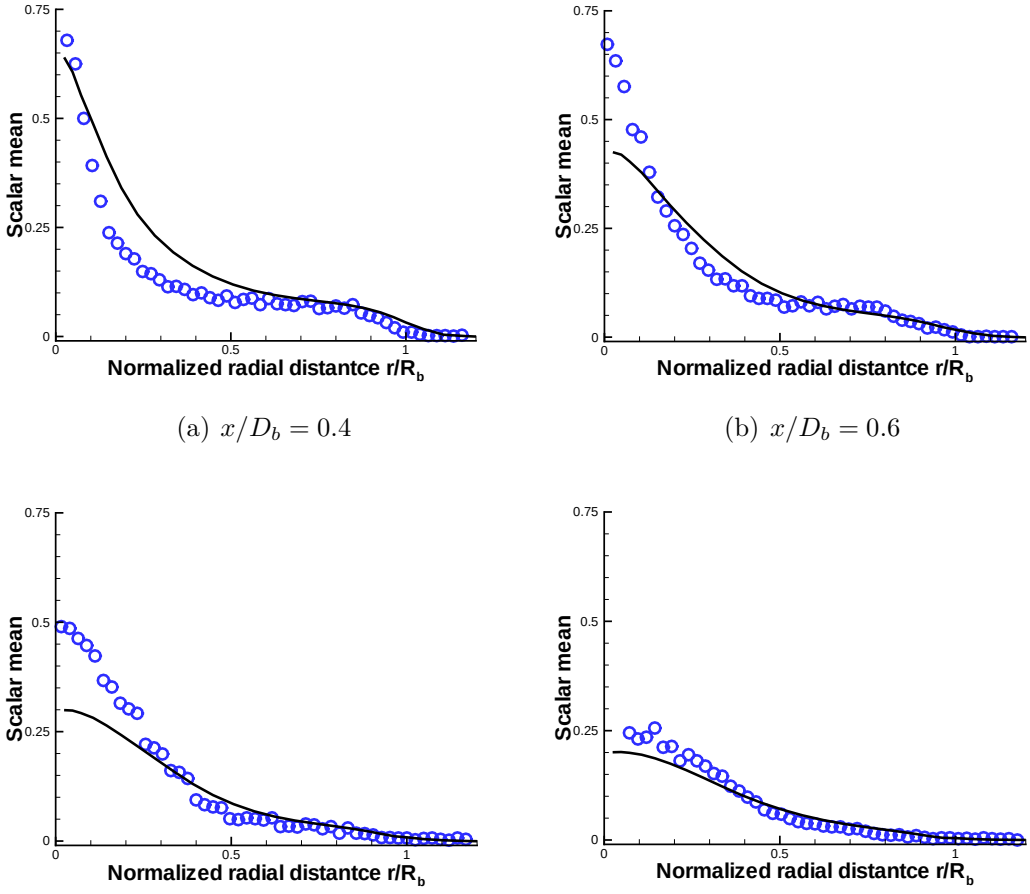

(a) $x/D_b = 0.4$

(b) $x/D_b = 0.6$

(c) $x/D_b = 0.8$

(d) $x/D_b = 1.0$

Figure 6.13: Scalar mean prediction at $x/D_b = 0.4, 0.6, 0.8, 1.0$ in the NRBB case using URANS. o: experimental data [16], dash: URANS calculation.

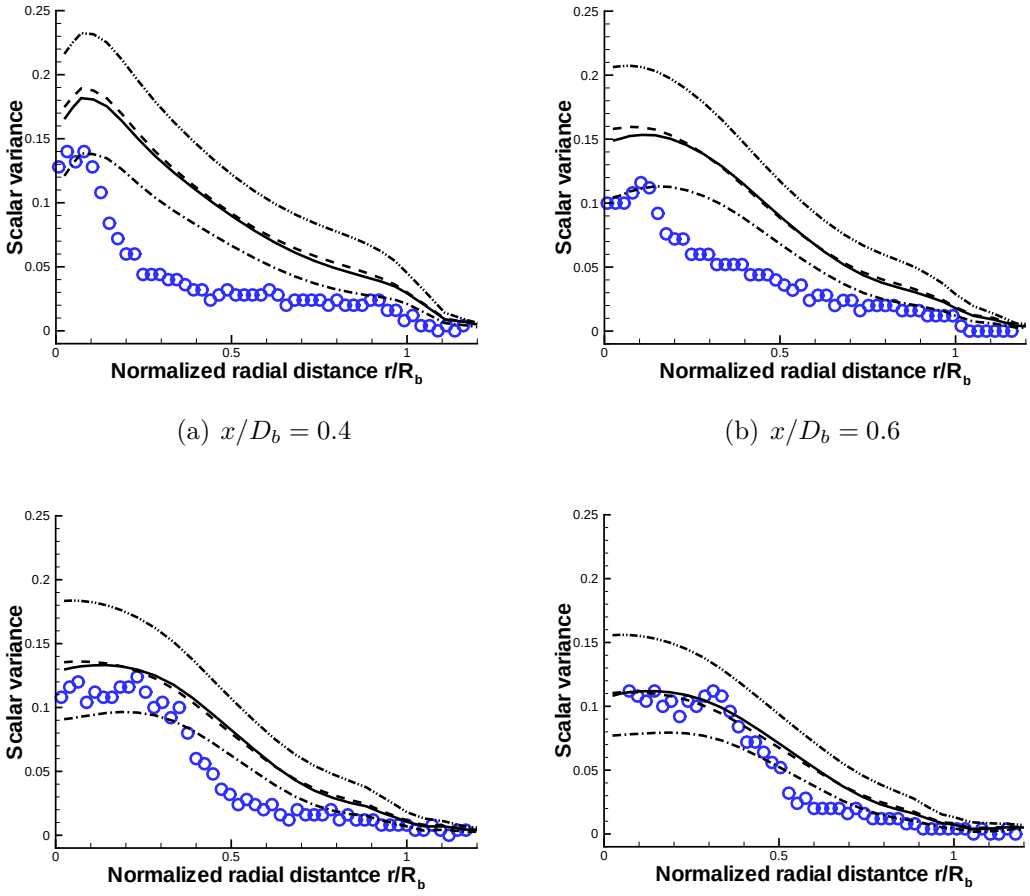

(a) $x/D_b = 0.4$

(b) $x/D_b = 0.6$

(c) $x/D_b = 0.8$

(d) $x/D_b = 1.0$

Figure 6.14: Scalar variance prediction at $x/D_b = 0.4, 0.6, 0.8, 1.0$ by solving the scalar dissipation rate transport equation with different model constants in URANS. o: experimental data [16], dash-dot-dot: Case 1 [31], dash-dot: Case 2, dash: Case 3, solid: Case 4.

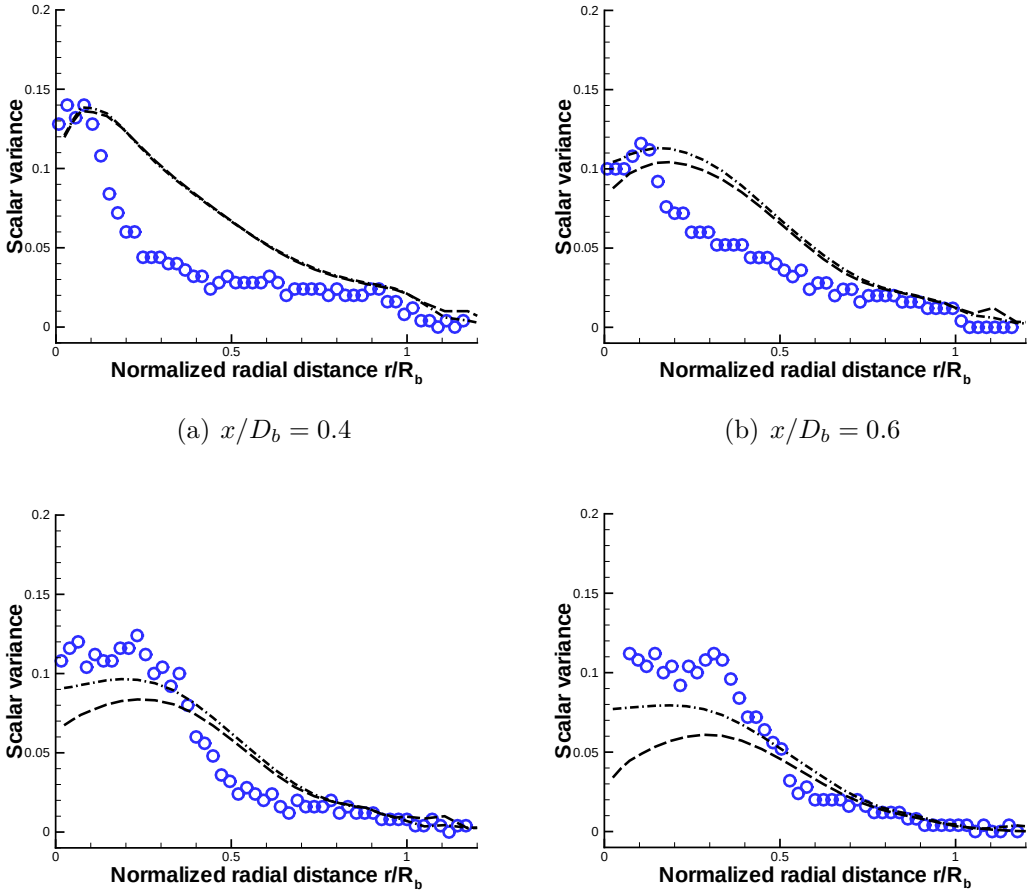

(a) $x/D_b = 0.4$

(b) $x/D_b = 0.6$

(c) $x/D_b = 0.8$

(d) $x/D_b = 1.0$

Figure 6.15: Scalar variance prediction at $x/D_b = 0.4, 0.6, 0.8, 1.0$ by the algebraic and the transport model in URANS. o: experimental data [16], long-dash: algebraic model, dash-dot: transport equation model (Case 2).

6.3.2 LES calculation

The axial and radial velocities at the same axial positions used in the LES calculations are presented in Figures 6.18 to 6.25. Note that all results in the LES calculations including the SGS scalar variance and SGS scalar dissipation rate are time-averaged and compared with experiment data. As explained above, three different grid resolutions listed in Table 6.1 are used to examine the grid dependency of the predicted results. All simulations are done with the Smagorinsky SGS model with $C_S = 0.1$.

Firstly, it is clear that the axial mean velocity profiles (LES-A) are improved compared to URANS results which are shown in Figures 6.5 to 6.6. It should be recalled that LES-A has same grid resolution as the URANS calculation. Although LES-A slightly over-predicts the axial mean velocities at $0.2 \leq r/R_b \leq 0.6$ at $x/D_b = 0.2$ and 0.4, the predicted centerline velocities are less diffusive downstream, where URANS under-predicts the axial mean velocities severely. Among the three grid resolutions, LES-C shows the best agreement with experimental data. This is somewhat expected, since the Smagorinsky SGS model sets a length scale using the grid size. Nevertheless, all three LES results are quite similar. Figures 6.20 to 6.21 present radial mean velocity profiles. Compared with URANS, LES-A shows quite similar predictions over the entire domain. Furthermore, the two other LES calculations show hardly any improvement in predicting the radial mean velocities. Recent LES studies [34, 71] also reported a difficulty in predicting the radial velocity profiles. Raman and Pitsch [71] noted that there seems to be a significant experimental discrepancy [56] and Kempf *et al.* [34] mentioned that there is great sensitivity in the flow immediately after the re-circulation zone. Further investigation refining the azimuthal direction is certainly required.

The axial and radial rms velocity profiles are shown in Figures 6.22 to 6.25. Overall prediction of LES calculations seems to be better than URANS. In the axial rms velocity predictions, LES-A gives a less diffusive prediction along the centerline than URANS. The axial rms velocities are slightly over-predicted along the centerline and under-predicted at $0.07 \lesssim r/R_b \lesssim 1.0$ up to $x/D_b = 1.0$. This issue is resolved

by refining the grid resolution so that LES-B and LES-C show excellent agreement with experimental data. The peak of the axial rms velocity is slightly over-predicted, though. All LES calculations predict the axial rms velocity profiles quite well until $x/D_b = 2.4$ but over-predict them afterwards. The radial rms profiles are predicted well by all three LES calculations. It is commonly noticed among all calculations that the centerline rms profiles are slightly over-predicted. Consequently, it is apparent that LES calculations give better prediction of the mean and rms velocity profiles than URANS. Furthermore, the finest grid resolution (LES-C) shows the best prediction. However, in author's opinion, no great difference in predicting the low order statistics of turbulence is found in this study.

The scalar mean fields that are obtained by solving its own transport equation are presented in Figure. 6.26. All three different grid resolutions predict the scalar mean field well until $x/D_b = 0.8$ and over-predict it afterwards. The over-prediction downstream seems to be attributed to the over-prediction of the rms values in flow field. All results are very close to each other and the marginal variations near the interface of the inner- and outer-vortex are noticed.

For a comparative study of using URANS and LES, the scalar variance in LES is obtained using a similar approach as that used in URANS. The scalar variance equation (Eq. (3.20)) is solved using two different scalar dissipation rate models: the algebraic model (Eq. (3.28)) and the transport equation model (Eq. (3.31)). Here $C_D = 0.17$ in Eq. (3.28) and $R_\tau = 2.0$ in Eq. (3.28) are used.

The calibration of the model constants C_1, C_2, C_3 and C_4 in Eq. (3.31) is first performed using the same test matrix listed in Table 6.2. The scalar variance predictions according to these test cases are shown in Figure 6.27. While Case 1 over-predicts and Case 2 under-predicts the scalar variance, both Case 3 and Case 4 give fairly good agreement with the experiment. It is also noticed that Case 3 and Case 4 yield very similar results, as noticed in Figure 6.14 for URANS calculations, and are the best results among the four cases examined here. Comparing these LES results with those predicted by URANS (Figure 6.14), it is found that the scalar variance predicted by LES for each case is generally lower than those in the URANS solutions.

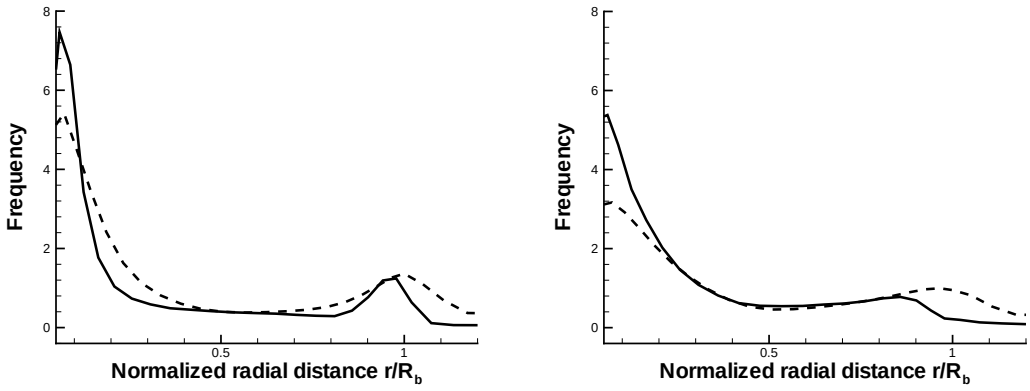

(a) $x/D_b = 0.4$ (b) $x/D_b = 0.6$

Figure 6.16: Turbulence frequencies obtained with URANS and LES. dash: URANS, solid: LES.

Recall that all equations used in URANS and LES have similar forms (cf. Eqs. (3.16) and (3.31)). This difference in prediction of the scalar variance is likely due to the different turbulence time scales employed by URANS and LES.

The turbulence time scales (or reciprocal of the turbulence frequencies) in URANS and LES are presented in Figure 6.16 using the profiles of the corresponding turbulence frequency ($\widetilde{\varepsilon}/\widetilde{k}$ for URANS and $\widetilde{\varepsilon}_{sgs}/\widetilde{k}_{sgs}$ for LES) at $x/D_b = 0.4$ and 0.6. The turbulence frequency in LES shows higher maximum values than in URANS, particularly along the nozzle centerline at $r/R_b = 0$. This means that the turbulence eddy-turn-over time (which is inversely proportional to the frequency) in LES is shorter than that in URANS. This higher turbulence frequency in LES appears to lead to a higher scalar dissipation rate and, hence, to lower scalar variance.

Figure 6.28 compares the scalar variance predicted by the new algebraic model and by the new transport equation model (Case 3) for the scalar dissipation rate with the grid resolution of LES-A. The algebraic model under-predicts the scalar variance over most of the domain and the results become fairly diffusive at downstream locations (at $x/D_b = 0.8$ and 1.0). The transport equation model for the scalar dissipation rate

yields very good scalar variance predictions in comparison with experimental data as shown in Figure 6.28, and it can reproduce the variation of the scalar variance along the nozzle centerline where URANS fails to do so. Moreover, the over-prediction of scalar variance by URANS close to the edge of the bluff-body burner at $x/D_b = 0.4$ and 0.6 in the range $0.2 \lesssim r/R_b \lesssim 0.7$ shown in Figure 6.15 is drastically improved using the transport-equation LES model, particularly in conjunction with the Case 3 model constants (cf. Figure 6.28).

One of the major objectives of this study is to demonstrate the superiority of the new LES approach, which solves the scalar variance equation with either the algebraic or the transport equation model for the scalar dissipation rate, over the existing algebraic scalar variance models employed in the LES community. To this end, the scale similarity model and the gradient-based model for scalar variance are employed in this study only for comparison purposes. Predictions using both models are shown in Figure 6.29. The scale similarity model constant $C_{ss} = 0.1$ is taken from [13]. The dynamic procedure [23] is used to determine the constant C_g in the gradient-based model. Both existing algebraic-type models severely under-predict the scalar variance over the entire domain. It is obvious that the new transport model for the scalar dissipation rate in conjunction with the scalar variance transport equation gives the best conformance to the experiment. It should be noted that both the scale similarity and gradient-based models calculate the scalar variance directly without explicitly involving the scalar dissipation rate.

The performance of using different approaches for the prediction of scalar variance in LES is compared by constructing the β-function probability density function (PDF) at (x, r) =(25 mm, 2.5 mm). The corresponding PDF shapes are presented in Figure 6.17. It can be seen that the shape of the PDF is fairly sensitive to the value of scalar variance. While the PDF from experimental data at this location shows an unmixed condition between the scalar and the air (as indicated by two peaks at $Z = 1$ and 0, respectively), the scale similarity model and the gradient-based model, which under-predict the scalar variance, show a certain amount of mixing. In contrast to these two algebraic models, the new approach of solving both the scalar variance

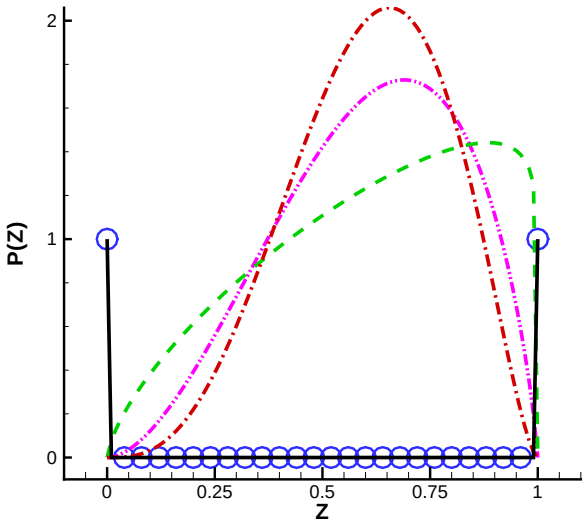

Figure 6.17: β-function PDF shapes obtained with various LES approaches at (x, r)=(25 mm,2.5 mm). o: experimental data, dash: gradient-based model, dash-dot-dot: scale similarity model, dash-dot: scalar variance transport equation with algebraic scalar dissipation rate model, solid: scalar variance transport equation with scalar dissipation rate transport model.

and the scalar dissipation rate transport equations reproduces the unmixed condition successfully, which is very encouraging. It is anticipated that our proposed approach for solving scalar variance will improve predictions for reacting flows as well.

Since our new scalar dissipation rate models employ a turbulent time scale consistent with the Smagorinsky SGS model, in which the filter width is related to the grid spacing, it is important to study how different grid resolutions affect predictions of scalar mean and variance. Three different grid sizes listed in Table 6.1 are adopted for the grid sensitivity study.

Figures 6.30(a) and (c) show the predicted scalar mean field. The scalar mean field seems to be fairly insensitive to the different grid sizes investigated, but a slight

difference is noticed in the range $0.1 \lesssim r/R_b \lesssim 0.5$ where the inner vortex (close to the jet) and the outer vortex (adjacent to the air coflow) meet at $r/R_b \approx 0.3$ (cf. Figure 6.4). The scalar variances are shown in Figures 6.30 (b) and (d). The scalar variance field is slightly more sensitive to the grid resolution. Comparing the LES-A and LES-B cases, in which n_x(LES-A)/n_x(LES-B) = 1/2, the finer grid resolution in the streamwise direction gives lower predictions of the scalar variance. This is reasonable because the eddy turn-over time in the resolved scale becomes smaller or, equivalently, the corresponding turbulence frequency becomes higher. As shown in Figure 6.16, higher turbulence frequency leads to higher scalar dissipation rate, resulting in a decrease in the scalar variance. This deficiency might be improved if the Smagorinsky SGS model constant is determined by the dynamic procedure [23].

Comparison of predicted scalar variance obtained with two URANS and two LES models (all of which solve the scalar variance from its own transport equation) is shown in Figure 6.31. As can be seen, the major deficiency with the URANS algebraic model is that scalar variance is under-predicted along the nozzle centerline, particularly at downstream stations. For example, scalar variance is under-predicted by a factor of about two compared to the experiment for $0 \leq r/R_b \lesssim 0.3$ at $x/D_b = 1.0$. This deficiency is likely linked to the well-known deficiency of the two-equation $k-\varepsilon$ turbulence model, which tends to overestimate the spreading rate of a round jet i.e., a flow in which the diffusion process plays a very important role. Furthermore, it is also noticed that the algebraic URANS model fails to reproduce the shape of scalar variance distribution in the range of $0.2 \lesssim r/R_b \lesssim 0.7$. Although the algebraic LES model under-predicts the scalar variance at all four stations examined likely due to insufficient grid resolution, the shape of scalar variance distribution near the edge of the bluff-body burner (at $x/D_b = 0.4$ and 0.6) is much better depicted in comparison with the algebraic URANS model.

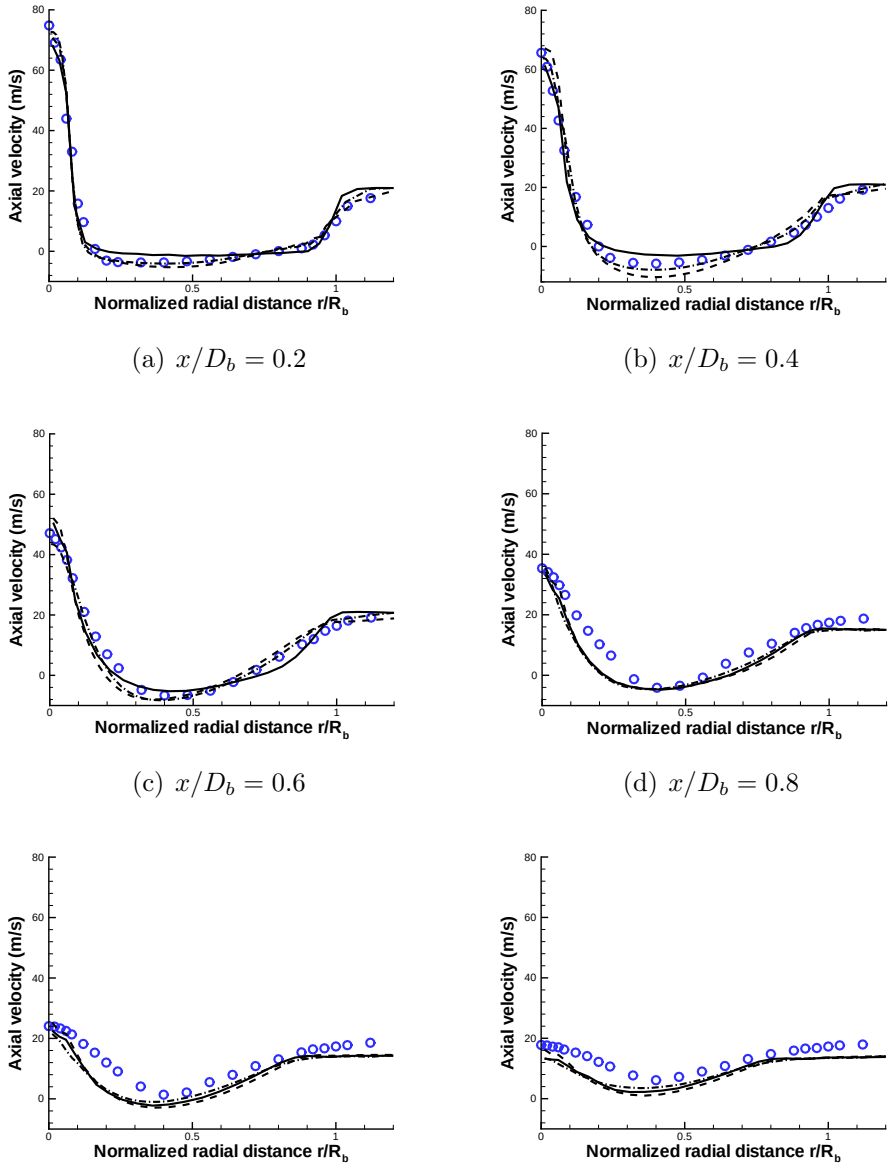

(a) $x/D_b = 0.2$ (b) $x/D_b = 0.4$

(c) $x/D_b = 0.6$ (d) $x/D_b = 0.8$

(e) $x/D_b = 1.0$ (f) $x/D_b = 1.2$

Figure 6.18: Comparison of axial mean velocities at $x/D_b = 0.2, 0.4, 0.6, 0.8, 1.0, 1.2$ in the NRBB case using LES. o: experimental data [16], solid: LES-A, dash: LES-B, dash-dot: LES-C.

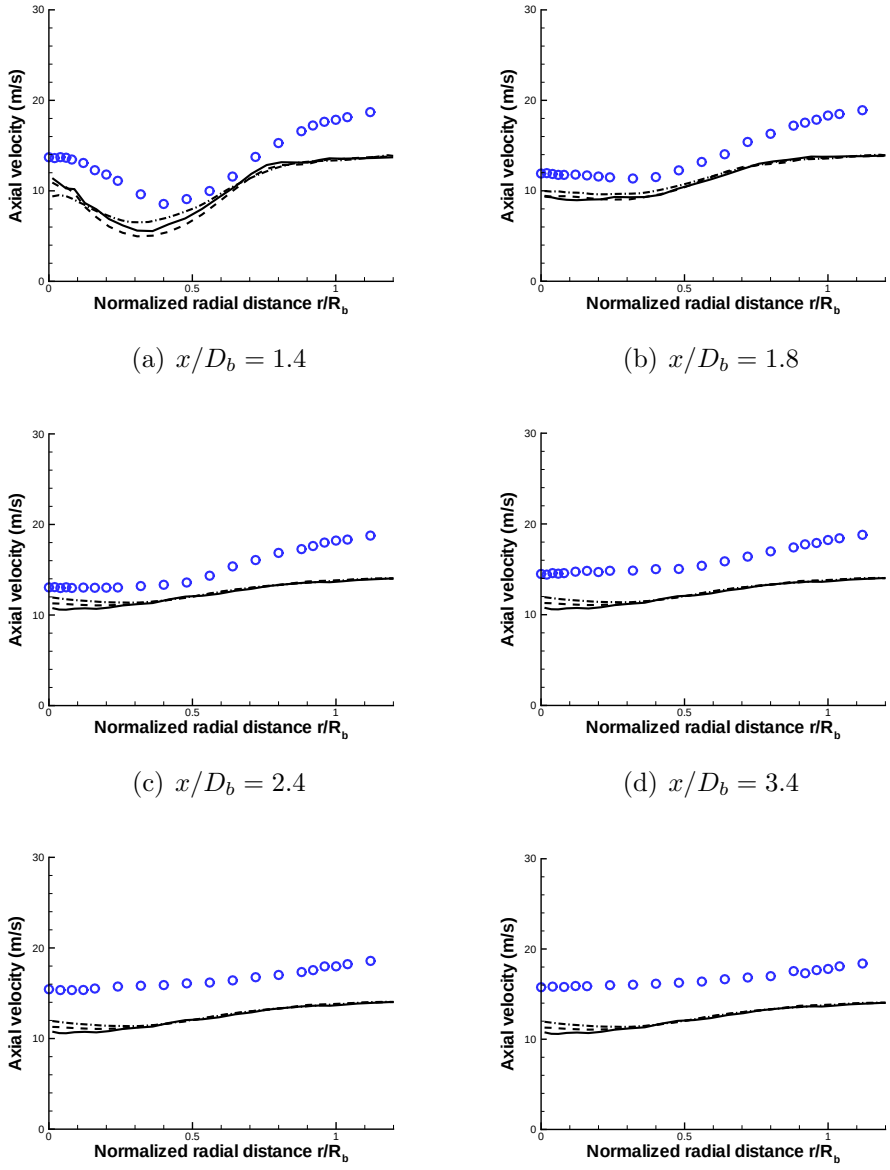

(a) $x/D_b = 1.4$

(b) $x/D_b = 1.8$

(c) $x/D_b = 2.4$

(d) $x/D_b = 3.4$

(e) $x/D_b = 4.4$

(f) $x/D_b = 5.2$

Figure 6.19: Comparison of axial mean velocities at $x/D_b = 1.4, 1.8, 2.4, 3.4, 4.4, 5.2$ in the NRBB case using LES. o: experimental data [16], solid: LES-A, dash: LES-B, dash-dot: LES-C.

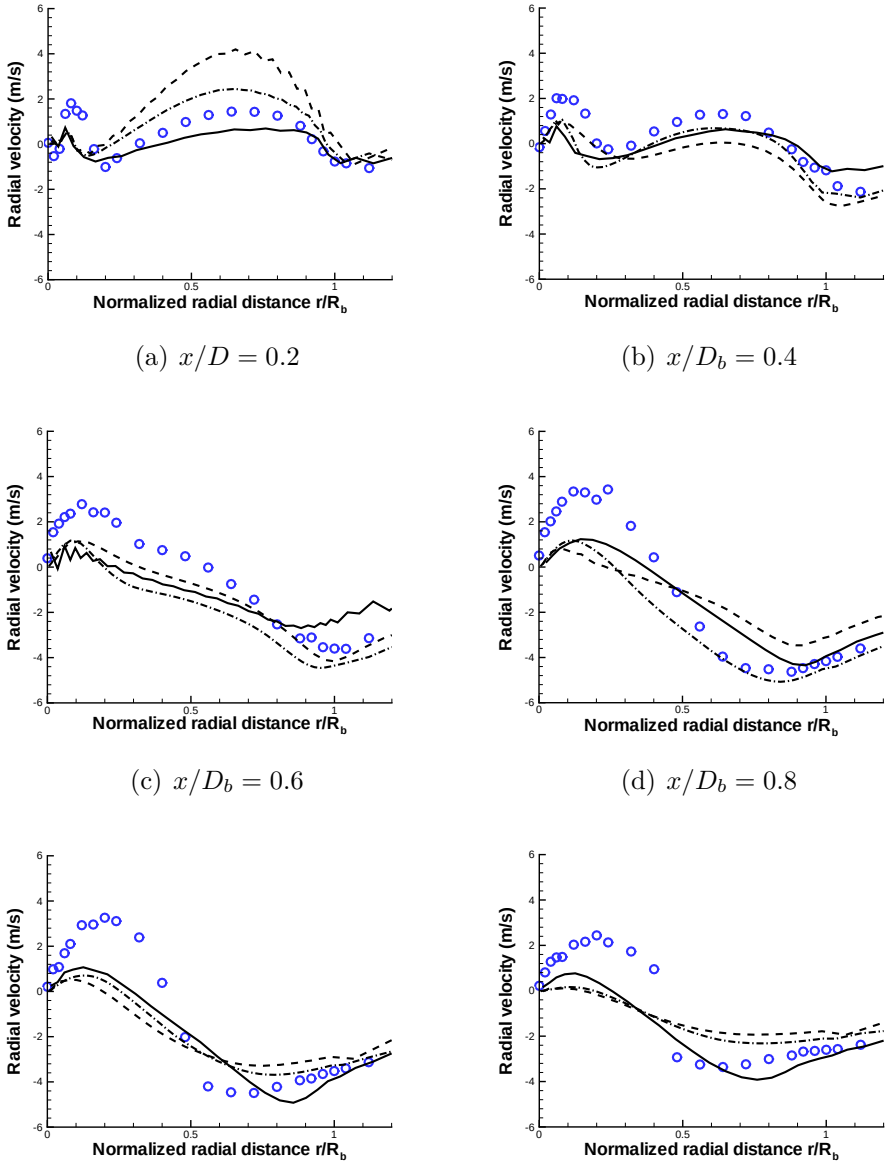

(a) $x/D = 0.2$ (b) $x/D_b = 0.4$

(c) $x/D_b = 0.6$ (d) $x/D_b = 0.8$

(e) $x/D_b = 1.0$ (f) $x/D_b = 1.2$

Figure 6.20: Comparison of radial mean velocities at $x/D_b = 0.2, 0.4, 0.6, 0.8, 1.0, 1.2$ in the NRBB case using LES. o: experimental data [16], solid: LES-A, dash: LES-B, dash-dot: LES-C.

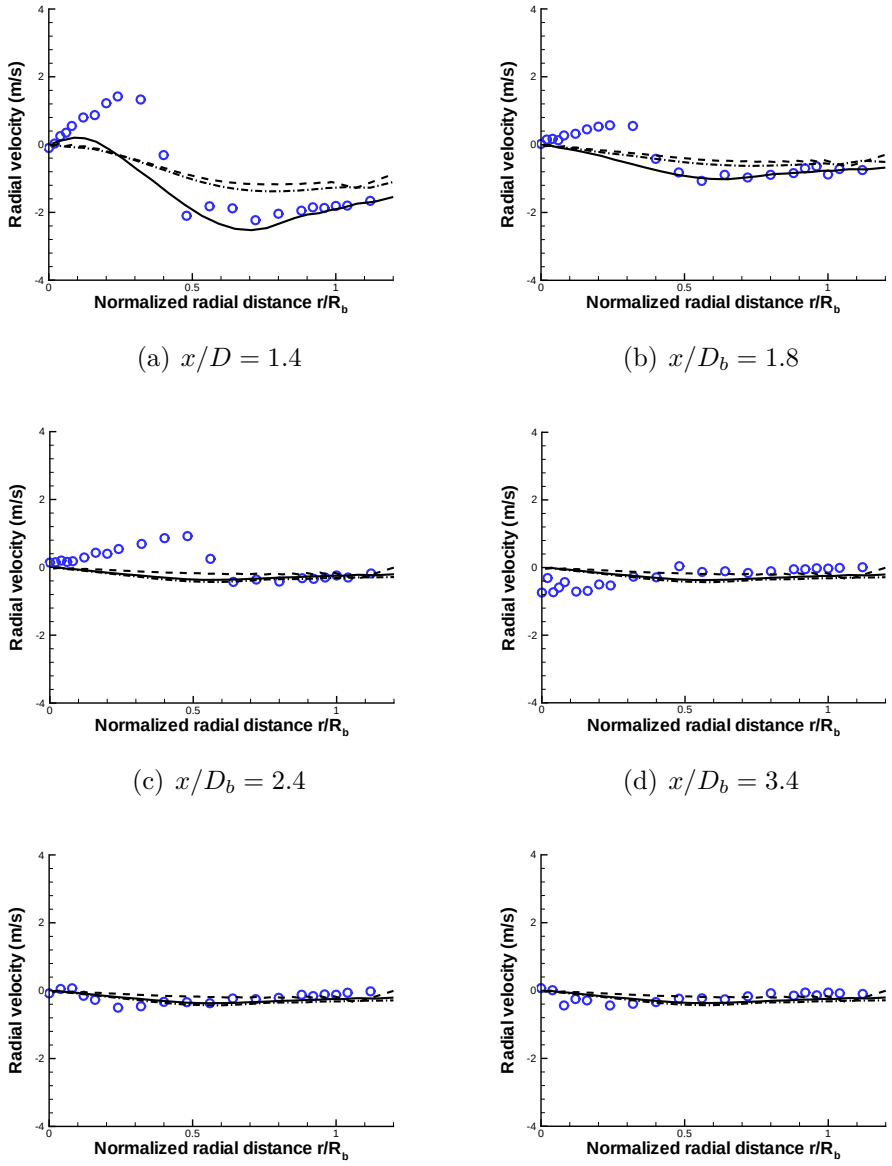

(a) $x/D = 1.4$ (b) $x/D_b = 1.8$

(c) $x/D_b = 2.4$ (d) $x/D_b = 3.4$

(e) $x/D_b = 4.4$ (f) $x/D_b = 5.2$

Figure 6.21: Comparison of radial mean velocities at $x/D_b = 1.4, 1.8, 2.4, 3.4, 4.4, 5.2$ in the NRBB case using LES. o: experimental data [16], solid: LES-A, dash: LES-B, dash-dot: LES-C.

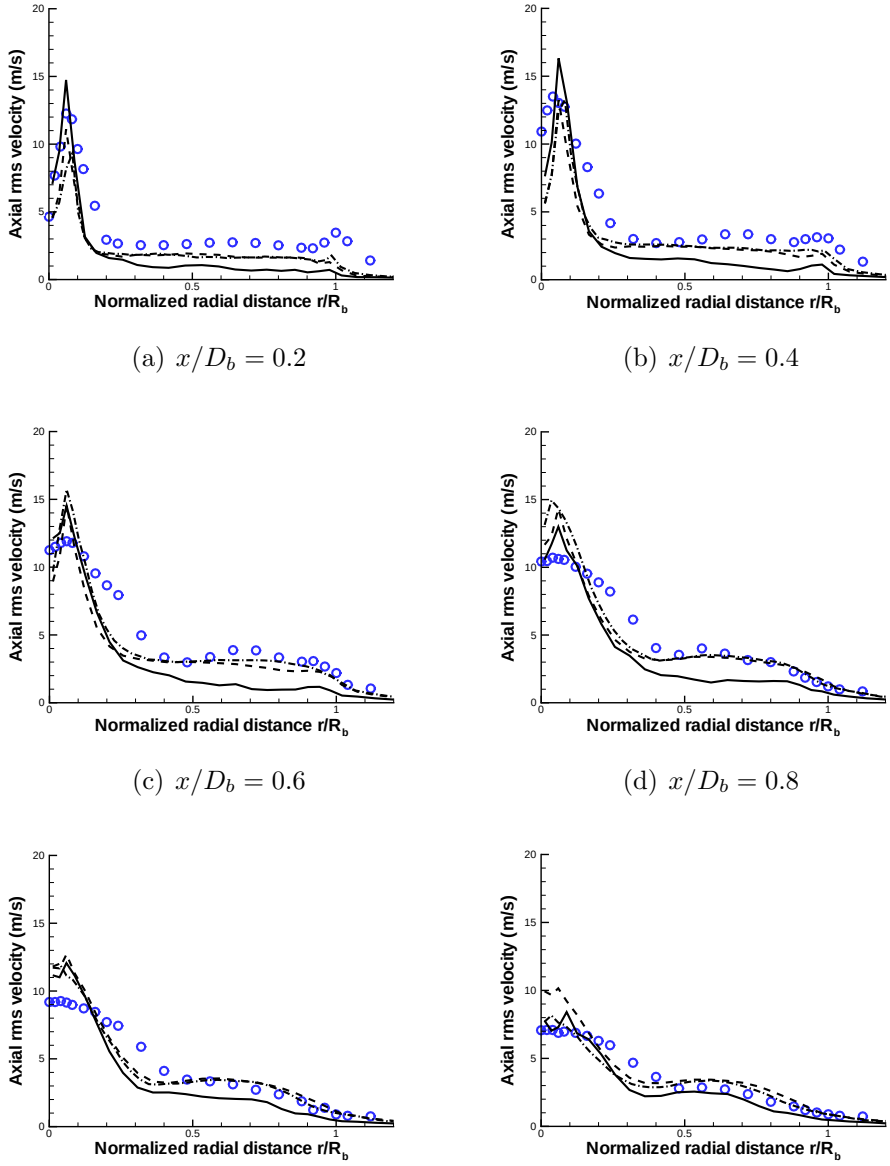

(a) $x/D_b = 0.2$ (b) $x/D_b = 0.4$

(c) $x/D_b = 0.6$ (d) $x/D_b = 0.8$

(e) $x/D_b = 1.0$ (f) $x/D_b = 1.2$

Figure 6.22: Comparison of axial rms velocities at $x/D_b = 0.2, 0.4, 0.6, 0.8, 1.0, 1.2$ in the NRBB case using LES. o: experimental data [16], solid: LES-A, dash: LES-B, dash-dot: LES-C.

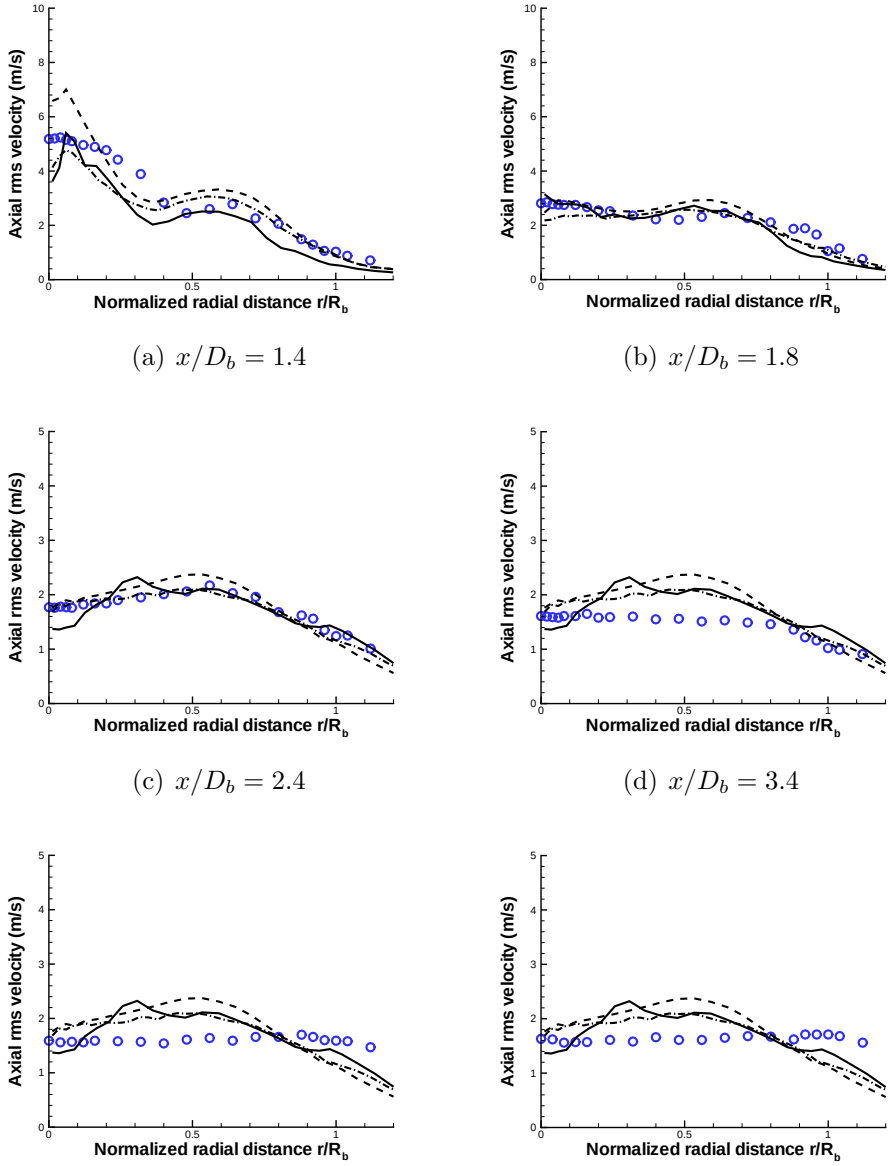

(a) $x/D_b = 1.4$ (b) $x/D_b = 1.8$

(c) $x/D_b = 2.4$ (d) $x/D_b = 3.4$

(e) $x/D_b = 4.4$ (f) $x/D_b = 5.2$

Figure 6.23: Comparison of axial rms velocities at $x/D_b = 1.4, 1.8, 2.4, 3.4, 4.4, 5.2$ in the NRBB case using LES. o: experimental data [16], solid: LES-A, dash: LES-B, dash-dot: LES-C.

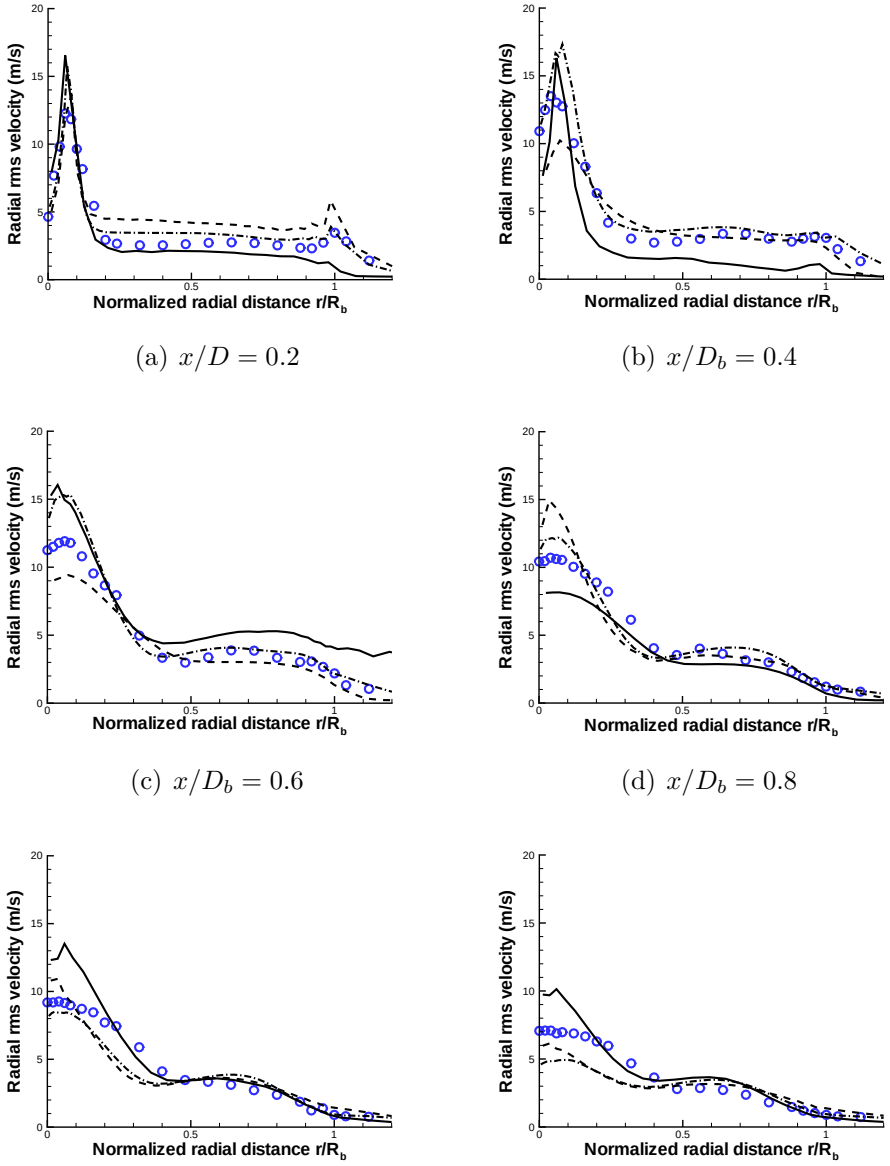

(a) $x/D = 0.2$ (b) $x/D_b = 0.4$

(c) $x/D_b = 0.6$ (d) $x/D_b = 0.8$

(e) $x/D_b = 1.0$ (f) $x/D_b = 1.2$

Figure 6.24: Comparison of radial rms velocities at $x/D_b = 0.2, 0.4, 0.6, 0.8, 1.0, 1.2$ in the NRBB case using LES. o: experimental data [16], solid: LES-A, dash: LES-B, dash-dot: LES-C.

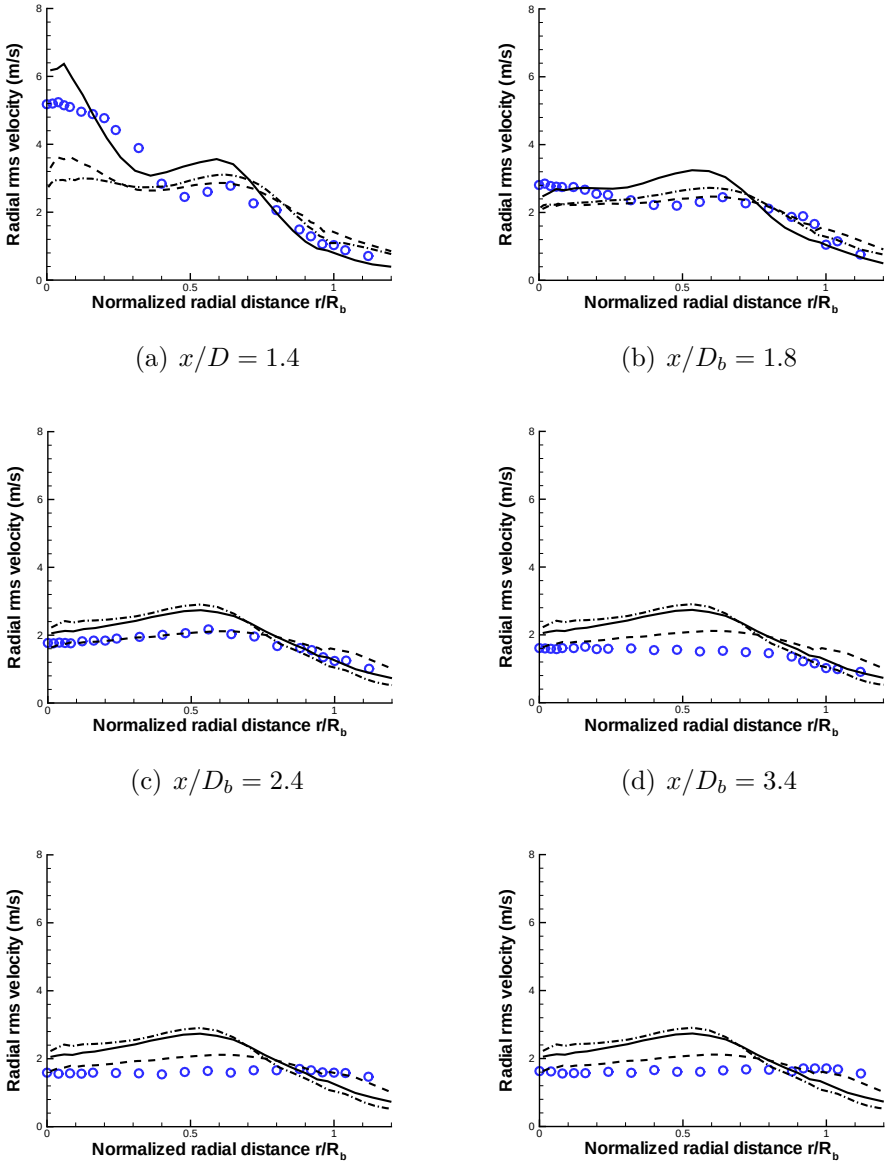

(a) $x/D = 1.4$ (b) $x/D_b = 1.8$

(c) $x/D_b = 2.4$ (d) $x/D_b = 3.4$

(e) $x/D_b = 4.4$ (f) $x/D_b = 5.2$

Figure 6.25: Comparison of radial rms velocities at $x/D_b = 1.4, 1.8, 2.4, 3.4, 4.4, 5.2$ in the NRBB case using LES. o: experimental data [16], solid: LES-A, dash: LES-B, dash-dot: LES-C.

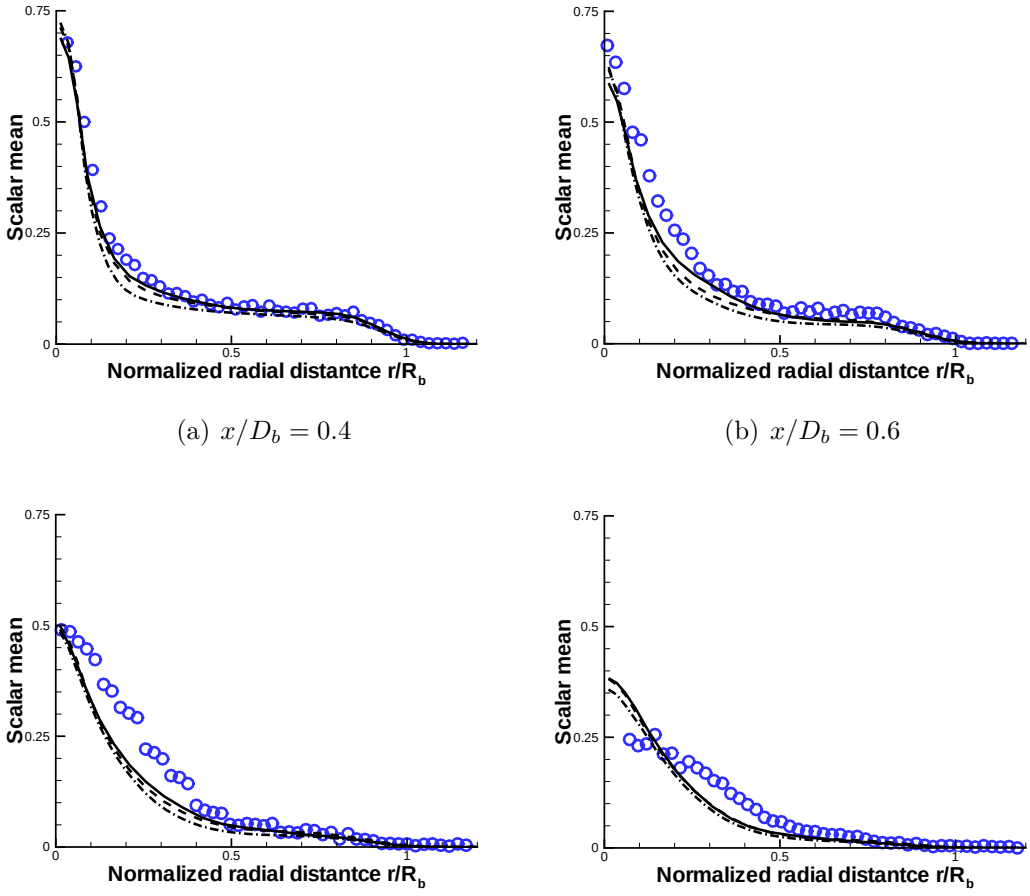

(a) $x/D_b = 0.4$

(b) $x/D_b = 0.6$

(c) $x/D_b = 0.8$

(d) $x/D_b = 1.0$

Figure 6.26: Scalar mean prediction at $x/D_b = 0.4, 0.6, 0.8, 1.0$ in the NRBB case using LES. o: experimental data [16], solid: LES-A, dash: LES-B, dash-dot: LES-C.

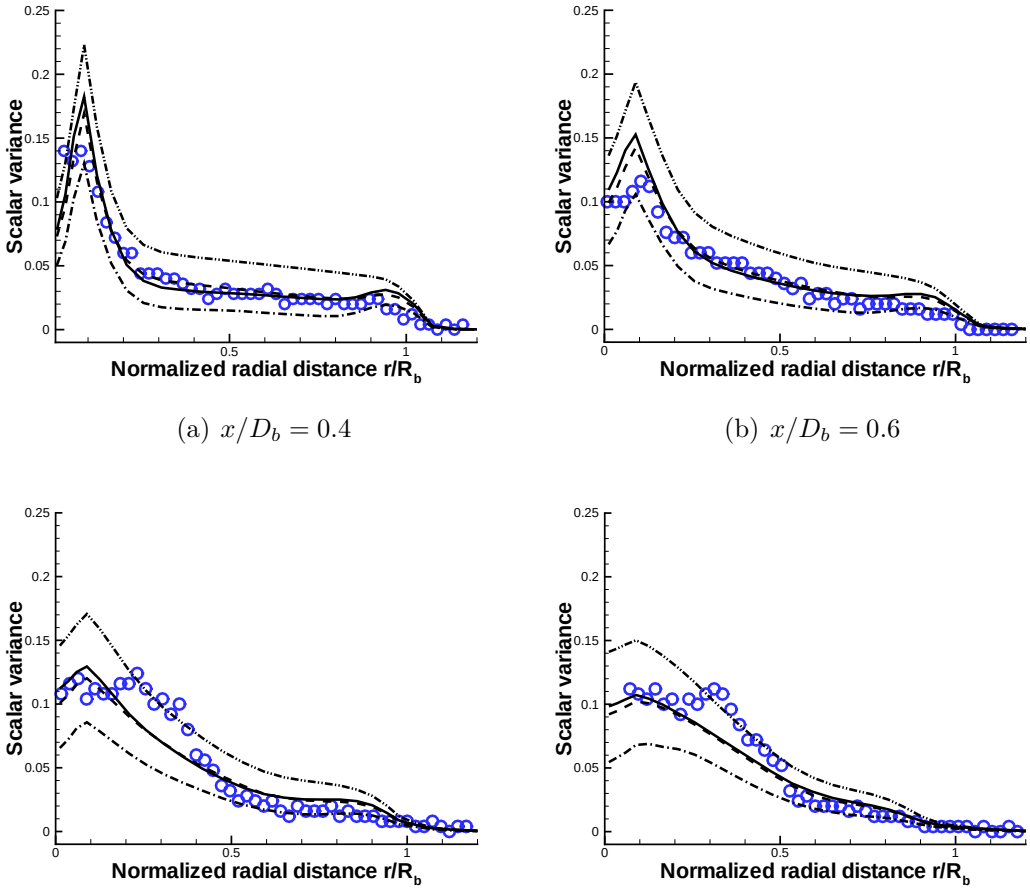

(a) $x/D_b = 0.4$ (b) $x/D_b = 0.6$

(c) $x/D_b = 0.8$ (d) $x/D_b = 1.0$

Figure 6.27: Scalar variance prediction at $x/D_b = 0.4, 0.6, 0.8, 1.0$ by solving the scalar dissipation rate transport equation with different model constants in LES (LES-A). o: experimental data [16], dash-dot-dot: Case 1, dash-dot: Case 2, dash: Case 3, solid: Case 4.

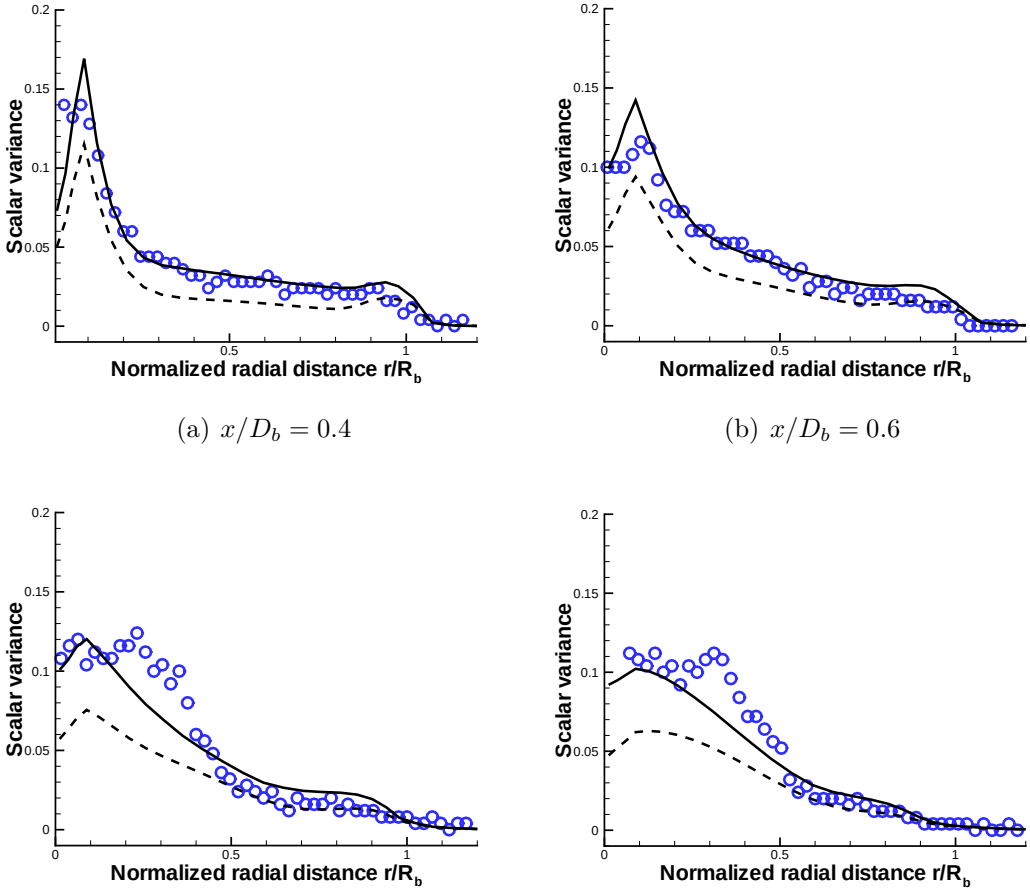

(a) $x/D_b = 0.4$

(b) $x/D_b = 0.6$

(c) $x/D_b = 0.8$

(d) $x/D_b = 1.0$

Figure 6.28: Scalar variance prediction at $x/D_b = 0.4, 0.6, 0.8, 1.0$ by the algebraic and the transport model in LES (LES-A). o: experimental data [16], dash: algebraic model, solid: transport equation model (Case 3).

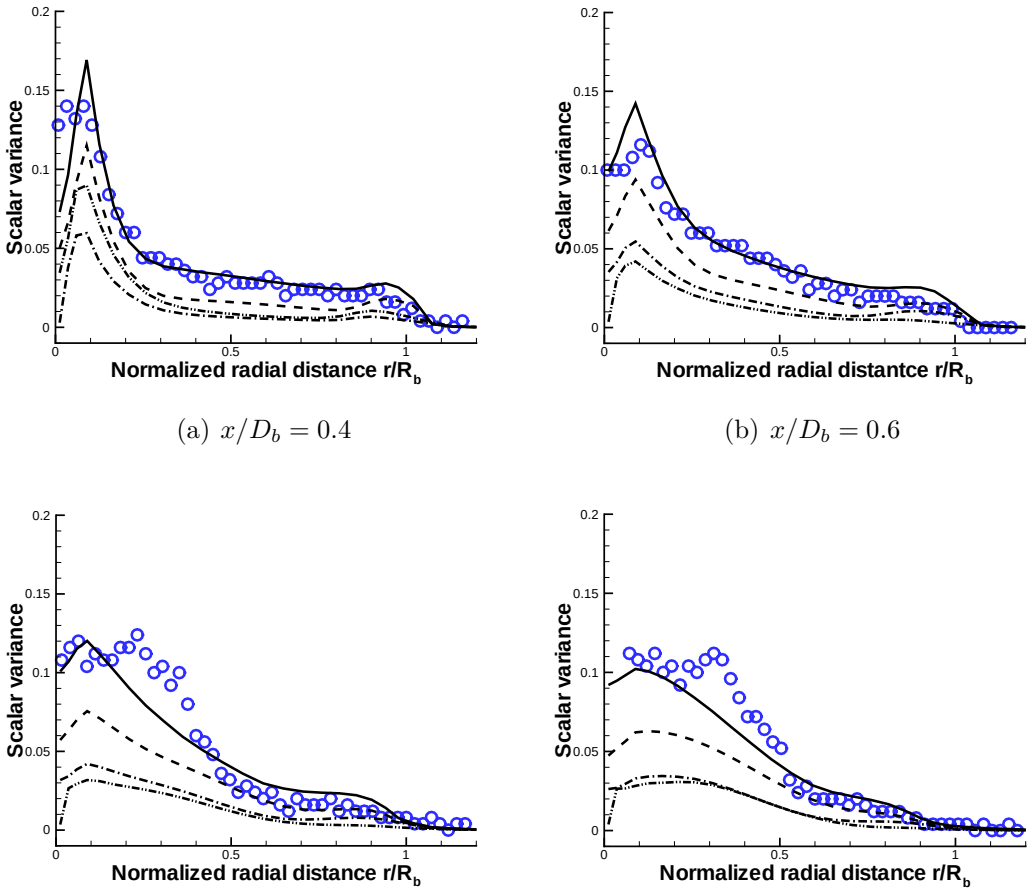

(a) $x/D_b = 0.4$

(b) $x/D_b = 0.6$

(c) $x/D_b = 0.8$

(d) $x/D_b = 1.0$

Figure 6.29: Scalar variance predicted at $x/D_b = 0.4, 0.6, 0.8, 1.0$ by different scalar variance models in LES (LES-A). o: experimental data [16], dash: scale similarity model, dash-dot-dot: gradient-based model, dash-dot: scalar variance transport equation with algebraic scalar dissipation rate model, solid: scalar variance transport equation with scalar dissipation rate transport model.

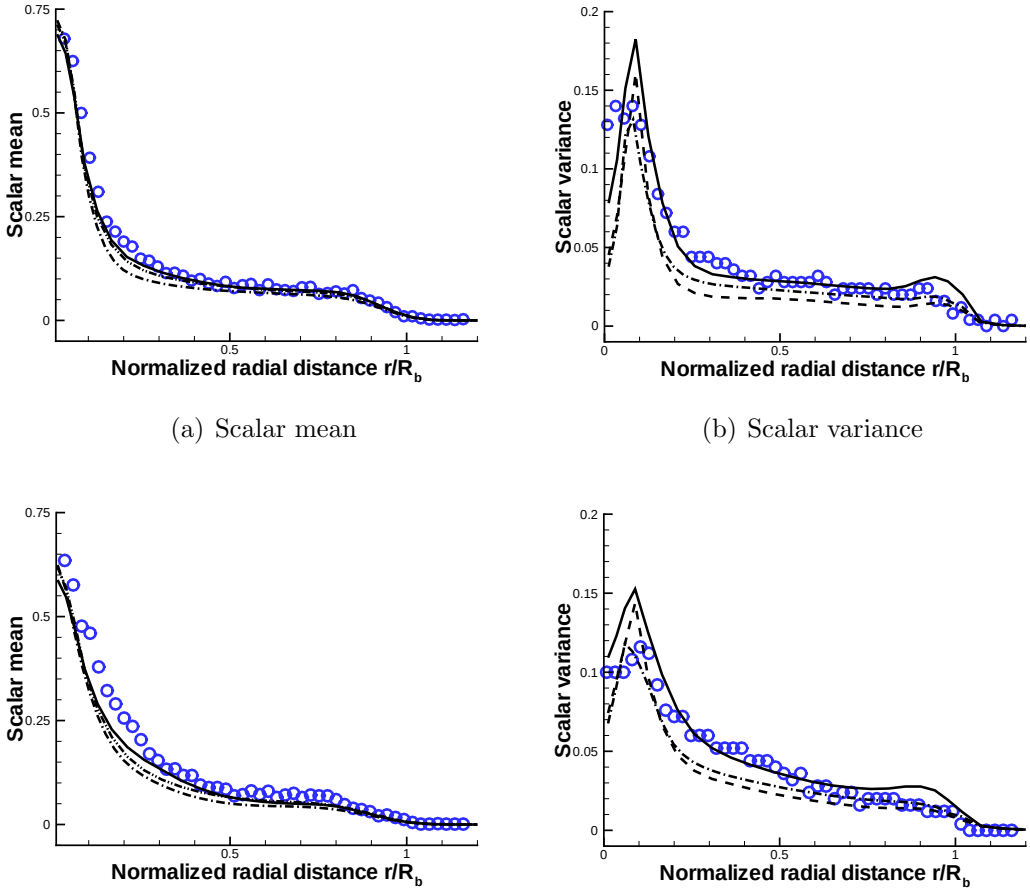

(a) Scalar mean

(b) Scalar variance

(c) Scalar mean

(d) Scalar variance

Figure 6.30: Profiles of scalar mean and variance predicted using LES with different grid resolutions at $x/D_b = 0.4$ ((a) and (b)) and at $x/D_b = 0.6$ ((c) and (d)). o: experimental data [16], solid: LES-A, dash: LES-B, dash-dot: LES-C.

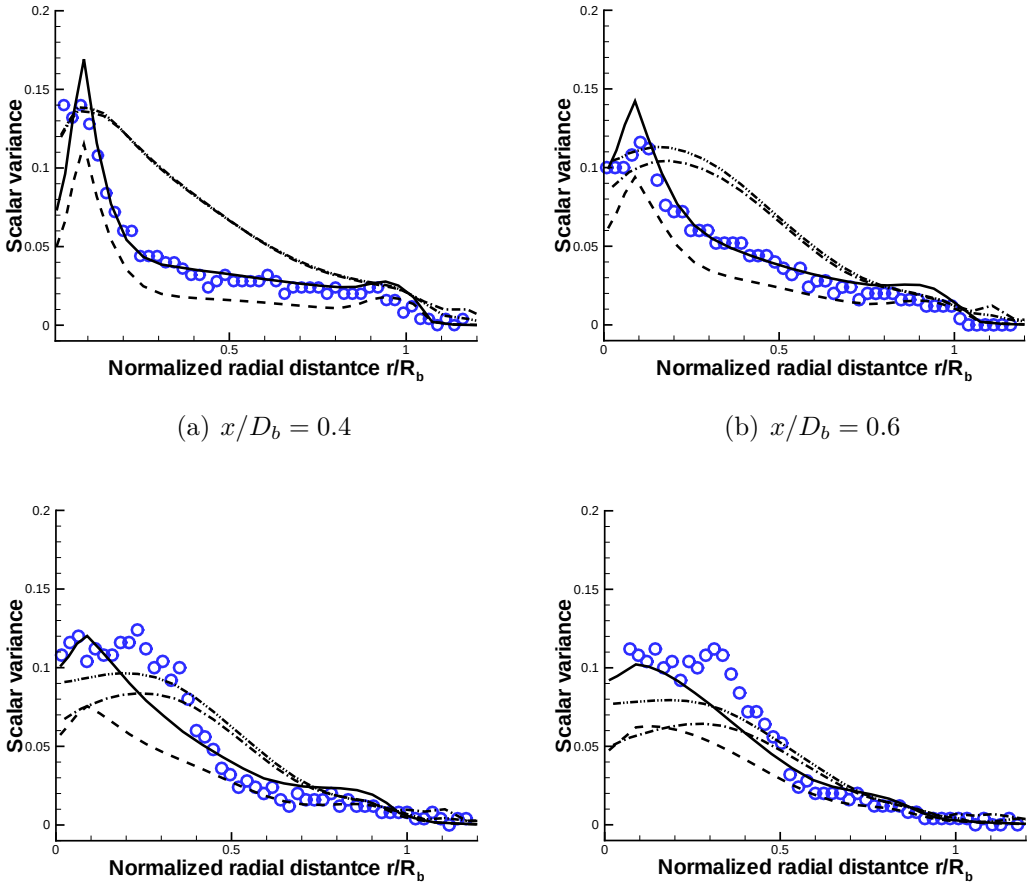

(a) $x/D_b = 0.4$

(b) $x/D_b = 0.6$

(c) $x/D_b = 0.8$

(d) $x/D_b = 1.0$

Figure 6.31: Scalar variance predictions using URANS and LES with same grid resolution for different scalar dissipation rate models. o: experimental data, dash-dot: algebraic model (URANS), dash-dot-dot: transport equation model (URANS), dash: algebraic model (LES), solid: transport equation model (LES).

6.4 Summary and conclusion

The scalar variance, which is required for the β-function PDF to describe the local mixing rate in the conserved scalar approach, has been examined using both URANS and LES in this study. A comparative study was done for both URANS and LES under the same grid resolution in order to see the potential benefit of converting RANS code to LES by changing the turbulence model. The results should be, in the author's opinion, interesting to those in the research community who mostly use RANS-based models.

As an alternative approach to algebraic models for the determination of scalar variance, its transport equation is introduced and the unclosed scalar dissipation rate term is parameterized by either an algebraic model or a transport equation model. The present study proposes a new algebraic LES model and a new transport equation LES model for the scalar dissipation rate, similar to the URANS approach. The major difference is that the SGS kinetic energy, $\widetilde{k}_{sgs}$, and its dissipation rate, $\widetilde{\varepsilon}_{sgs}$, are prescribed using algebraic expressions derived under the assumption of local equilibrium condition of the flow. So, two less transport equations are solved in LES compared to the URANS approach. Although the URANS approach involves solving two additional equations over LES, it takes about four times longer for LES to obtain converged results than URANS. For example, each time iteration in URANS converges within two iterations of the SIMPLE algorithm but requires eight iterations in LES.

Generally speaking, the scalar dissipation rate transport models for URANS and LES show better performance than their corresponding algebraic models. However, the shape of scalar variance distribution, which the algebraic URANS model fails to predict, still cannot be reproduced by using the transport equation URANS model for the scalar dissipation rate. In contrast, the LES transport model for the scalar dissipation rate gives the best conformance to experimental data, both in terms of the magnitude and shape of scalar variance distribution. As mentioned earlier, the turbulent mixing process depends strongly on the turbulence and mixing models. This is somewhat

expected because firstly LES is, in principle, a more accurate turbulence model than URANS. Secondly, it is physically more correct to represent the turbulent mixing process using the transport equation model instead of the algebraic model, since the local equilibrium assumption of the scalar is questionable for complex recirculating flows.

Chapter 7

Reacting Bluff-Body flow

The newly proposed approach for the scalar variance and scalar dissipation rate is now extended to the reacting case. The geometric configuration is the same as for the non-reacting case described in the previous section. The numerical experiments have been conducted by implementing different scalar dissipation rate models. In the conserved scalar formalism, the chemical equilibrium model shown in Figure 2.3, which is introduced in Section 2.2.3, is adopted to deal with the local chemical reactions. A $\delta-$function PDF calculation is also performed for comparison purposes. Similar to the previous chapter, URANS calculations are first conducted and LES calculations will be left for future work.

7.1 Sydney bluff-body recirculating reacting flow

A turbulent non-premixed bluff-body stabilized $CH_4 : H_2$ flame, which is often called the Sydney bluff-body flame, is simulated. This flame has been a popular choice as a validation case since it shows high level of complexity in flow but yet it reveals little local extinction. Additionally, as a combustor is closed system, the interaction

of the flame with the walls and the effect of the inflow geometry should be modelled appropriately.

The Sydney bluff-body burner under consideration has the same geometry as the non-reacting flow case shown in Figure 6.1(a), but has different flow conditions and chemical reactions. Similar to the non-reacting case, this bluff-body flame involves the complex flow physics encountered in the recirculation zone and the neck zone. The recirculation zone is formed immediately behind the bluff-body wall as shown in Figure 7.1(a). Two vortices in the recirculation zone stabilizes the flames, i.e., hot products ciculate back to the nozzle exit and provide a continuous ignition source for the flame. The jet penetrates a hot lower density medium, which results in a shift of the stagnation point further downstream of the bluff body. According to Raman and Pitch [71], this flame is highly transient and three-dimensional and cannot be realistically captured by RANS-based models. This instability is also noticed in URANS simulations and is shown in the snapshot of the flame in Figure 7.1(b). The recent work of Kuan and Lindstedt [40] supports this by addressing the transient effects of the bluff-body flame. At the downstream region where the recirculation zone ends, there exists a neck zone that has strong interactions between turbulent mixing and chemical reactions. Further downstream, a jet-like flame zone is created.

The fuel consists of a 1 : 1 methane:hydrogen volume fraction with an approximate stoichiometric ratio of 0.05. Due to wind tunnel limitations, experimental data for the flow field were obtained at slightly different inlet velocities than the scalar field [16]. Therefore, two different simulations are carried out corresponding to their respective flow field and scalar measurements. The first simulation (HM1E) used a fuel jet velocity of $U_{jet} = 108$ m/s and a coflow velocity of $U_{coflow} = 35$ m/s. Results from this simulation are compared against velocity statistics from the experiment. The second simulation (HM1) used a slightly higher jet velocity of $U_{jet} = 118$ m/s and a coflow velocity of $U_{coflow} = 40$ m/s. These results are compared with the scalar field profiles of the experiment. While the velocity measurement was performed as it was done in NRBB, scalar field measurements were made using the Raman/Rayleigh/LIF technique to give instantaneous and simultaneous temperature

and the concentration of many species at a single point in the flame. The species measured are: $N_2, O_2, CH_4, CO, CO_2, H_2, H_2O, OH$ and NO. Experimental data HM1 and HM1E are both at 50% of the blow-off limit and are thus expected to show similar characteristics. This is supported by Kuan and Lindstedt [40], who found that the flow fields only differ marginally. Experiment details can be found in [16].

7.2 Simulation details

The same discretization used for the non-reacting case (NRBB) is used for this reacting simulation (RBB). While the lateral computational domain size remains the same, the streamwise computational domain is extended to $12R_b$ following recent work [34, 71] so that the inlet plane is placed at $x = -100$ mm and the outlet is at $x = 200$ mm. Grid resolution is initially chosen to be same as the NRBB case but the results of flow turbulence quantities show poor prediction in particular near the interface between the two recirculating vortices. Based on trial and error and following Lien [45], all computations are performed on a non-uniform grid of $(n_x, n_r, n_\theta) = (150, 90, 34)$. Numerical grids are densely refined in the proximity of the recirculation zone and neck zone in the axial direction, and are properly distributed in the jet region and the shear layer around the outer edge of the bluff body.

Since this case is an extension of the NRBB case, most numerical aspects remain the same. Four transport equations (energy, scalar mean, scalar variance and scalar dissipation rate) are solved for the scalar field of the reacting case, and the appropriate boundary conditions for each equation are defined. The scalar mean (mixture fraction) is set to $Z = 1$ at the jet flow and $Z = 0$ at the coflow, and the scalar variance and its dissipation rate are set to zero at all inlet sides. The enthalpy value based on the mixture in the co-flow and the nozzle jet is supplied at the appropriate boundary. The parallelized STREAM code is also employed to simulate URANS and the standard $k - \varepsilon$ model is used to update the turbulent viscosity.

The focus of the present chapter is to compare the model performance of the scalar

dissipation rate models in the reacting flow and to examine how the scalar dissipation rate models contributes in the reacting case. It is naturally expected that the better accuracy of this modeling leads to improved prediction of the mean thermochemical variables through accurate $\beta-$function PDF integration. To this end, the algebraic and transport equation models with four different model constants, which are introduced and tested in NRBB, are simulated in conjunction with the chemical equilibrium model. A simulation with a δ-function PDF, which relies only on the scalar mean, is also conducted and the results are compared with other $\beta-$function PDF models. However, the results of the $\delta-$function PDF show the worst prediction among the test cases in the most of considered variables. Therefore, the $\delta-$function PDF results are presented but not discussed from now on unless necessary.

7.3 Results

7.3.1 Flow Field

A complex flow pattern forms downstream of the face of the bluff-body with two recirculation zones as shown in Figure 7.1(a). At sufficiently high fuel jet velocity, the flow penetrates the recirculation zone and forms a jet-like flame further downstream. Based on the flow pattern and the two mixture boundaries, distinctly different reaction zones can be identified. It can clearly be seen that the counter rotating vortices are present in the recirculation region. The main reaction zone, where the preheated and partially reacted fuel and the coflowing oxidizer mix, is located at the edge of the outer vortex. Two vortices transport the fuel and the air into the recirculation zone to stabilize the flame. A narrow reaction zone with the near-stoichiometric or slightly leaner mixture is created in the outer shear layer between the coflow and the outer vortex. The flame field in the recirculation zone is characterized by a rich mixture condition and the corresponding temperature and reaction rates are much lower than those at the stoichiometric condition.

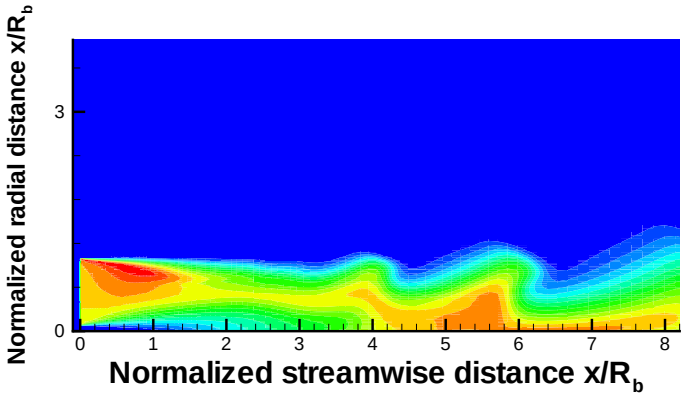

Figure 7.1: Instantaneous temperature distribution in URANS simulation.

As discussed in the recent literature by Raman and Pitsch [71], the recirculation zone exhibits large-scale recirculation with the volume of fluid entrapped in the vortices. The large density gradient in the outer shear layer also generates an amount of vortex shedding. The non-stationary turbulent flow structure is highly three dimensional, with large variations in local compositions along the azimuthal direction. This signifies the complexity of this flow and a time-resolving unsteady flow solver is obviously necessary to simulate the non-stationary turbulent complex flame field realistically.

The predicted axial and radial profiles of the mean velocities for the HM1E flame shown in Figures 7.2 to 7.5 are compared to measurements taken at different axial locations ($x/D_b \in \{0.2, 0.4, 0.6, 0.8, 1.0, 1.2, 1.4, 1.8, 2.4, 3.4\}$) by six different simulations in conjunction with the chemical equilibrium model. Despite of the shortcomings of RANS-based models, the mean velocities and the recirculating lengths are predicted well by all simulations. Similar to NRBB results in Section 6.3, good agreement between the calculated and experimental axial mean velocity profiles is achieved up to $x/D_b = 1.0$. At further downstream stations, however, the mean centerline velocities

are under-predicted. This seems to be due to the over-estimation of the spreading rate of the fuel jet and this under-estimation of mean profiles, which also occurs in the NRBB simulations, is often noticed in RANS-based models. Radial velocity profiles are much improved compared to the NRBB case and this seems to be due to the grid resolution of the wall-normal direction. After the recirculation zone, the radial mean velocity profiles in Figure 7.5 suddenly show very poor prediction, most likely due to vortex shedding downstream. As many others have reported [34, 71], and as seen in Figure 7.1(b), strong vortex shedding occurs at the edge of the outer bluff-body and this unsteady feature shakes the flame downstream. Predictions are quite accurate in the recirculation region, while the peaks in the velocity profiles are under-predicted in downstream locations. It has been noted that there are significant experimental discrepancies at downstream locations [56]. Taking this into account, the current predictions are able to capture the flame structure and the essential characteristics of the flow.

Figures 7.6 to 7.9 compare rms velocity profiles. Similar to the mean velocity profiles, the axial rms velocity profiles show good agreement with experimental data up to $x/D_b = 1.0$ but the centerline rms velocities are under-predicted downstream. This could also be explained by spreading rate over-estimation. Radial rms velocities are slightly over-predicted throughout the entire domain. It should be noted that the discrepancy between model predictions and experimental data in this reacting case is smaller than in the non-reacting case. This may be attributed to a reduction in the radial diffusion effect, causing a decrease in the spreading rate of the fuel jet. As a result, the deficiency of the under-estimation of the centerline velocity in the NRBB case is improved in the RBB case. The reason for less diffusion occurring in the RBB case is likely due to a decrease in the turbulent viscosity. In a reacting flow, the density of the mixture decreases when the temperature increases.

It is seen that both the axial and radial rms velocities show a small peak near the outer edge of the bluff-body, corresponding to the interaction of the coflow with the recirculating fluid. Further downstream, this secondary peak in the rms axial velocity profiles moves toward the centerline, indicating that the width of the recirculation

zone decreases with axial distance. All simulations give very similar results until the recirculation zone ends, subsequently, they show slightly different prediction of velocity profiles downstream. It should be noted that the simulation with the $\delta-$function PDF gives quite poorer prediction than all other $\beta-$function PDF simulations. Overall, the simulations yield reasonable velocity profiles for the more challenging reactive case, although excessive rms velocity fluctuations are predicted in both the inner and outer shear layers.

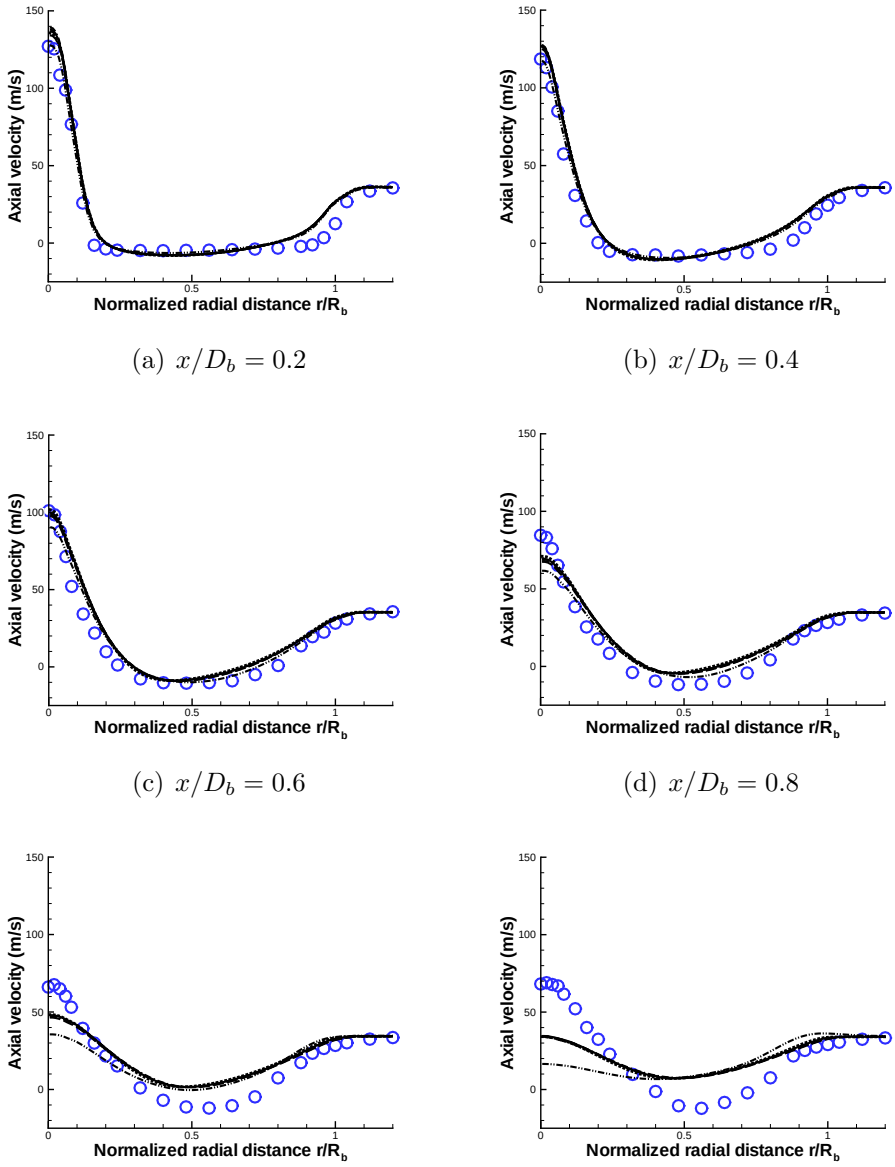

(a) $x/D_b = 0.2$ (b) $x/D_b = 0.4$

(c) $x/D_b = 0.6$ (d) $x/D_b = 0.8$

(e) $x/D_b = 1.0$ (f) $x/D_b = 1.2$

Figure 7.2: Comparison of axial mean velocities at at $x/D_b = 0.2, 0.4, 0.6, 0.8, 1.0, 1.2$ in the RBB case using URANS. o: experimental data [16], dash-dot-dot: δ-PDF, long-dash: algebraic model, dotted: Case 1, dash-dot: Case 2, dashed: Case 3, Solid: Case 4.

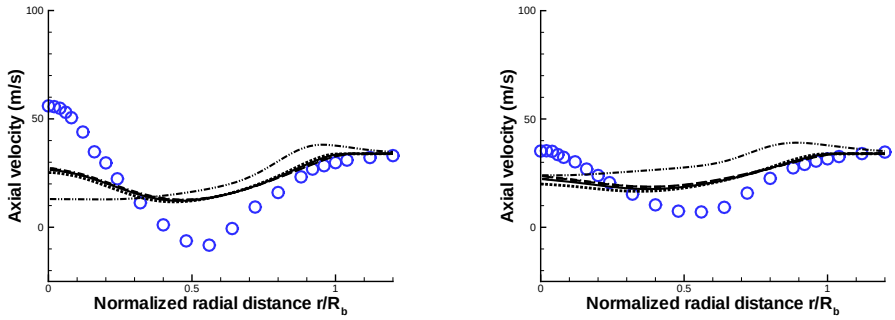

(a) $x/D_b = 1.4$

(b) $x/D_b = 1.8$

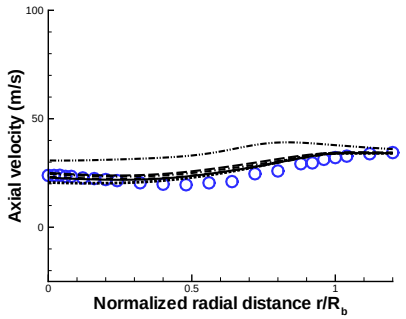

(c) $x/D_b = 2.4$

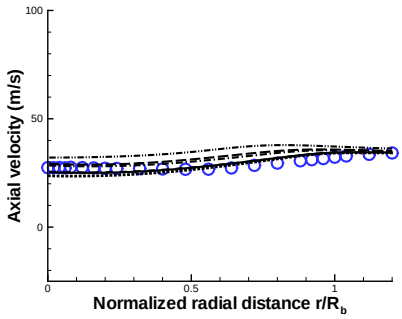

(d) $x/D_b = 3.4$

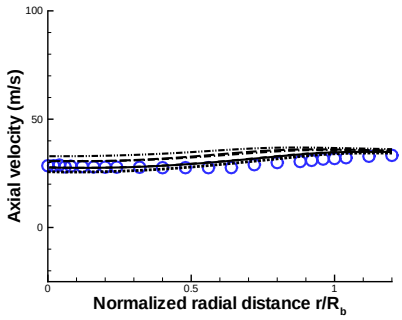

(e) $x/D_b = 4.4$

Figure 7.3: Comparison of axial mean velocities at at $x/D_b = 1.4, 1.8, 2.4, 3.4, 4.4$ in the RBB case using URANS. o: experimental data [16], dash-dot-dot: δ-PDF, long-dash: algebraic model, dotted: Case 1, dash-dot: Case 2, dashed: Case 3, Solid: Case 4.

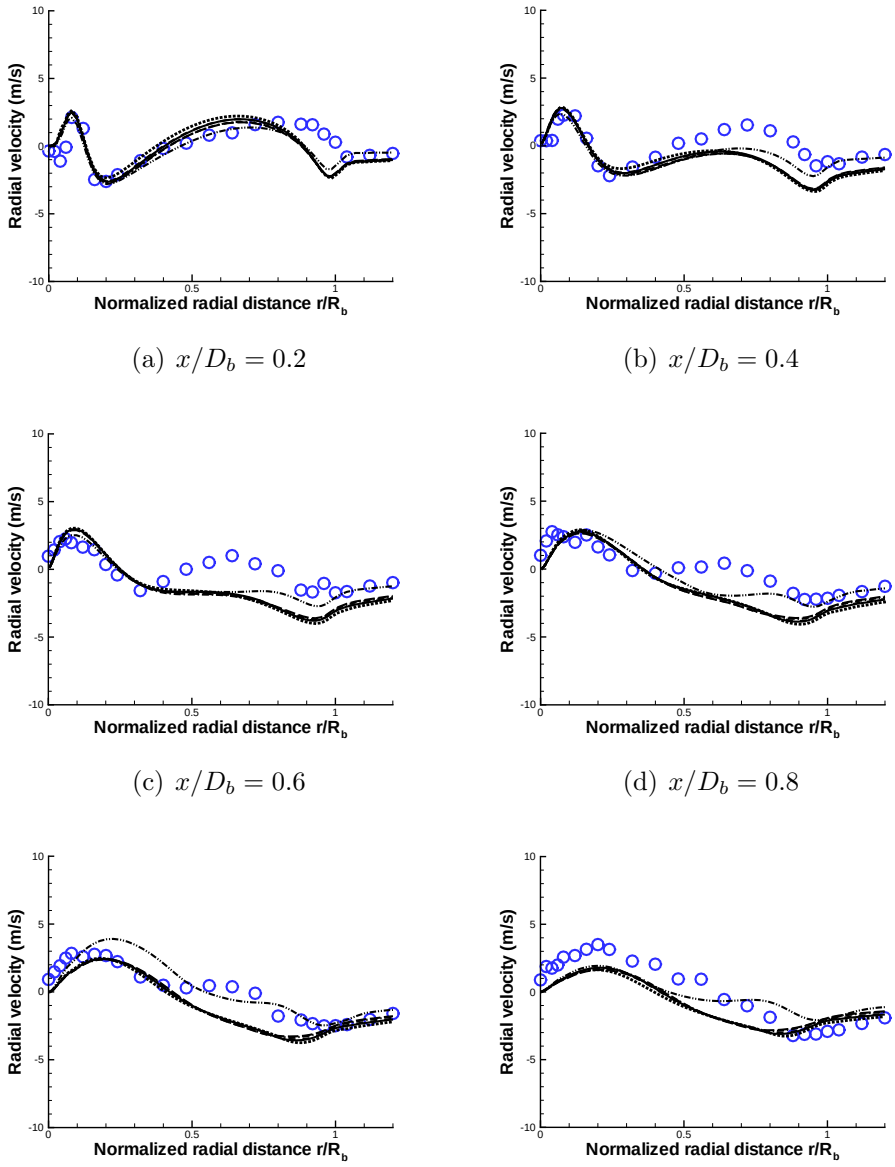

(a) $x/D_b = 0.2$ (b) $x/D_b = 0.4$

(c) $x/D_b = 0.6$ (d) $x/D_b = 0.8$

(e) $x/D_b = 1.0$ (f) $x/D_b = 1.2$

Figure 7.4: Comparison of radial mean velocities at at $x/D_b = 0.2, 0.4, 0.6, 0.8, 1.0, 1.2$ in the RBB case using URANS. o: experimental data [16], dash-dot-dot: δ-PDF, long-dash: algebraic model, dotted: Case 1, dash-dot: Case 2, dashed: Case 3, Solid: Case 4.

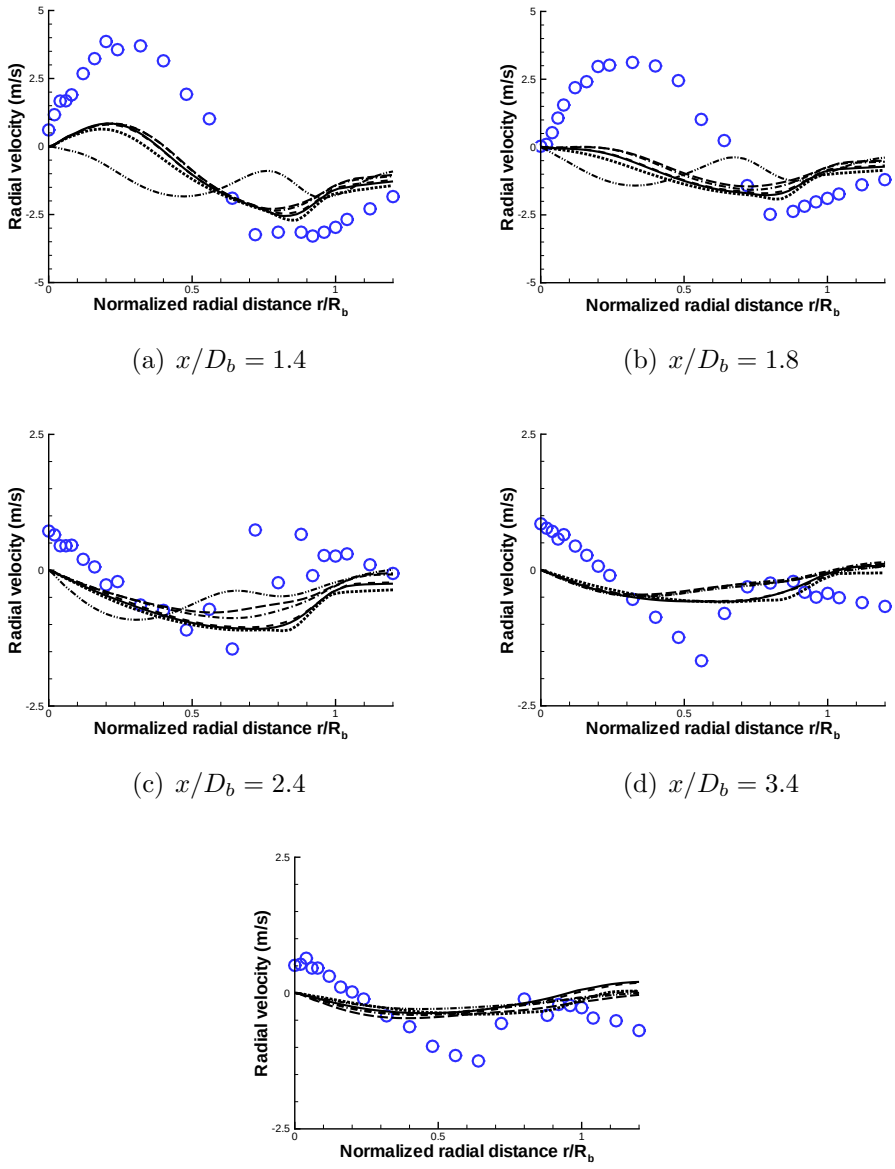

(a) $x/D_b = 1.4$

(b) $x/D_b = 1.8$

(c) $x/D_b = 2.4$

(d) $x/D_b = 3.4$

(e) $x/D_b = 4.4$

Figure 7.5: Comparison of radial mean velocities at at $x/D_b = 1.4, 1.8, 2.4, 3.4, 4.4$ in the RBB case using URANS. o: experimental data [16], dash-dot-dot: δ-PDF, long-dash: algebraic model, dotted: Case 1, dash-dot: Case 2, dashed: Case 3, Solid: Case 4.

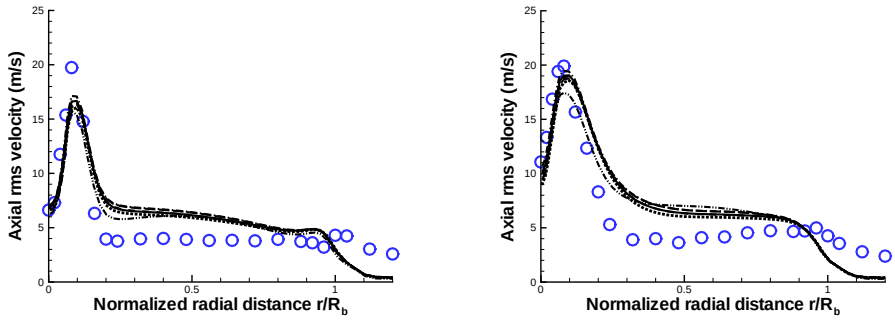

(a) $x/D_b = 0.2$

(b) $x/D_b = 0.4$

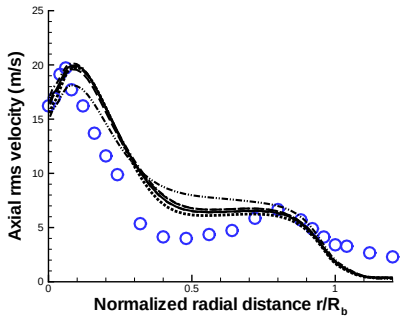

(c) $x/D_b = 0.6$

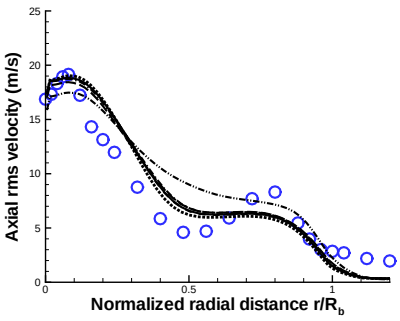

(d) $x/D_b = 0.8$

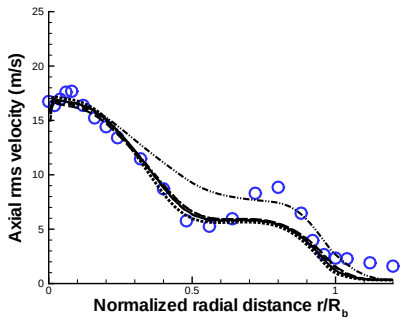

(e) $x/D_b = 1.0$

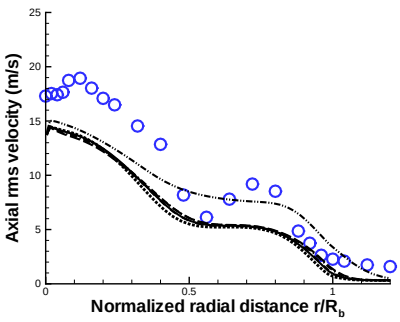

(f) $x/D_b = 1.2$

Figure 7.6: Comparison of axial rms velocities at at $x/D_b = 0.2, 0.4, 0.6, 0.8, 1.0, 1.2$ in the RBB case using URANS. o: experimental data [16], dash-dot-dot: δ-PDF, long-dash: algebraic model, dotted: Case 1, dash-dot: Case 2, dashed: Case 3, Solid: Case 4.

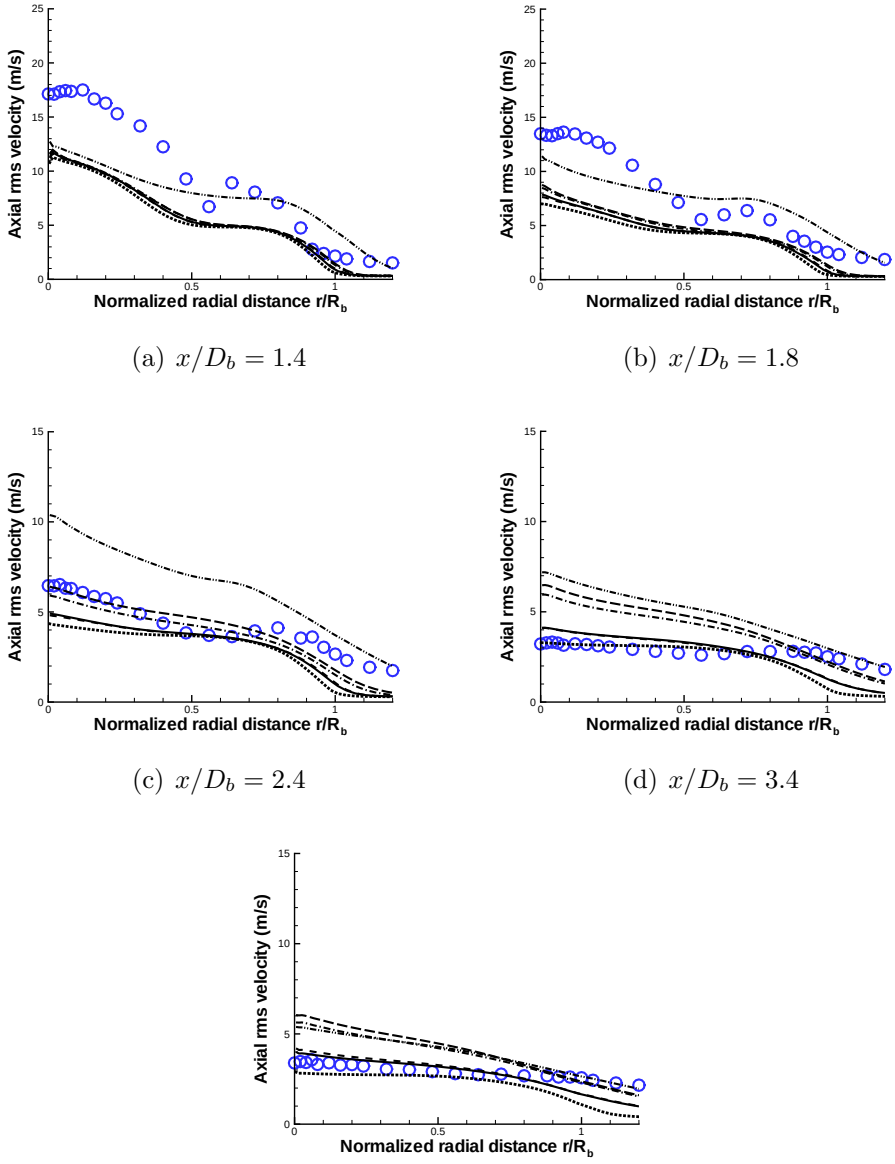

(a) $x/D_b = 1.4$

(b) $x/D_b = 1.8$

(c) $x/D_b = 2.4$

(d) $x/D_b = 3.4$

(e) $x/D_b = 4.4$

Figure 7.7: Comparison of axial rms velocities at at $x/D_b = 1.4, 1.8, 2.4, 3.4, 4.4$ in the RBB case using URANS. o: experimental data [16], dash-dot-dot: δ-PDF, long-dash: algebraic model, dotted: Case 1, dash-dot: Case 2, dashed: Case 3, Solid: Case 4.

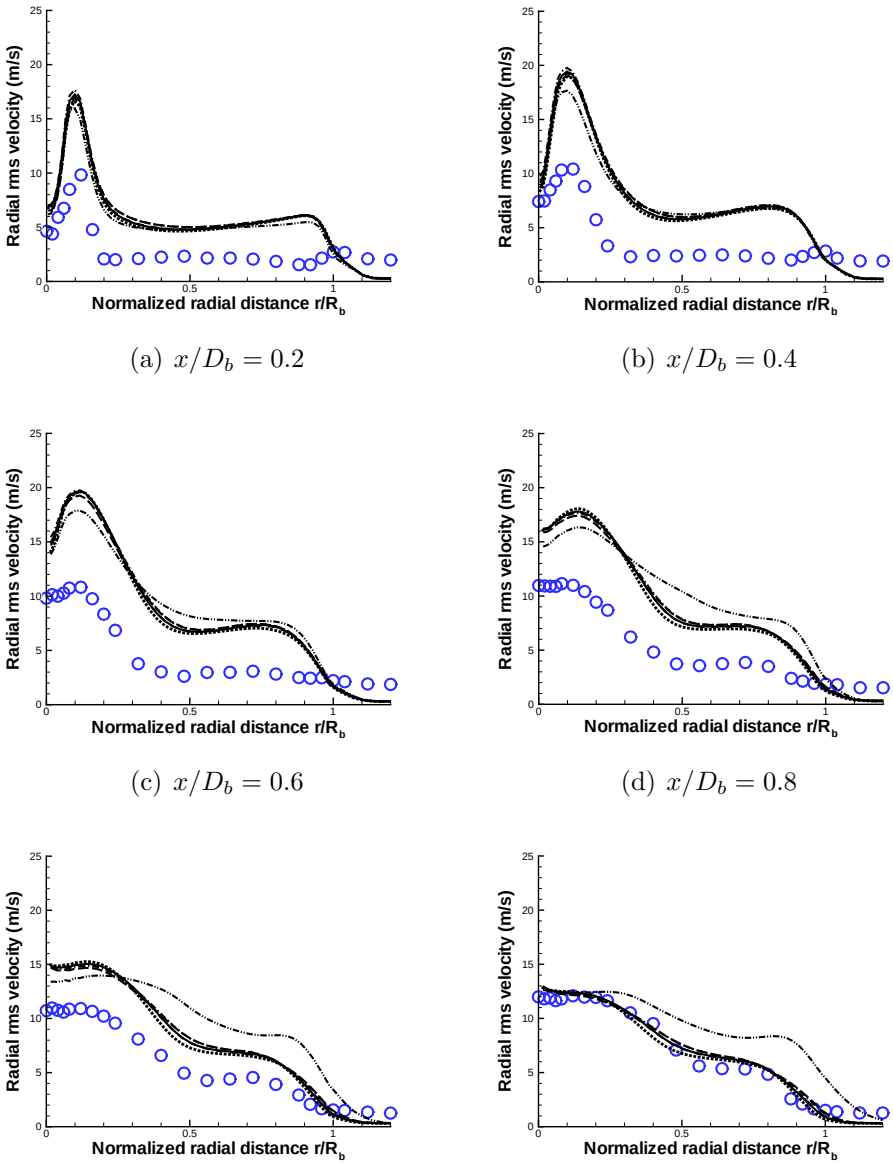

(a) $x/D_b = 0.2$ (b) $x/D_b = 0.4$

(c) $x/D_b = 0.6$ (d) $x/D_b = 0.8$

(e) $x/D_b = 1.0$ (f) $x/D_b = 1.2$

Figure 7.8: Comparison of radial rms velocities at at $x/D_b = 0.2, 0.4, 0.6, 0.8, 1.0, 1.2$ in the RBB case using URANS. o: experimental data [16], dash-dot-dot: δ-PDF, long-dash: algebraic model, dotted: Case 1, dash-dot: Case 2, dashed: Case 3, Solid: Case 4.

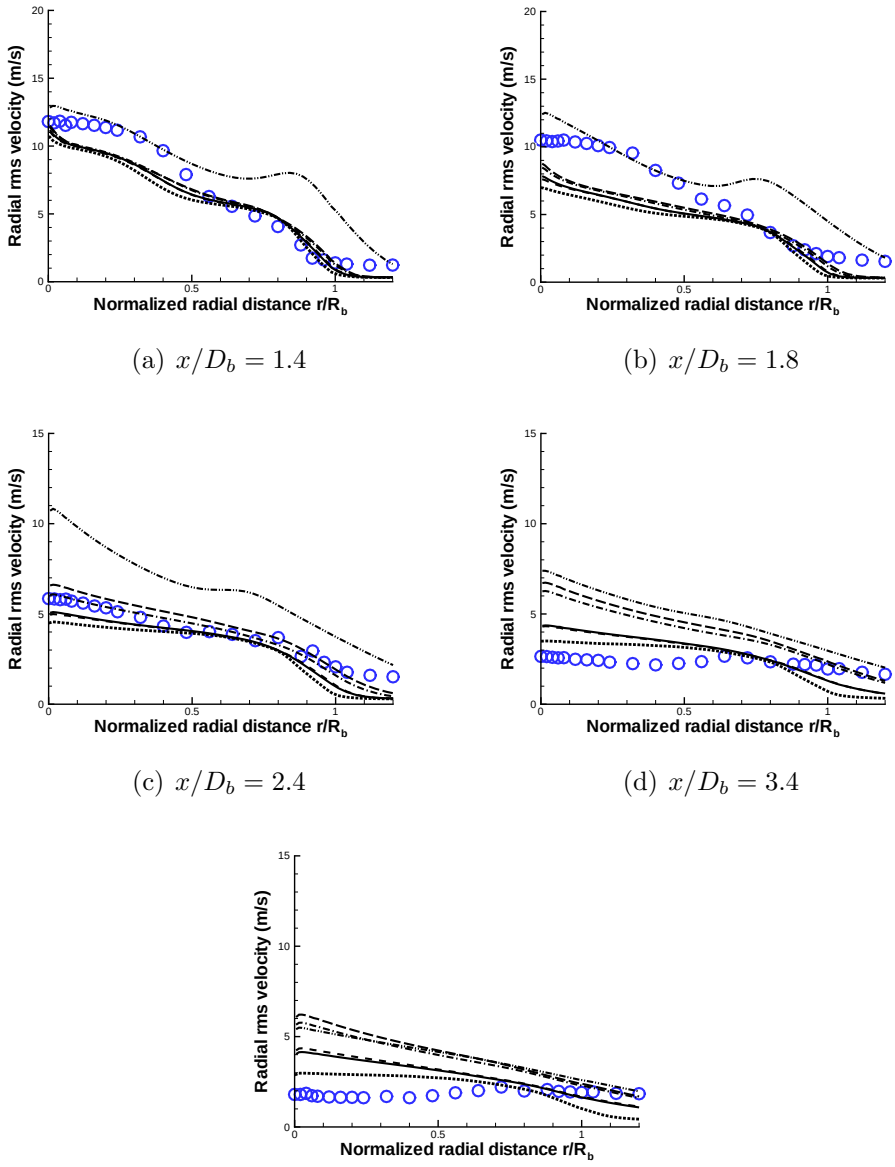

(a) $x/D_b = 1.4$

(b) $x/D_b = 1.8$

(c) $x/D_b = 2.4$

(d) $x/D_b = 3.4$

(e) $x/D_b = 4.4$

Figure 7.9: Comparison of radial rms velocities at at $x/D_b = 1.4, 1.8, 2.4, 3.4, 4.4$ in the RBB case using URANS. o: experimental data [16], dash-dot-dot: δ-PDF, long-dash: algebraic model, dotted: Case 1, dash-dot: Case 2, dashed: Case 3, Solid: Case 4.

7.3.2 Scalar Field

Figure 7.10 shows radial profiles of the scalar mean (i.e., mixture fraction, $\widetilde{Z}$) at the axial positions ($x/D_b \in \{0.26, 0.6, 0.9, 1.3, 1.8, 2.4\}$) and the results are compared with experimental data (HM1) [16]. Although different scalar dissipation rate models are used, all results show very similar trends as follows. In all cases, the $k-\varepsilon$ turbulence model reproduces the scalar mean value reasonably well near the bluff-body, but under-predicts those values downstream. Figure 7.10 demonstrates an overall good agreement between the measured and calculated scalar mean profiles except for a small over-prediction near the nozzle exit at $x/D_b = 0.26$ and a large under-estimate downstream, particularly after $x/D_b = 1.8$. The under-prediction of the scalar mean along the centerline at downstream stations is clearly related to the under-prediction of the centerline velocity at corresponding stations.

The radial profiles of the scalar variance are presented in Figure 7.11 at the same axial positions with the scalar mean profiles above. The transport equation model (Eq. (3.6)) and the algebraic model (Eq. (3.12)) for the scalar dissipation rate are employed with the same model constants. Note that there are no results obtained using the $\delta-$function PDF since it does not require the scalar variance. Firstly, the model constants for the transport equation, which are listed in Table 6.2, are calibrated and discussed. In the NRBB case, as shown in Figure 6.14, Case 3 and Case 4 show very similar results in predicting the scalar variance, and show the best agreement with experimental data among the four test cases while Case 1 over-predicts and Case 2 under-predicts. The RBB results show a trend very similar to the NRBB case. However, all scalar variance results are predicted to be slightly higher than those in NRBB, but those could represent the trend of variation to a certain extent. As a result, Case 2, which gives the lowest scalar variance among the transport models, shows the best agreement with experimental data among the test cases.

As identified in recent studies [49, 71], it is observed that the strong recirculation near the bluff-body leads to large-scale mixing. In Figure 7.11, it is also noticed in this

study. However, a secondary spike in vicinity of the edge of the bluff-body caused by the shear layer between the coflow and the recirculation zone [71] is not captured in the figure. The profiles for Case 2 basically over-predict experimental data over the entire domain. Moreover, the variation of the outer-vortex layer after $x/D_b = 1.8$ is not properly reproduced and it is also observed in the profiles obtained using the algebraic model. There are two main reasons for this deficiency; one is the limit of the $k-\varepsilon$ turbulence model and the other is the large vortex shedding along the outer layer.

It should be noted that the algebraic model gives quite impressive results compared to the transport equation models. As seen in Figure 7.11, the algebraic model shows good agreement with experimental data except at $x/D_b = 2.4$. Case 2 and the algebraic model show very similar trends and values of the scalar variance, but the algebraic model results become more diffusive earlier than in Case 2. This is also noticed in NRBB case as shown in Figure 6.15. However, as a result, this makes the algebraic model results come closer to experimental data since both over-predict it. The algebraic model gives the best results among the test cases.

Figure 7.12 shows a comparison of the radial distributions of mean temperatures at various axial locations. As expected from the scalar variance results, Case 2 and the algebraic model give good agreement with experimental data. The prediction quality of each case in the transport model varies by model; Case 2 gives the best results and Case 1 gives the worst. This is the reverse of the prediction quality of the scalar variance and is applicable over the entire domain. The results of Case 2 and the algebraic model predict the mean temperature reasonably well until $x/D_b = 0.6$. Downstream, however, the mean temperature profiles along the centerline show over-prediction possibly caused by the severe under-prediction in the mixture fraction field. Both the algebraic model and Case 2 also fail to reproduce the peak at the outer-vortex region most likely due to the strong vortex shedding in the outer shear layer. While Case 2 over-predicts the scalar variance in the inner-vortex layer slightly higher than the algebraic model after $x/D_b = 0.9$, both seem to predict the mean temperature with almost the same accuracy. A slight difference is found instead toward the outer

shear layer. This is actually observed in a comparison of the different transport equation models as well. It is obvious because most chemical reaction occurs in the recirculating zone.

The temperature profiles of Case 2 and the algebraic model show a peak at $x/D_b = 0.26$ near the outer shear layer ($r/R_b = 1.0$). The two results are too close to each other to be distinct in the figure, however. While this peak is not observed in measurements, it is noticed in previous studies [34, 71]. Dally *et al.* [16] suggested that non-existence of the peak distribution in measurements could be due to intermittent local extinction caused by the high scalar dissipation rate. However, Kuan and Lindstedt [40] stated that the influence of boundary conditions is particularly strong in this shear layer and also the measurement in this narrow region should be done cautiously. Based on the remarkable prediction of the mean and rms profiles of velocity and the scalar mean, Raman and Pitsch [71] suggested that the existence of the peak temperature zone corresponds to enhanced reactions at the interface of the recirculation and outer shear layer, and this could be attributed to the validity of flamelet assumption or the influence of under-predicted scalar variance. In any case, the exact source of this discrepancy is not yet clear.

The mean species mass fractions are compared with experimental data in Figure 7.13 to 7.16. Y_{CO_2} profiles in Figure 7.14 show reasonable agreement for all axial locations considered and the peak at $r/R_b = 1.0$ is also present. While Y_{CO_2} is under-predicted over the entire domain, the prediction worsens in the outer-vortex layer. As seen distinctly at axial position $x/D_b = 0.6$, the instability of the outer-vortex layer leads to bump at $r/R_b = 0.7$ while the peak moves towards the centerline. This is found slightly in the mean temperature profiles as well. Y_{CO} profiles in Figure 7.15 are a bit over-predicted in vicinity of inner-vortex layer. It has been known that equilibrium chemistry usually leads to the poor results for hydrocarbon combustion processes because Y_{CO} consumption rates are slow, especially for the very fuel-rich mixtures with low temperatures which are unlikely to reach the chemical equilibrium state.

Mass fraction of the hydroxyl radical are shown in Figure 7.16. Radical Y_{OH} is formed through the rapid two-body reaction $H + O_2 = OH + O$. Y_{OH} decays towards the

chemical equilibrium via the slower three-body recombination reaction $H+OH+M = H_2O+M$ [1, 19]. In turbulent reacting flows, the rate of mixing is much slower than the chemical reaction of the two-body reaction, but much faster than the three-body reaction [19]. This results in a superequilibrium amount of Y_{OH} upstream of the flame, which gradually diminishes to the chemical equilibrium amount further downstream. So, the prediction of Y_{OH} is a good indication of the predictive capability of the models for non-equilibrium effects. At the axial location near the bluff-body, the agreement is good but it becomes poor downstream of $x/D_b = 0.9$. At $x/D_b = 0.26$, the computed Y_{OH} shows a peak at $r/R_b = 1.0$ that is in line with the peak in the temperature profile in Figure 7.12. The peak is slightly over-predicted and shifted toward centerline, though. Downstream of $x/D_b = 0.9$, the simulation seems to fail to capture the hydroxyl radical appropriately. Despite the reasonable agreement of the scalar mean and the scalar variance profiles with experimental data up to $x/D_b = 1.3$, Y_{OH} is poorly reproduced. Raman and Pitsch [71] explain that the Y_{OH} profile is a highly non-linear function of the scalar variance, implying that minor errors in model predictions can lead to large deviations of Y_{OH} profiles.

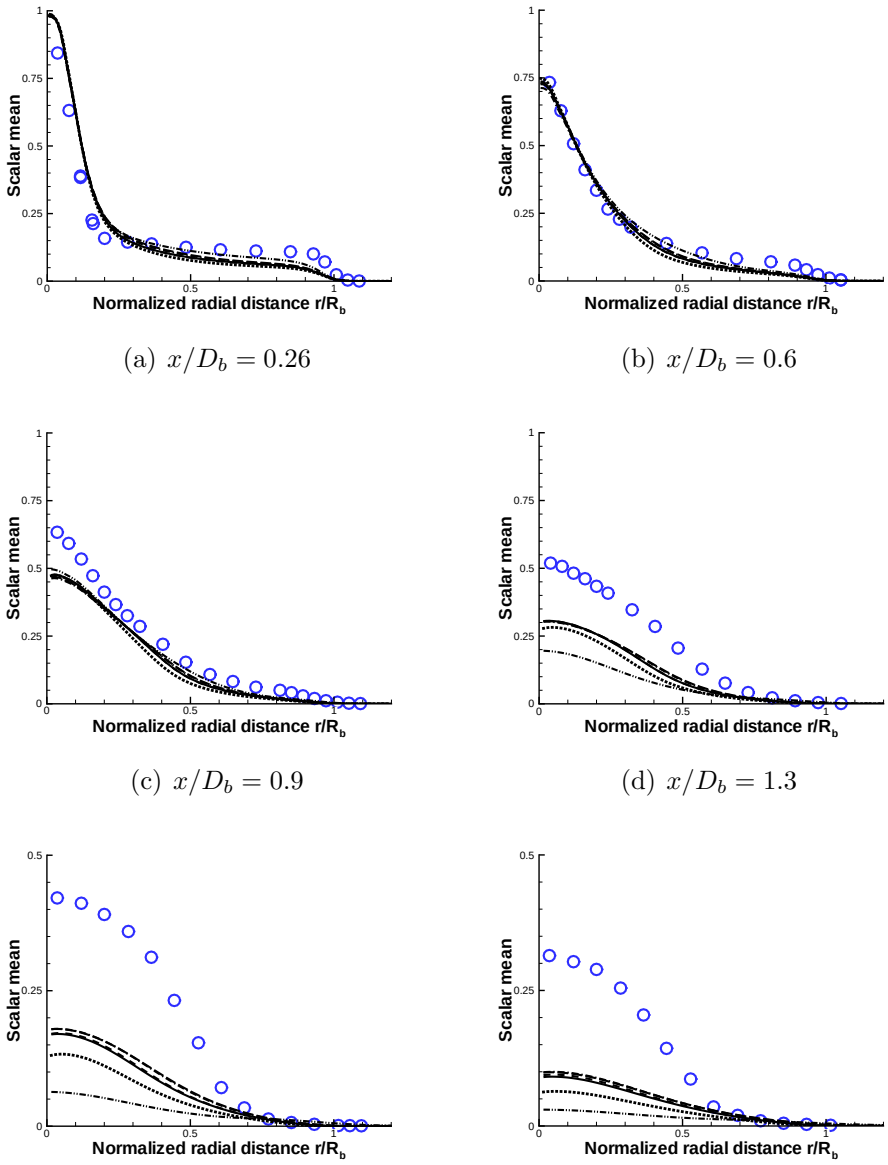

(a) $x/D_b = 0.26$ (b) $x/D_b = 0.6$

(c) $x/D_b = 0.9$ (d) $x/D_b = 1.3$

(e) $x/D_b = 1.8$ (f) $x/D_b = 2.4$

Figure 7.10: Scalar mean prediction at $x/D_b = 0.26, 0.6, 0.9, 1.3, 1.8, 2.4$ by solving the scalar dissipation rate transport equation with different model constants in the RBB case using URANS. o: experimental data [16], dash-dot-dot: δ-PDF, long-dash: algebraic model, dotted: Case 1, dash-dot: Case 2, dashed: Case 3, Solid: Case 4.

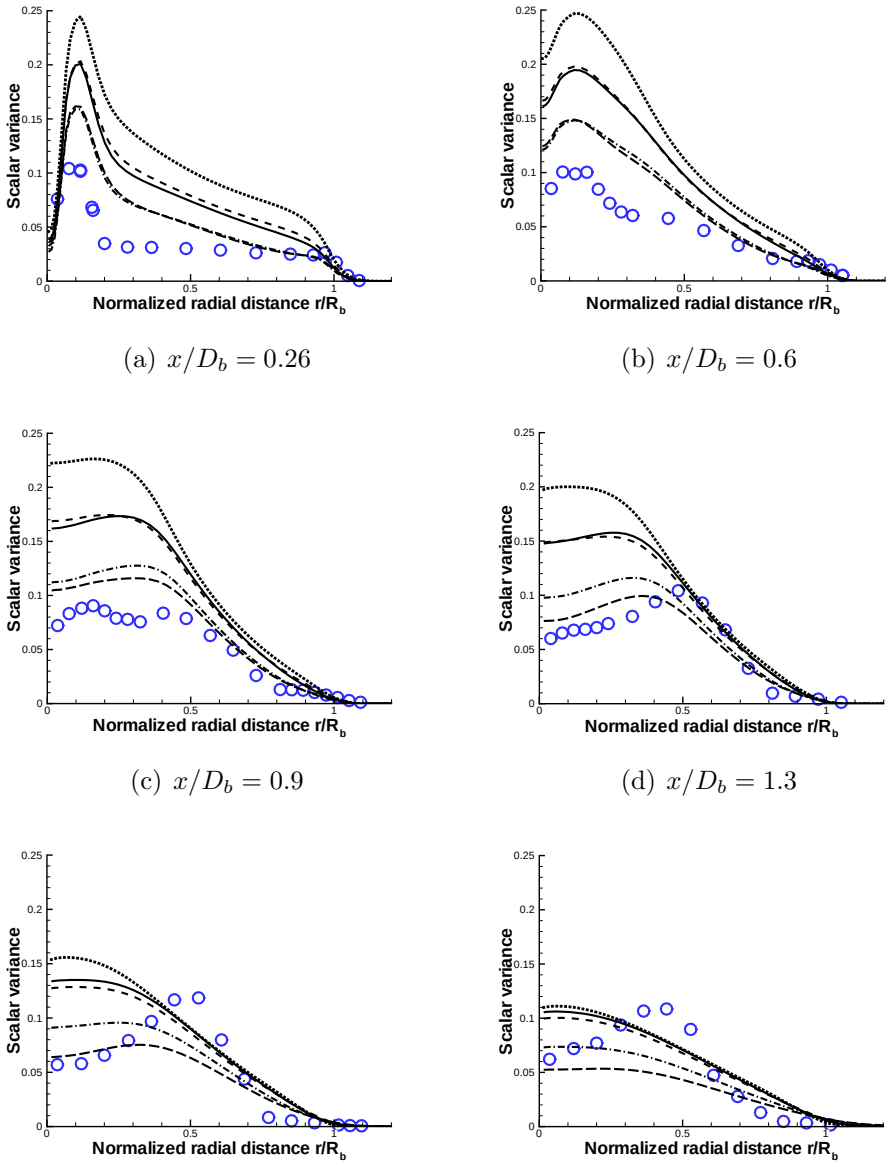

(a) $x/D_b = 0.26$ (b) $x/D_b = 0.6$

(c) $x/D_b = 0.9$ (d) $x/D_b = 1.3$

(e) $x/D_b = 1.8$ (f) $x/D_b = 2.4$

Figure 7.11: Scalar variance prediction at $x/D_b = 0.26, 0.6, 0.9, 1.3, 1.8, 2.4$ by the algebraic and the transport model in the RBB case using URANS. o: experimental data [16], long-dash: algebraic model, dotted: Case 1, dash-dot: Case 2, dashed: Case 3, Solid: Case 4.

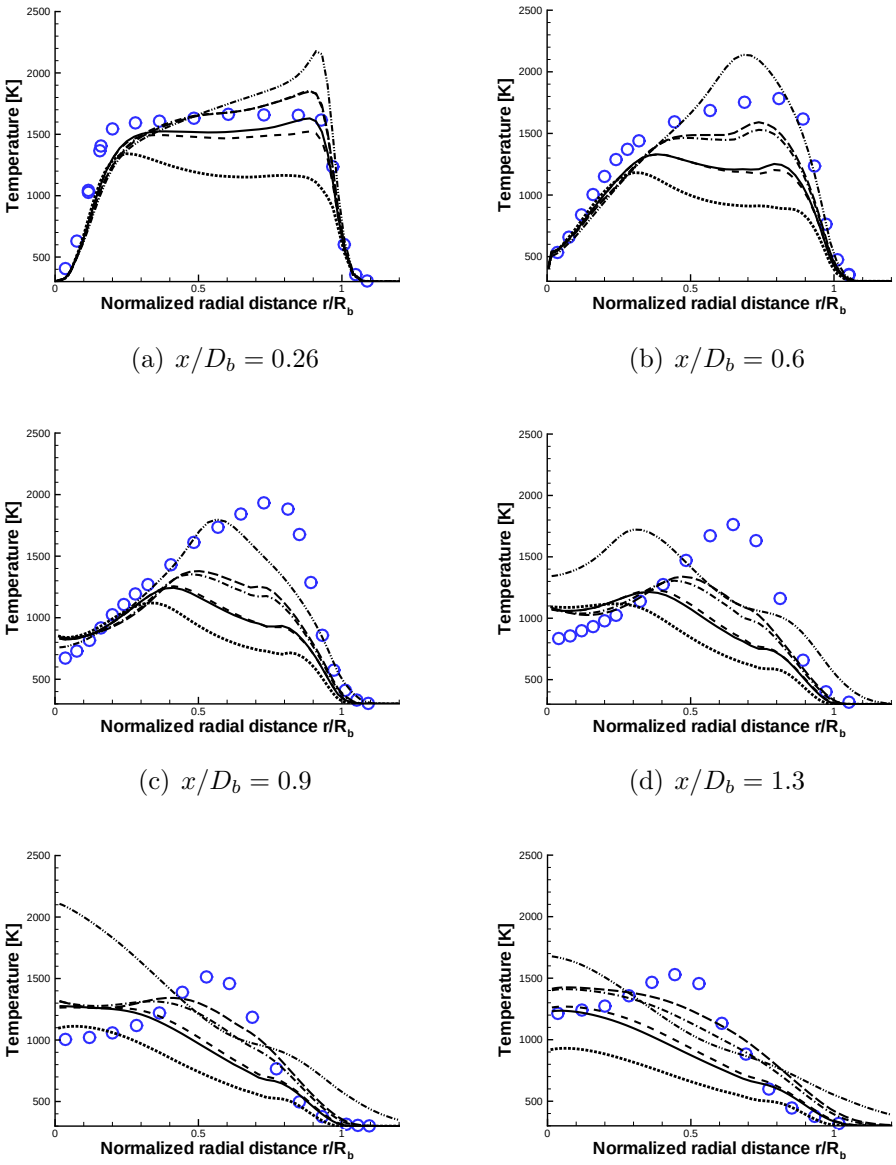

(a) $x/D_b = 0.26$ (b) $x/D_b = 0.6$

(c) $x/D_b = 0.9$ (d) $x/D_b = 1.3$

(e) $x/D_b = 1.8$ (f) $x/D_b = 2.4$

Figure 7.12: Mean temperature prediction at $x/D_b = 0.26, 0.6, 0.9, 1.3, 1.8, 2.4$ by the algebraic and the transport model in the RBB case using URANS. o: experimental data [16], dash-dot-dot: δ-PDF, long-dash: algebraic model, dotted: Case 1, dash-dot: Case 2, dashed: Case 3, Solid: Case 4.

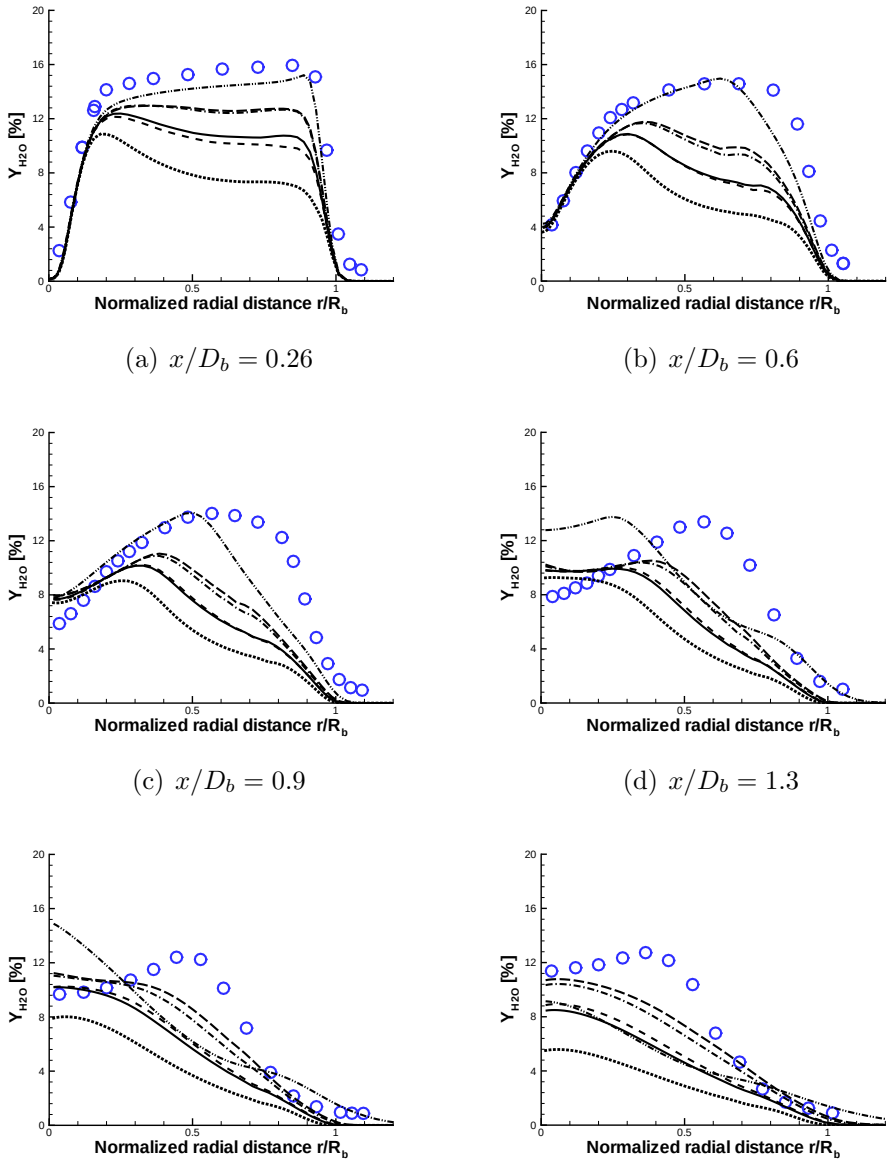

(a) $x/D_b = 0.26$ (b) $x/D_b = 0.6$

(c) $x/D_b = 0.9$ (d) $x/D_b = 1.3$

(e) $x/D_b = 1.8$ (f) $x/D_b = 2.4$

Figure 7.13: Y_{H_2O} prediction at $x/D_b = 0.26, 0.6, 0.9, 1.3, 1.8, 2.4$ by the algebraic and the transport model in the RBB case using URANS. o: experimental data [16], dash-dot-dot: δ-PDF, long-dash: algebraic model, dotted: Case 1, dash-dot: Case 2, dashed: Case 3, Solid: Case 4.

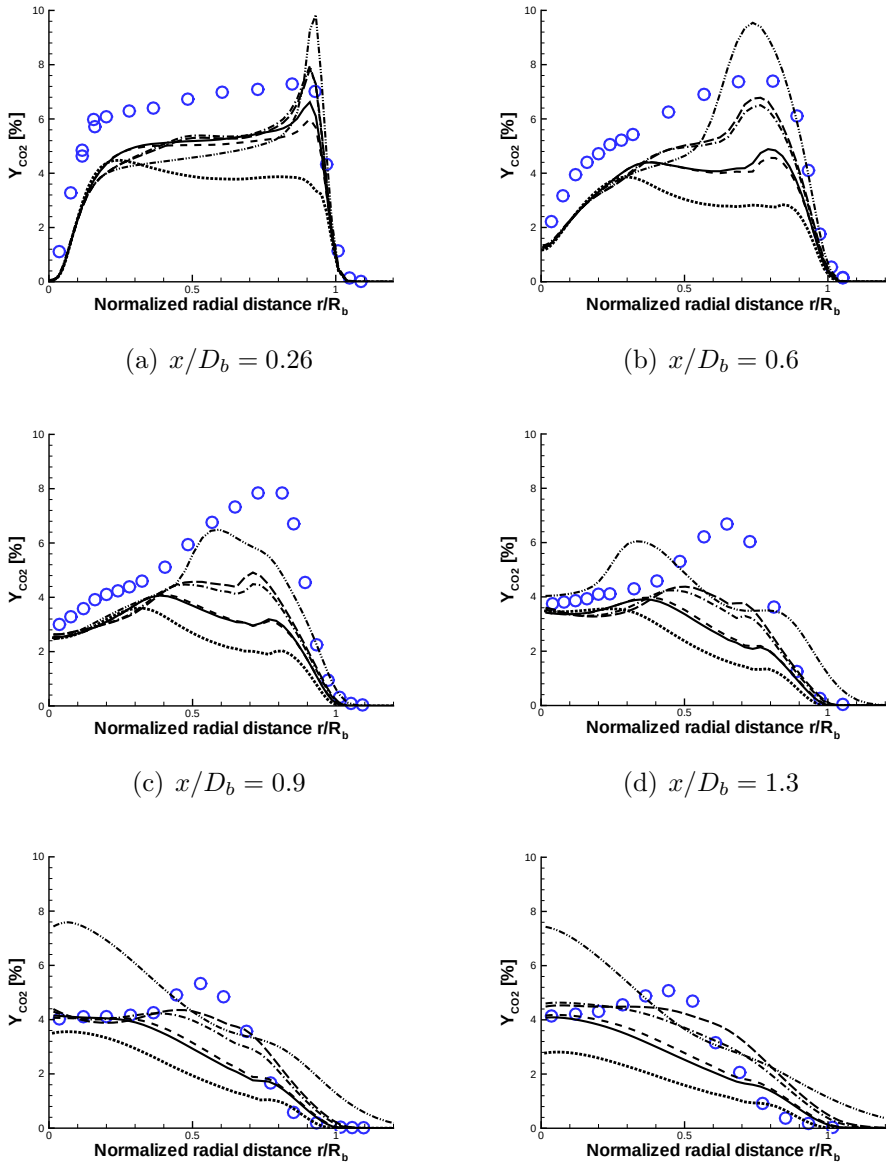

(a) $x/D_b = 0.26$ (b) $x/D_b = 0.6$

(c) $x/D_b = 0.9$ (d) $x/D_b = 1.3$

(e) $x/D_b = 1.8$ (f) $x/D_b = 2.4$

Figure 7.14: Y_{CO_2} prediction at $x/D_b = 0.26, 0.6, 0.9, 1.3, 1.8, 2.4$ by the algebraic and the transport model in the RBB case using URANS. o: experimental data [16], dash-dot-dot: δ-PDF, long-dash: algebraic model, dotted: Case 1, dash-dot: Case 2, dashed: Case 3, Solid: Case 4.

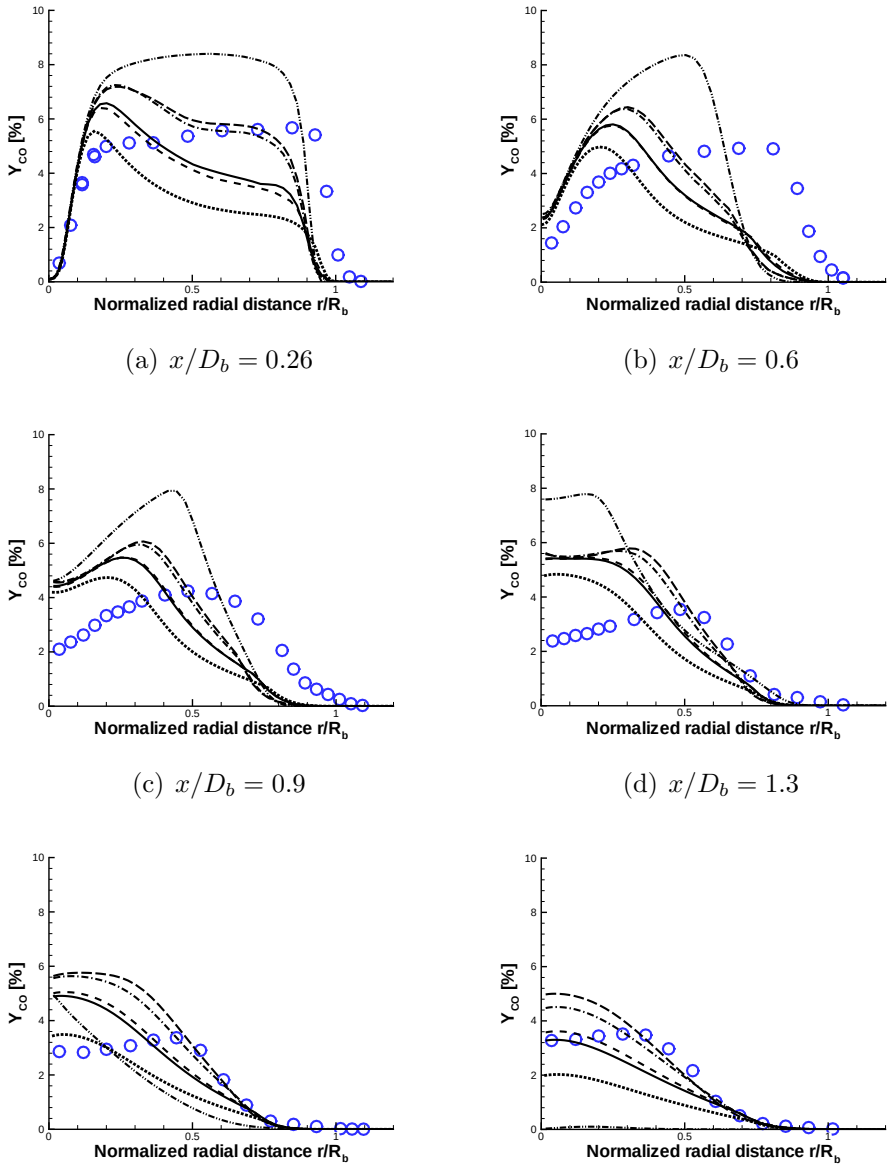

(a) $x/D_b = 0.26$ (b) $x/D_b = 0.6$

(c) $x/D_b = 0.9$ (d) $x/D_b = 1.3$

(e) $x/D_b = 1.8$ (f) $x/D_b = 2.4$

Figure 7.15: Y_{CO}prediction at $x/D_b = 0.26, 0.6, 0.9, 1.3, 1.8, 2.4$ by the algebraic and the transport model in the RBB case using URANS. o: experimental data [16], dash-dot-dot: δ-PDF, long-dash: algebraic model, dotted: Case 1, dash-dot: Case 2, dashed: Case 3, Solid: Case 4.

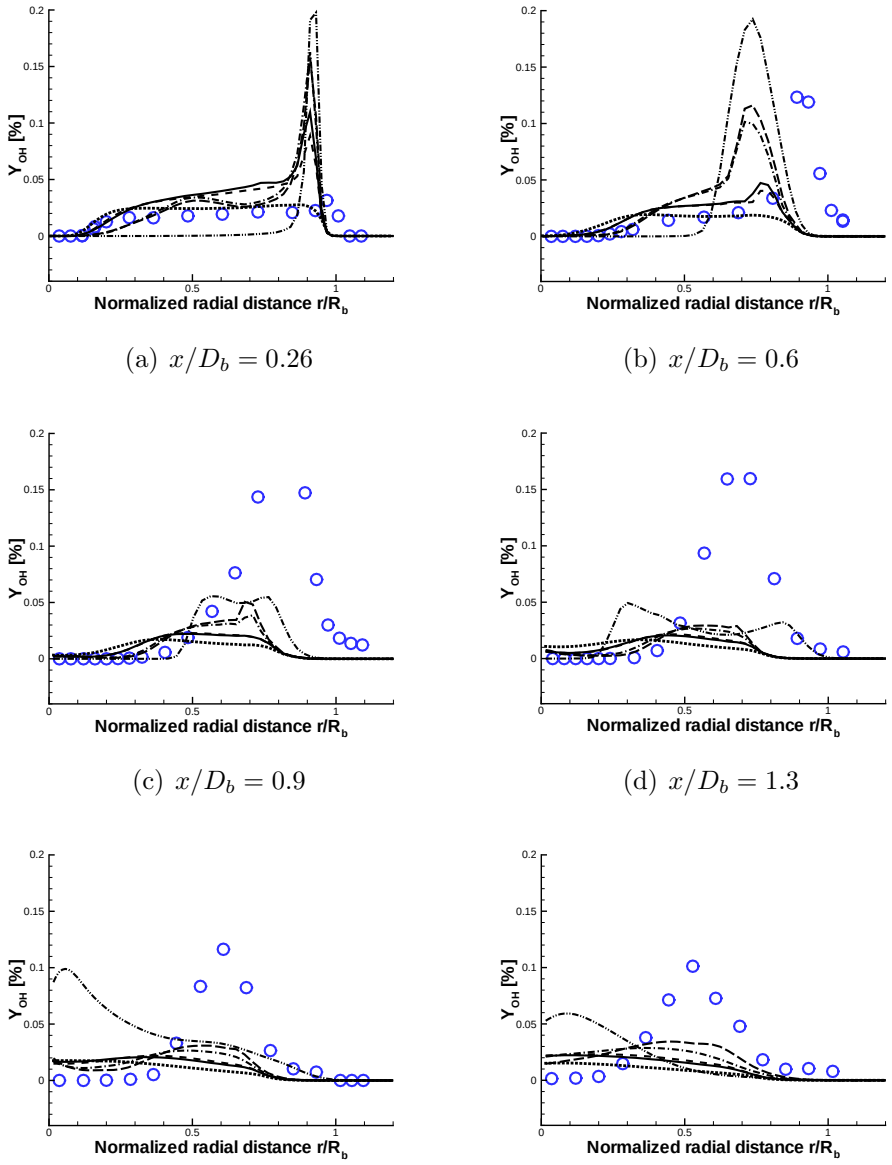

(a) $x/D_b = 0.26$ (b) $x/D_b = 0.6$

(c) $x/D_b = 0.9$ (d) $x/D_b = 1.3$

(e) $x/D_b = 1.8$ (f) $x/D_b = 2.4$

Figure 7.16: Y_{OH} prediction at $x/D_b = 0.26, 0.6, 0.9, 1.3, 1.8, 2.4$ by the algebraic and the transport model in the RBB case using URANS. o: experimental data [16], dash-dot-dot: δ-PDF, long-dash: algebraic model, dotted: Case 1, dash-dot: Case 2, dashed: Case 3, Solid: Case 4.

7.4 Summary and conclusion

The Sydney bluff-body reacting flow has been simulated by applying different scalar dissipation rate models. The existing algebraic model and newly proposed scalar dissipation rate transport equation are employed in pursuit of accurate scalar variance prediction. The chemical equilibrium model is used to describe the thermo-chemistry. Both velocity and species mass fraction statistics are compared with experimental data. The mean velocity profiles show good agreement with experimental data for both axial and radial velocity components. However, the mean velocity profiles along the centerline are under-predicted mainly due to the over-estimation of the spreading rate of the fuel-side jet. While the trend of axial rms velocity profiles follows the axial mean velocity profiles, the radial rms velocity profiles over-predicts the experimental data over the entire domain.

For all scalar dissipation rate model calculations, the scalar mean profiles show good agreement with the experimental data until $x/D_b = 1.3$, but severe under-prediction occurs downstream along the centerline. The reason of this seems to be in line with the velocity profiles. The scalar variance is obtained basically by two different models; the algebraic model and the transport equation model. Four different model constants for the scalar dissipation transport equation are calibrated. Case 2 among the model constant testing cases and the algebraic model give the best agreement with experimental data, a result consistent with NRBB case. The discrepancy between Case 2 and the algebraic model gets larger toward downstream showing that the centerline prediction of the algebraic model becomes diffusive quickly. This actually results in the algebraic model showing better agreement with experimental data downstream. The scalar variance is slightly over-predicted over the entire domain by Case 2 and therefore the model constants need to be adjusted. Based on the scalar variance prediction at $x/D_b = 0.6$ where the scalar mean shows great agreement with experimental data, it is suggested that the model constant C_3 be increased.

In general, the thermo-chemical variables such as temperature and the species mass fraction predicted by Case 2 and the algebraic model are in good agreement with

experimental data. At axial location $x/D_b = 0.26$, for most thermo-chemical variables, a peak near the edge at $r/R_b = 1.0$ of the bluff body is found. After the axial location $x/D_b = 0.9$, the peak temperature in the outer-vortex layer is not successfully captured, most likely due to the strong instability of the outer vortex. Species mass fractions show good agreement until $x/D_b = 1.3$ and the prediction worsens downstream. As expected, the hydroxyl radical, which is found by non-equilibrium chemistry, cannot be captured successfully due to the limitation of the chemical equilibrium assumption.

The trend of prediction in thermo-chemical variables seems very similar to the scalar mean profile. It could be said that the predictions of thermo-chemical variables are affected mainly by the prediction of the scalar mean. However, it should be also noted that there are big differences in predicting thermo-chemical variables according to different scalar variance predictions which are strongly coupled with different scalar dissipation rate models. As explained earlier, the local mixing state is modelled by the presumed $\beta-$function PDF in this work and the accuracy of this PDF relies heavily on the scalar mean and the variance. Considering that all different scalar dissipation models in consideration show very similar scalar mean profiles, it could be said that the better accuracy of the scalar dissipation rate modelling leads to improved prediction of the mean thermo-chemical variables through the accurate $\beta-$function PDF integration.

Chapter 8

Conclusions and Future work

8.1 Outcomes of the study

This thesis presents progress towards the application of large eddy simulation (LES) to turbulent reacting flows of engineering interest. The well-established turbulent combustion modelling techniques in RANS-based calculations were extended to LES in this study. The main effort of this study lies in the modelling of the scalar variance and its dissipation rate, which are necessary in the presumed $\beta-$function PDF approach with the conserved-scalar formalism. While a new model of the scalar variance and its dissipation rate in LES are pursued, URANS calculations were conducted to examine the differences between URANS and LES in predicting those variables. The comparative study was performed with same grid resolution for URANS and LES, as explained early, in order to see the advantage and disadvantage of converting RANS-based code to LES through the minimal change in turbulence modeling part of the code.

In many previous studies [34, 64, 71] which performed LES in combusting flows, the scalar variance and its dissipation rate were obtained through algebraic-type models. Moreover, those two variables were calculated separately. The scalar variance and

its dissipation rate are supposed to be solved via a coupled system, however. In this study, the transport equation for the scalar dissipation rate was proposed in consistency with the Smagorinsky SGS model and solved together with the scalar variance equation.

Two different scalar dissipation rate models were tested for simulating non-reacting (NRBB) and reacting (RBB) bluff-body turbulent flows using URANS and LES; one was the algebraic model and the other was the transport equation model. In the NRBB case, LES demonstrated better performance than URANS in predicting both the flow field and scalar field. The URANS calculation was able to predict the peak value and general trend but failed to represent the variation of the scalar variance in the outer-vortex layer region. The LES calculation showed great agreement with experimental data in predicting the scalar variance and was able to represent its variability. Among the scalar dissipation rate models, the transport equation model in both URANS and LES gave better performance particularly towards downstream where the algebraic model became more diffusive. The same approach was extended to the RBB case using URANS in conjunction with the chemical equilibrium model. The scalar mean field was well predicted until $x/D_b = 1.3$ after which it was severely under-predicted. Since the local distributions of the thermo-chemical variables are affected heavily by the scalar mean, all thermo-chemical variables such as mean temperature and species mass fractions showed similar trends. The scalar variance was found to be slightly over-predicted over the entire domain regardless of the scalar dissipation rate model and hence required adjustment of the model constant. Conclusively, the LES calculation solving the scalar variance and its dissipation rate transport equations shows the best performance among the possible combinations of simulations.

A LES code based on STREAM [44] was parallelized using the domain decomposition method, and the developed code was validated by simulating the turbulent channel flow before proceeding to the bluff-body simulations. Through this validation case, the wall boundary condition and SGS model implementation were tested successfully.

8.2 Future directions

Firstly, it is strongly suggested that the laminar flamelet model be incorporated with URANS. While the scalar dissipation rate contributes to the calculation of the scalar variance, it is also required to invoke the laminar flamelet solution since it accounts for the effect of turbulence on chemical reactions. It was author's initial plan to include the laminar flamelet calculations in this report. To this end, the steady laminar flamelet solver in Section 2.2.3 has been developed using TWOPNT ODE solver and the look-up table has been made.

Laminar flamelet calculations have been performed and some preliminary results were obtained (not presented). All thermo-chemical variables are predicted similarly to the chemical equilibrium model. The algebraic scalar dissipation rate model with the laminar flamelet combustion model shows slight improvement over the scalar dissipation rate model with the chemical equilibrium model. Since the laminar flamelet model can account for non-equilibrium chemistry, it was expected that the prediction of Y_{OH} could be improved when compared with the chemical equilibrium model. However, all the laminar flamelet simulations failed to deliver improvement of the prediction of Y_{OH}, and therefore the laminar flamelet simulations need to be investigated further. This failure in predicting Y_{OH} might be attributed to the trilinear interpolation which could generate errors when the value of Y_{OH} itself is very small. It is author's intent to apply a new integration method proposed by Lien *et al* [45] in which the $\beta-$function PDF is calculated analytically. This will help the integration procedure to minimize undesirable errors.

It should be noted here that the laminar flamelet calculation takes a very long time to converge since the residual oscillates severely. This was reported by Cook *et al* [14]. One possible cause is the scalar dissipation rate calculation. In the calculation of the scalar dissipation rate equation, Eq. (3.16), the scalar variance, which has quite a small value and varies significantly, serves as a denominator in the scalar destruction term. Since the scalar variance and its dissipation rate equations are solved as a coupled system, this issue of convergence can be difficult to avoid. Further investigation

into the numerical aspects of this matter be done in the near future.

Since all of the aforementioned developments of the scalar variance and its dissipation rate in LES are proposed to be used in simulating reacting flows, the LES calculation for the RBB case will be the next intended study. The superiority of LES over URANS in predicting the scalar mixing field was already confirmed for the NRBB case and it is in the author's interest to examine if LES demonstrates better performance than URANS in the RBB case. Furthermore, the main focus in performing LES calculations will be how the newly proposed approach in this study works for reacting flows.

Appendix A - Scalar variance in LES

For any local thermo-chemical variable $\phi_k(Z(x_1,t))$, the filtered mean in LES is defined as

$$\overline{\phi}_k(x,t) = \int \phi_k(Z(x_1,t))G(x-x_1,\overline{\Delta})dx_1, \tag{.1}$$

where the local thermo-chemical property is regarded as a function of the mixture fraction (Z). Using a δ-function,

$$\begin{aligned}
\overline{\phi}_k(x,t) &= \int_{x_1=-\infty}^{x_1=\infty} \left(\int_{\Psi=0}^{\Psi=1} \phi_k(\Psi)\delta\left[\Psi - Z(x_1,t)\right] d\Psi \right) G(x-x_1,\overline{\Delta})dx_1 \\
&= \int_{\Psi=0}^{\Psi=1} \phi_k(\Psi) \left(\int_{x_1=-\infty}^{x_1=\infty} \delta\left[\Psi - Z(x_1,t)\right] G(x-x_1,\overline{\Delta})dx_1 \right) d\Psi \\
&= \int_{\Psi=0}^{\Psi=1} \phi_k(\Psi) P(\Psi;x,t) d\Psi.
\end{aligned} \tag{.2}$$

The filtered probability density function [22] is defined as

$$P(\Psi;x,t) = \int_{x_1=-\infty}^{x_1=\infty} \delta\left[\Psi - Z(x_1,t)\right] G(x-x_1,\overline{\Delta})dx_1. \tag{.3}$$

The Favre-filtered variable is

$$\widetilde{\phi}_k(x,t) = \frac{\overline{\rho\phi_k}}{\overline{\rho}} = \int_{\Psi=0}^{\Psi=1} \phi_k(\Psi)\widetilde{P}(\Psi;x,t)d\Psi, \tag{.4}$$

where $\widetilde{P}(\Psi;x,t)$ is a Favre-filtered PDF.

The first and second moment of Ψ is required for the β-function PDF. The first moment of this PDF is calculated as

$$\begin{aligned}
\widetilde{Z} &= \int \Psi \widetilde{P}(\Psi)d\Psi \\
&= \int\int \Psi\delta\left[\Psi - Z(x_1,t)\right] G(x-x_1,\overline{\Delta})dx_1 d\Psi \\
&= \int Z(x_1,t)G(x-x_1,\overline{\Delta})dx_1.
\end{aligned} \tag{.5}$$

The second moment is

$$\begin{aligned}
\widetilde{Z''^2} &= \int (\Psi - \widetilde{Z})^2 \widetilde{P}(\Psi)d\Psi \\
&= \int\int \left(\Psi^2 - 2\Psi\widetilde{Z} + \widetilde{Z}^2\right)\delta\left[\Psi - Z\right] G(x-x_1,\overline{\Delta})dx_1 d\Psi \\
&= \int \left(Z^2 - 2Z\widetilde{Z} + \widetilde{Z}^2\right) G(x-x_1,\overline{\Delta})dx_1 \\
&= \widetilde{Z^2} - 2\widetilde{Z}\widetilde{Z} + \widetilde{Z}^2 \\
&= \widetilde{Z^2} - \widetilde{Z}^2,
\end{aligned} \tag{.6}$$

where $Z' = Z - \widetilde{Z}$ is the fluctuation part of the scalar in this study for LES.

Appendix B - Chemical Mechanism for CH_4/H_2 Combustion

Reaction	A_k	β_k	E_k
$2O + M \leftrightarrow O2 + M$	$1.200E+17$	-1.000	.00
$O + H + M \leftrightarrow OH + M$	$5.000E+17$	-1.000	.00
$O + H2 \leftrightarrow H + OH$	$5.000E+04$	2.670	6290.00
$O + HO2 \leftrightarrow OH + O2$	$2.000E+13$	.000	.00
$O + H2O2 \leftrightarrow OH + HO2$	$9.630E+06$	2.000	4000.00
$O + CH \leftrightarrow H + CO$	$5.700E+13$	.000	.00
$O + CH2 \leftrightarrow H + HCO$	$8.000E+13$	.000	.00
$O + CH2(S) \leftrightarrow H2 + CO$	$1.500E+13$	.000	.00
$O + CH2(S) \leftrightarrow H + HCO$	$1.500E+13$	.000	.00
$O + CH3 \leftrightarrow H + CH2O$	$8.430E+13$	.000	.00
$O + CH4 \leftrightarrow OH + CH3$	$1.020E+09$	1.500	8600.00
$O + CO + M \leftrightarrow CO2 + M$	$6.020E+14$	.000	3000.00
$O + HCO \leftrightarrow OH + CO$	$3.000E+13$	.000	.00
$O + HCO \leftrightarrow H + CO2$	$3.000E+13$	.000	.00
$O + CH2O \leftrightarrow OH + HCO$	$3.900E+13$	.000	3540.00
$O + CH2OH \leftrightarrow OH + CH2O$	$1.000E+13$	.000	.00
$O + CH3O \leftrightarrow OH + CH2O$	$1.000E+13$	.000	.00
$O + CH3OH \leftrightarrow OH + CH2OH$	$3.880E+05$	2.500	3100.00

$O + CH3OH \leftrightarrow OH + CH3O$	$1.300E+05$	2.500	5000.00
$O + C2H \leftrightarrow CH + CO$	$5.000E+13$	.000	.00
$O + C2H2 \leftrightarrow H + HCCO$	$1.020E+07$	2.000	1900.00
$O + C2H2 \leftrightarrow OH + C2H$	$4.600E+19$	−1.410	28950.00
$O + C2H2 \leftrightarrow CO + CH2$	$1.020E+07$	2.000	1900.00
$O + C2H3 \leftrightarrow H + CH2CO$	$3.000E+1$	.000	.00
$O + C2H4 \leftrightarrow CH3 + HCO$	$1.920E+07$	1.830	220.00
$O + C2H5 \leftrightarrow CH3 + CH2O$	$1.320E+14$	.000	.00
$O + C2H6 \leftrightarrow OH + C2H5$	$8.980E+07$	1.920	5690.00
$O + HCCO \leftrightarrow H + 2CO$	$1.000E+14$	.000	.00
$O + CH2CO \leftrightarrow OH + HCCO$	$1.000E+13$	.000	8000.00
$O + CH2CO \leftrightarrow CH2 + CO2$	$1.750E+12$	.000	1350.00
$O2 + CO \leftrightarrow O + CO2$	$2.500E+12$	.000	47800.00
$O2 + CH2O \leftrightarrow HO2 + HCO$	$1.000E+14$	.000	40000.00
$H + O2 + M \leftrightarrow HO2 + M$	$2.800E+18$	−.860	.00
$H + 2O2 \leftrightarrow HO2 + O2$	$3.000E+20$	−1.720	.00
$H + O2 + H2O \leftrightarrow HO2 + H2O$	$9.380E+18$	−.760	.00
$H + O2 + N2 \leftrightarrow HO2 + N2$	$3.750E+20$	−1.720	.00
$H + O2 + AR \leftrightarrow HO2 + AR$	$7.000E+17$	−.800	.00
$H + O2 \leftrightarrow O + OH$	$8.300E+13$	.000	14413.00
$2H + M \leftrightarrow H2 + M$	$1.000E+18$	−1.000	.00
$2H + H2 \leftrightarrow 2H2$	$9.000E+16$	−.600	.00
$2H + H2O \leftrightarrow H2 + H2O$	$6.000E+19$	−1.250	.00
$2H + CO2 \leftrightarrow H2 + CO2$	$5.500E+20$	−2.000	.00
$H + OH + M \leftrightarrow H2O + M$	$2.200E+22$	−2.000	.00
$H + HO2 \leftrightarrow O + H2O$	$3.970E+12$	.000	671.00
$H + HO2 \leftrightarrow O2 + H2$	$2.800E+13$	.000	1068.00
$H + HO2 \leftrightarrow 2OH$	$1.340E+14$	.000	635.00
$H + H2O2 \leftrightarrow HO2 + H2$	$1.210E+07$	2.000	5200.00
$H + H2O2 \leftrightarrow OH + H2O$	$1.000E+13$	.000	3600.00

$H + CH \leftrightarrow C + H2$	$1.100E+14$	.000	.00
$H + CH2(+M) \leftrightarrow CH3(+M)$	$2.500E+16$	$-.800$	.00
$H + CH2(S) \leftrightarrow CH + H2$	$3.000E+13$	.000	.00
$H + CH3(+M) \leftrightarrow CH4(+M)$	$1.270E+16$	$-.630$	383.00
$H + CH4 \leftrightarrow CH3 + H2$	$6.600E+08$	1.620	10840.00
$H + HCO(+M) \leftrightarrow CH2O(+M)$	$1.090E+12$	.480	-260.00
$H + HCO \leftrightarrow H2 + CO$	$7.340E+13$	.000	.00
$H + CH2O(+M) \leftrightarrow CH2OH(+M)$	$5.400E+11$	.454	3600.00
$H + CH2O(+M) \leftrightarrow CH3O(+M)$	$5.400E+11$	.454	2600.00
$H + CH2O \leftrightarrow HCO + H2$	$2.300E+10$	1.050	3275.00
$H + CH2OH(+M) \leftrightarrow CH3OH(+M)$	$1.800E+13$	.000	.00
$H + CH2OH \leftrightarrow H2 + CH2O$	$2.000E+13$	.000	.00
$H + CH2OH \leftrightarrow OH + CH3$	$1.200E+13$	.000	.00
$H + CH2OH \leftrightarrow CH2(S) + H2O$	$6.000E+12$	.000	.00
$H + CH3O(+M) \leftrightarrow CH3OH(+M)$	$5.000E+13$	.000	.00
$H + CH3O \leftrightarrow H + CH2OH$	$3.400E+06$	1.600	.00
$H + CH3O \leftrightarrow H2 + CH2O$	$2.000E+13$	.000	.00
$H + CH3O \leftrightarrow OH + CH3$	$3.200E+13$	.000	.00
$H + CH3O \leftrightarrow CH2(S) + H2O$	$1.600E+13$	.000	.00
$H + CH3OH \leftrightarrow CH2OH + H2$	$1.700E+07$	2.100	4870.00
$H + CH3OH \leftrightarrow CH3O + H2$	$4.200E+06$	2.100	4870.00
$H + C2H(+M) \leftrightarrow C2H2(+M)$	$1.000E+17$	-1.000	.00
$H + C2H2(+M) \leftrightarrow C2H3(+M)$	$5.600E+12$	.000	2400.00
$H + C2H3(+M) \leftrightarrow C2H4(+M)$	$6.080E+12$	.270	280.00
$H + C2H3 \leftrightarrow H2 + C2H2$	$3.000E+13$	.000	.00
$H + C2H4(+M) \leftrightarrow C2H5(+M)$	$1.080E+12$	.454	1820.00
$H + C2H4 \leftrightarrow C2H3 + H2$	$1.325E+06$	2.530	12240.00
$H + C2H5(+M) \leftrightarrow C2H6(+M)$	$5.210E+17$	$-.990$	1580.00
$H + C2H5 \leftrightarrow H2 + C2H4$	$2.000E+12$	.000	.00
$H + C2H6 \leftrightarrow C2H5 + H2$	$1.150E+08$	1.900	7530.00

$H + HCCO \leftrightarrow CH2(S) + CO$	$1.000E+14$	.000	.00
$H + CH2CO \leftrightarrow HCCO + H2$	$5.000E+13$	.000	8000.00
$H + CH2CO \leftrightarrow CH3 + CO$	$1.130E+13$	.000	3428.00
$H + HCCOH \leftrightarrow H + CH2CO$	$1.000E+13$	.000	.00
$H2 + CO(+M) \leftrightarrow CH2O(+M)$	$4.300E+07$	1.500	79600.00
$OH + H2 \leftrightarrow H + H2O$	$2.160E+08$	1.510	3430.00
$2OH(+M) \leftrightarrow H2O2(+M)$	$7.400E+13$	$-.370$	.00
$2OH \leftrightarrow O + H2O$	$3.570E+04$	2.400	-2110.00
$OH + HO2 \leftrightarrow O2 + H2O$	$2.900E+13$	.000	-500.00
$OH + H2O2 \leftrightarrow HO2 + H2O$	$1.750E+12$	.000	320.00
$OH + H2O2 \leftrightarrow HO2 + H2O$	$5.800E+14$	.000	9560.00
$OH + C \leftrightarrow H + CO$	$5.000E+13$	.000	.00
$OH + CH \leftrightarrow H + HCO$	$3.000E+13$	.000	.00
$OH + CH2 \leftrightarrow H + CH2O$	$2.000E+13$	.000	.00
$OH + CH2 \leftrightarrow CH + H2O$	$1.130E+07$	2.000	3000.00
$OH + CH2(S) \leftrightarrow H + CH2O$	$3.000E+13$	.000	.00
$OH + CH3(+M) \leftrightarrow CH3OH(+M)$	$6.300E+13$	.000	.00
$OH + CH3 \leftrightarrow CH2 + H2O$	$5.600E+07$	1.600	5420.00
$OH + CH3 \leftrightarrow CH2(S) + H2O$	$2.501E+13$	.000	.00
$OH + CH4 \leftrightarrow CH3 + H2O$	$1.000E+08$	1.600	3120.00
$OH + CO \leftrightarrow H + CO2$	$4.760E+07$	1.228	70.00
$OH + HCO \leftrightarrow H2O + CO$	$5.000E+13$	.000	.00
$OH + CH2O \leftrightarrow HCO + H2O$	$3.430E+09$	1.180	-447.00
$OH + CH2OH \leftrightarrow H2O + CH2O$	$5.000E+12$	.000	.00
$OH + CH3O \leftrightarrow H2O + CH2O$	$5.000E+12$	.000	.00
$OH + CH3OH \leftrightarrow CH2OH + H2O$	$1.440E+06$	2.000	-840.00
$OH + CH3OH \leftrightarrow CH3O + H2O$	$6.300E+06$	2.000	1500.00
$OH + C2H \leftrightarrow H + HCCO$	$2.000E+13$	.000	.00
$OH + C2H2 \leftrightarrow H + CH2CO$	$2.180E-04$	4.500	-1000.00
$OH + C2H2 \leftrightarrow H + HCCOH$	$5.040E+05$	2.300	13500.00

$OH + C2H2 \leftrightarrow C2H + H2O$	$3.370E+07$	2.000	14000.00
$OH + C2H2 \leftrightarrow CH3 + CO$	$4.830E-04$	4.000	−2000.00
$OH + C2H3 \leftrightarrow H2O + C2H2$	$5.000E+12$	.000	.00
$OH + C2H4 \leftrightarrow C2H3 + H2O$	$3.600E+06$	2.000	2500.00
$OH + C2H6 \leftrightarrow C2H5 + H2O$	$3.540E+06$	2.120	870.00
$OH + CH2CO \leftrightarrow HCCO + H2O$	$7.500E+12$	.000	2000.00
$2HO2 \leftrightarrow O2 + H2O2$	$1.300E+11$	.000	−1630.00
$2HO2 \leftrightarrow O2 + H2O2$	$4.200E+14$	.000	12000.00
$HO2 + CH2 \leftrightarrow OH + CH2O$	$2.000E+13$	.000	.00
$HO2 + CH3 \leftrightarrow O2 + CH4$	$1.000E+12$	.000	.00
$HO2 + CH3 \leftrightarrow OH + CH3O$	$2.000E+13$	.000	.00
$HO2 + CO \leftrightarrow OH + CO2$	$1.500E+14$	.000	23600.00
$HO2 + CH2O \leftrightarrow HCO + H2O2$	$1.000E+12$	.000	8000.00
$C + O2 \leftrightarrow O + CO$	$5.800E+13$	.000	576.00
$C + CH2 \leftrightarrow H + C2H$	$5.000E+13$	.000	.00
$C + CH3 \leftrightarrow H + C2H2$	$5.000E+13$	.000	.00
$CH + O2 \leftrightarrow O + HCO$	$3.300E+13$	.000	.00
$CH + H2 \leftrightarrow H + CH2$	$1.107E+08$	1.790	1670.00
$CH + H2O \leftrightarrow H + CH2O$	$1.713E+13$	.000	−755.00
$CH + CH2 \leftrightarrow H + C2H2$	$4.000E+13$	.000	.00
$CH + CH3 \leftrightarrow H + C2H3$	$3.000E+13$	.000	.00
$CH + CH4 \leftrightarrow H + C2H4$	$6.000E+13$	.000	.00
$CH + CO(+M) \leftrightarrow HCCO(+M)$	$5.000E+13$	.000	.00
$CH + CO2 \leftrightarrow HCO + CO$	$3.400E+12$	.000	690.00
$CH + CH2O \leftrightarrow H + CH2CO$	$9.460E+13$	.000	−515.00
$CH + HCCO \leftrightarrow CO + C2H2$	$5.000E+13$	.000	.00
$CH2 + O2 \leftrightarrow OH + HCO$	$1.320E+13$	.000	1500.00
$CH2 + H2 \leftrightarrow H + CH3$	$5.000E+05$	2.000	7230.00
$2CH2 \leftrightarrow H2 + C2H2$	$3.200E+13$	.000	.00
$CH2 + CH3 \leftrightarrow H + C2H4$	$4.000E+13$	.000	.00

$CH2 + CH4 \leftrightarrow 2CH3$	$2.460E+06$	2.000	8270.00
$CH2 + CO(+M) \leftrightarrow CH2CO(+M)$	$8.100E+11$	.500	4510.00
$CH2 + HCCO \leftrightarrow C2H3 + CO$	$3.000E+13$	.000	.00
$CH2(S) + N2 \leftrightarrow CH2 + N2$	$1.500E+13$	.000	600.00
$CH2(S) + AR \leftrightarrow CH2 + AR$	$9.000E+12$	.000	600.00
$CH2(S) + O2 \leftrightarrow H + OH + CO$	$2.800E+13$	.000	.00
$CH2(S) + O2 \leftrightarrow CO + H2O$	$1.200E+13$	.000	.00
$CH2(S) + H2 \leftrightarrow CH3 + H$	$7.000E+13$	.000	.00
$CH2(S) + H2O(+M) \leftrightarrow CH3OH(+M)$	$2.000E+13$	.000	.00
$CH2(S) + H2O \leftrightarrow CH2 + H2O$	$3.000E+13$	.000	.00
$CH2(S) + CH3 \leftrightarrow H + C2H4$	$1.200E+13$	.000	-570.00
$CH2(S) + CH4 \leftrightarrow 2CH3$	$1.600E+13$	.000	-570.00
$CH2(S) + CO \leftrightarrow CH2 + CO$	$9.000E+12$	.000	.00
$CH2(S) + CO2 \leftrightarrow CH2 + CO2$	$7.000E+12$	.000	.00
$CH2(S) + CO2 \leftrightarrow CO + CH2O$	$1.400E+13$	.000	.00
$CH2(S) + C2H6 \leftrightarrow CH3 + C2H5$	$4.000E+13$	.000	-550.00
$CH3 + O2 \leftrightarrow O + CH3O$	$2.675E+13$	.000	28800.00
$CH3 + O2 \leftrightarrow OH + CH2O$	$3.600E+10$	.000	8940.00
$CH3 + H2O2 \leftrightarrow HO2 + CH4$	$2.450E+04$	2.470	5180.00
$2CH3(+M) \leftrightarrow C2H6(+M)$	$2.120E+16$	$-.970$	620.00
$2CH3 \leftrightarrow H + C2H5$	$4.990E+12$	.100	10600.00
$CH3 + HCO \leftrightarrow CH4 + CO$	$2.648E+13$	.000	.00
$CH3 + CH2O \leftrightarrow HCO + CH4$	$3.320E+03$	2.810	5860.00
$CH3 + CH3OH \leftrightarrow CH2OH + CH4$	$3.000E+07$	1.500	9940.00
$CH3 + CH3OH \leftrightarrow CH3O + CH4$	$1.000E+07$	1.500	9940.00
$CH3 + C2H4 \leftrightarrow C2H3 + CH4$	$2.270E+05$	2.000	9200.00
$CH3 + C2H6 \leftrightarrow C2H5 + CH4$	$6.140E+06$	1.740	10450.00
$HCO + H2O \leftrightarrow H + CO + H2O$	$2.244E+18$	-1.000	17000.00
$HCO + M \leftrightarrow H + CO + M$	$1.870E+17$	-1.000	17000.00
$HCO + O2 \leftrightarrow HO2 + CO$	$7.600E+12$	.000	400.00

$CH2OH + O2 \leftrightarrow HO2 + CH2O$	$1.800E+13$	.000	900.00
$CH3O + O2 \leftrightarrow HO2 + CH2O$	$4.280E-13$	7.600	−3530.00
$C2H + O2 \leftrightarrow HCO + CO$	$5.000E+13$	.000	1500.00
$C2H + H2 \leftrightarrow H + C2H2$	$4.070E+05$	2.400	200.00
$C2H3 + O2 \leftrightarrow HCO + CH2O$	$3.980E+12$	.000	−240.00
$C2H4(+M) \leftrightarrow H2 + C2H2(+M)$	$8.000E+12$	.440	88770.00
$C2H5 + O2 \leftrightarrow HO2 + C2H4$	$8.400E+11$	.000	3875.00
$HCCO + O2 \leftrightarrow OH + 2CO$	$1.600E+12$	.000	854.00
$2HCCO \leftrightarrow 2CO + C2H2$	$1.000E+13$	.000	.00
$N + NO \leftrightarrow N2 + O$	$3.500E+13$	.000	330.00
$N + O2 \leftrightarrow NO + O$	$2.650E+12$	.000	6400.00
$N + OH \leftrightarrow NO + H$	$7.333E+13$	.000	1120.00
$N2O + O \leftrightarrow N2 + O2$	$1.400E+12$	.000	10810.00
$N2O + O \leftrightarrow 2NO$	$2.900E+13$	.000	23150.00
$N2O + H \leftrightarrow N2 + OH$	$4.400E+14$	.000	18880.00
$N2O + OH \leftrightarrow N2 + HO2$	$2.000E+12$	.000	21060.00
$N2O(+M) \leftrightarrow N2 + O(+M)$	$1.300E+11$	.000	59620.00
$HO2 + NO \leftrightarrow NO2 + OH$	$2.110E+12$	.000	−480.00
$NO + O + M \leftrightarrow NO2 + M$	$1.060E+20$	−1.410	.00
$NO2 + O \leftrightarrow NO + O2$	$3.900E+12$	.000	−240.00
$NO2 + H \leftrightarrow NO + OH$	$1.320E+14$	.000	360.00
$NH + O \leftrightarrow NO + H$	$5.000E+13$	.000	.00
$NH + H \leftrightarrow N + H2$	$3.200E+13$	.000	330.00
$NH + OH \leftrightarrow HNO + H$	$2.000E+13$	.000	.00
$NH + OH \leftrightarrow N + H2O$	$2.000E+09$	1.200	.00
$NH + O2 \leftrightarrow HNO + O$	$4.610E+05$	2.000	6500.00
$NH + O2 \leftrightarrow NO + OH$	$1.280E+06$	1.500	100.00
$NH + N \leftrightarrow N2 + H$	$1.500E+13$	.000	.00
$NH + H2O \leftrightarrow HNO + H2$	$2.000E+13$	.000	13850.00
$NH + NO \leftrightarrow N2 + OH$	$2.160E+13$	−.230	.00

$NH + NO \leftrightarrow N2O + H$	$4.160E+14$	$-.450$	.00
$NH2 + O \leftrightarrow OH + NH$	$7.000E+12$	.000	.00
$NH2 + O \leftrightarrow H + HNO$	$4.600E+13$	.000	.00
$NH2 + H \leftrightarrow NH + H2$	$4.000E+13$	.000	3650.00
$NH2 + OH \leftrightarrow NH + H2O$	$9.000E+07$	1.500	-460.00
$NNH \leftrightarrow N2 + H$	$3.300E+08$	.000	.00
$NNH + M \leftrightarrow N2 + H + M$	$1.300E+14$	$-.110$	4980.00
$NNH + O2 \leftrightarrow HO2 + N2$	$5.000E+12$	.000	.00
$NNH + O \leftrightarrow OH + N2$	$2.500E+13$	.000	.00
$NNH + O \leftrightarrow NH + NO$	$7.000E+13$	.000	.00
$NNH + H \leftrightarrow H2 + N2$	$5.000E+13$	.000	.00
$NNH + OH \leftrightarrow H2O + N2$	$2.000E+13$	.000	.00
$NNH + CH3 \leftrightarrow CH4 + N2$	$2.500E+13$	.000	.00
$H + NO + M \leftrightarrow HNO + M$	$8.950E+19$	-1.320	740.00
$HNO + O \leftrightarrow NO + OH$	$2.500E+13$	.000	.00
$HNO + H \leftrightarrow H2 + NO$	$4.500E+11$	.720	660.00
$HNO + OH \leftrightarrow NO + H2O$	$1.300E+07$	1.900	-950.00
$HNO + O2 \leftrightarrow HO2 + NO$	$1.000E+13$	.000	13000.00
$CN + O \leftrightarrow CO + N$	$7.700E+13$	.000	.00
$CN + OH \leftrightarrow NCO + H$	$4.000E+13$	.000	.00
$CN + H2O \leftrightarrow HCN + OH$	$8.000E+12$	.000	7460.00
$CN + O2 \leftrightarrow NCO + O$	$6.140E+12$	.000	-440.00
$CN + H2 \leftrightarrow HCN + H$	$2.100E+13$	.000	4710.00
$NCO + O \leftrightarrow NO + CO$	$2.350E+13$	.000	.00
$NCO + H \leftrightarrow NH + CO$	$5.400E+13$	.000	.00
$NCO + OH \leftrightarrow NO + H + CO$	$2.500E+12$	.000	.00
$NCO + N \leftrightarrow N2 + CO$	$2.000E+13$	.000	.00
$NCO + O2 \leftrightarrow NO + CO2$	$2.000E+12$	.000	20000.00
$NCO + M \leftrightarrow N + CO + M$	$8.800E+16$	$-.500$	48000.00
$NCO + NO \leftrightarrow N2O + CO$	$2.850E+17$	-1.520	740.00

$NCO + NO \leftrightarrow N2 + CO2$	$5.700E+18$	-2.000	800.00
$HCN + M \leftrightarrow H + CN + M$	$1.040E+29$	-3.300	126600.00
$HCN + O \leftrightarrow NCO + H$	$1.107E+04$	2.640	4980.00
$HCN + O \leftrightarrow NH + CO$	$2.767E+03$	2.640	4980.00
$HCN + O \leftrightarrow CN + OH$	$2.134E+09$	1.580	26600.00
$HCN + OH \leftrightarrow HOCN + H$	$1.100E+06$	2.030	13370.00
$HCN + OH \leftrightarrow HNCO + H$	$4.400E+03$	2.260	6400.00
$HCN + OH \leftrightarrow NH2 + CO$	$1.600E+02$	2.560	9000.00
$H + HCN + M \leftrightarrow H2CN + M$	$1.400E+26$	-3.400	1900.00
$H2CN + N \leftrightarrow N2 + CH2$	$6.000E+13$	.000	400.00
$C + N2 \leftrightarrow CN + N$	$6.300E+13$	.000	46020.00
$CH + N2 \leftrightarrow HCN + N$	$2.857E+08$	1.100	20400.00
$CH + N2(+M) \leftrightarrow HCNN(+M)$	$3.100E+12$	.150	.00
$CH2 + N2 \leftrightarrow HCN + NH$	$1.000E+13$	.000	74000.00
$CH2(S) + N2 \leftrightarrow NH + HCN$	$1.000E+11$	.000	65000.00
$C + NO \leftrightarrow CN + O$	$1.900E+13$	.000	.00
$C + NO \leftrightarrow CO + N$	$2.900E+13$	.000	.00
$CH + NO \leftrightarrow HCN + O$	$5.000E+13$	.000	.00
$CH + NO \leftrightarrow H + NCO$	$2.000E+13$	.000	.00
$CH + NO \leftrightarrow N + HCO$	$3.000E+13$	.000	.00
$CH2 + NO \leftrightarrow H + HNCO$	$3.100E+17$	-1.380	1270.00
$CH2 + NO \leftrightarrow OH + HCN$	$2.900E+14$	$-.690$	760.00
$CH2 + NO \leftrightarrow H + HCNO$	$3.800E+13$	$-.360$	580.00
$CH2(S) + NO \leftrightarrow H + HNCO$	$3.100E+17$	-1.380	1270.00
$CH2(S) + NO \leftrightarrow OH + HCN$	$2.900E+14$	$-.690$	760.00
$CH2(S) + NO \leftrightarrow H + HCNO$	$3.800E+13$	$-.360$	580.00
$CH3 + NO \leftrightarrow HCN + H2O$	$9.600E+13$	.000	28800.00
$CH3 + NO \leftrightarrow H2CN + OH$	$1.000E+12$	.000	21750.00
$HCNN + O \leftrightarrow CO + H + N2$	$2.200E+13$	.000	.00
$HCNN + O \leftrightarrow HCN + NO$	$2.000E+12$	.000	.00

$HCNN + O2 \leftrightarrow O + HCO + N2$	$1.200E+13$	.000	.00
$HCNN + OH \leftrightarrow H + HCO + N2$	$1.200E+13$	.000	.00
$HCNN + H \leftrightarrow CH2 + N2$	$1.000E+14$	.000	.00
$HNCO + O \leftrightarrow NH + CO2$	$9.800E+07$	1.410	8500.00
$HNCO + O \leftrightarrow HNO + CO$	$1.500E+08$	1.570	44000.00
$HNCO + O \leftrightarrow NCO + OH$	$2.200E+06$	2.110	11400.00
$HNCO + H \leftrightarrow NH2 + CO$	$2.250E+07$	1.700	3800.00
$HNCO + H \leftrightarrow H2 + NCO$	$1.050E+05$	2.500	13300.00
$HNCO + OH \leftrightarrow NCO + H2O$	$4.650E+12$	.000	6850.00
$HNCO + OH \leftrightarrow NH2 + CO2$	$1.550E+12$	.000	6850.00
$HNCO + M \leftrightarrow NH + CO + M$	$1.180E+16$	.000	84720.00
$HCNO + H \leftrightarrow H + HNCO$	$2.100E+15$	$-.690$	2850.00
$HCNO + H \leftrightarrow OH + HCN$	$2.700E+11$	.180	2120.00
$HCNO + H \leftrightarrow NH2 + CO$	$1.700E+14$	$-.750$	2890.00
$HOCN + H \leftrightarrow H + HNCO$	$2.000E+07$	2.000	2000.00
$HCCO + NO \leftrightarrow HCNO + CO$	$2.350E+13$	.000	.00
$CH3 + N \leftrightarrow H2CN + H$	$6.100E+14$	$-.310$	290.00
$CH3 + N \leftrightarrow HCN + H2$	$3.700E+12$	.150	-90.00
$NH3 + H \leftrightarrow NH2 + H2$	$5.400E+05$	2.400	9915.00
$NH3 + OH \leftrightarrow NH2 + H2O$	$5.000E+07$	1.600	955.00
$NH3 + O \leftrightarrow NH2 + OH$	$9.400E+06$	1.940	6460.00

Table 1: Chemical reactions in GRI-MECH 2.11.

Bibliography

[1] Barlow, R.S., Dibble, R.W., Lucht, R.P., and Chen, J.Y. Effect of Damköhler number on superequilibrium OH concentration in turbulent nonpremixed jet flames. *Combust. Flame*, 82:235–251, 1990.

[2] Beguier, C., Dekeyser, I., and Launder, B.E. Ratio of scalar and velocity dissipation time scales in shear flow turbulence. *Journal of Fluid Mechanics*, 21:307–310, 1978.

[3] Bilger, R.W. Turbulent jet diffusion flames. *Prog. Energy Combust. Sci.*, 1:87–109, 1976.

[4] Boussinesq, J. Essai sur la theories des eaux courantes. *Memoires presentes par divers savants a lAcademic des Sciences de lInstitut National de France*, 23:46–50, 1877.

[5] Bowman, C.T., Hanson, R.K., Davidson, D.F., Gardiner, W.C., Lissianski, Jr., V., Smith, G.P., Golden, D.M., Frenklach, M., and Goldenberg, M. *GRI-Mech 2.11.* http://www.me.berkeley.edu, 1995.

[6] Branley, N. and Jones, W.P. Large eddy simulation of a turbulent non-premixed flame. *Combust. Flame*, 127:1914–1934, 2001.

[7] Burke, S. P. and Schumann, T.E.W. Diffusion flames. *1st Symposium on Combustion*, 1:2–11, 1928.

[8] Chapman, D.R. Computational aerodynamics development and outlook. *AIAA Journal*, 17:1293–1313, 1979.

[9] Chen, C.S., Chang, K.C., and Chen, J.Y. Application of a robust beta-pdf treatment to analysis of thermal no formation in nonpremixed hydrogen-air flame. *Combust. Flame*, 98:375–390, 1994.

[10] Cheng, Y., Lien, F.S., Yee, E., and Sinclair, R. A comparison of large-eddy simulations with a standard k-e Reynolds-averaged Navier-Stokes model for the prediction of a fully developed turbulent flow over a matrix of cubes. *Journal of Wind Engineering and Industrial Aerodynamics*, 91:1301–1328, 2003.

[11] Chevray, R. and Tutu, R.K. Intermittency and preferential transport of heat in a round jet. *Journal of Fluid Mechanics*, 88:133–160, 1978.

[12] Cook, A.W. Determination of the constant coefficient in scale similarity models. *Physics of Fluids*, 9(5):1485–1487, 1997.

[13] Cook, A.W. and Riley, J.J. A subgrid model for equilibrium chemistry in turbulent flows. *Physics of Fluids*, 6(8):2868–2870, 1994.

[14] Cook, A.W., Riley, J.J., and Kosály, G. A laminar flamelet approach to subgrid-scale chemistry in turbulent flows. *Combust. Flame*, 109:332–341, 1997.

[15] Cuenot, B. and Poinsot, T. Effects of curvature and unsteadness in diffusion flames.implications for turbulent diffusion combustion. *Proceedings of the Combustion Institute*, 25:1383–1390, 1994.

[16] Dally, B.B., Masri, A.R., Barlow, R.S., and Fletchner, G.J. Instantaneous and mean compositional structure of bluff-body stabilized nonpremixed flames. *Combust. Flame*, 114:119–148, 1998.

[17] De Bruyn Kops, S.M., Riley, J.J., and Kosály, G. Investigation of modeling for non-premixed turbulent combustion. *Flow, Turbulence and combustion*, 60:105–122, 1998.

[18] Deardorff, J.W. A numerical study of three-dimensional turublent channel flow at large Reynolds numbers. *Journal of Fluid Mechanics*, 41(2):453–480, 1970.

[19] Drake, M.C., Blint, R.J., Lucht, R.P., and Chen, J.Y. Structure of laminar opposed flow diffusion flames with CO/H2/N2 fuel. *Combust. Sci. Tech.*, 61:187–224, 1988.

[20] Durbin, P.A. and Pettersson Reif, B.A. *Statistical theory and modeling for turbulent flows*. John Wiley and Sons, Ltd, 2001.

[21] Ferziger, J.H. and Peric, M. *Computational methods for fluid dynamics*. Springer, 2002.

[22] Gao, F. and O'Brien, E.E. A large-eddy simulation scheme for turbulent reacting flows. *Physics of Fluids*, 5(6):1282–1284, 1993.

[23] Germano, M., Piomelli, U., Moin, P., and Cabot, W.H. A dynamic subgrid-scale eddy viscosity model. *Physics of Fluids*, A(3):1760–1765, 1991.

[24] Girimaji, S.S. and Zhou, Y. Analysis and modeling of subgrid scalar mixing using numerical data. *Physics of Fluids*, 8(5):1224–1236, 1996.

[25] Grcar, J.F. The TWOPNT program for boundary value problems. Sandia Report SAND91-8320, Sandia Laboratory, 1992.

[26] Härtel, C. and Kleiser, L. Analysis and modeling of subgrid-scale motions in near-wall turbulence. *Journal of Fluid Mechanics*, 356:327–352, 1998.

[27] Janicka, J. and Sadiki, A. Large eddy simulation of turbulent combustion systems. *Proceedings of the Combustion Institute*, 30:537–547, 2005.

[28] Jiménez, C., Ducros, F., Cuenot, B., and Bédat, B. Subgrid scale variance and dissipation of a scalar field in large eddy simulations. *Physics of Fluids*, 13(6):1748–1754, 2001.

[29] Jiménez, J., Liñán, A., Rogers, M.M., and Higuera, F.J. A priori testing of subgrid models for chemically reacting nonpremixed turbulent shear flows. *Journal of Fluid Mechanics*, 349:149–171, 1998.

[30] Jimenez, J. and Moin, P. The minimal flow unit in near-wall turbulence. *Journal of Fluid Mechanics*, 225:213–240, 1991.

[31] Jones, W.P. and Musonge, P. Closure of the Reynolds stress and scalar flux equations. *Physics of Fluids*, 31:3589–3604, 1988.

[32] Kee, R.J., Rupley, F.M., and Miller, J.A. The CHEMKIN thermodynamic database. Sandia Report SAND87-8215B, Sandia Laboratory, 1992.

[33] Kempf, A., Flemming, F., and Janicka, J. Investigation of lengthscales,scalar dissipation,and flame orientation in a piloted diffusion flame by LES. *Proceedings of the Combustion Institute*, 30:557–565, 2005.

[34] Kempf, A., Lindstedt, R.P., and Janicka, J. Large-eddy simulation of a bluff-body stabilized nonpremixed flame. *Combust. Flame*, 144:170–189, 2006.

[35] Kempf, A., Sadiki, A., and Janicka, J. Prediction of finite chemistry effects using large eddy simulation. *Proceedings of the Combustion Institute*, 29:1979–1985, 2002.

[36] Kerstein, A.R. Linear-eddy modeling of turbulent transport. Part 4. structure of diffusion flames. *Combust. Sci. Tech.*, 81:75–96, 1992.

[37] Kim, J., Moin, P., and Moser, R. Turbulence statistics in fully developed channel flow at low Reynods number. *Journal of Fluid Mechanics*, 177:133–166, 1987.

[38] Klimenko, A.Y. and Bilger, R.W. Conditional moment closure for turbulent combustion. *Prog. Energy Combust. Sci.*, 25(6):595–687, 1999.

[39] Kravchenko, A.G., Moin, P., and Moser, R. Zonal embedded grids for numerical simulations of wall-bounded turbulent flows. *Journal of Computational Physics*, 127:412–423, 1996.

[40] Kuan, T.S. and Lindstedt, R.P. Transported probability density function modeling of a bluff-body stabilized turbulent flame. *Proceeding of Combustion Institution*, 30(1):767–774, 2005.

[41] Lentini, D. Assessment of the stretched lamainar flamelet approach for nonpremixed turbulent combustion. *Combust. Sci. Tech.*, 100:95–122, 1994.

[42] Lesieur, M. and Métais, O. New trends in large-eddy simulations of turbulence. *Annu. Rev. Fluid Mech.*, 28:45–82, 1996.

[43] Lien, F.S. *Computational modelling of 3D flow in complex ducts and passages.* PhD thesis, University of Manchester, 1992.

[44] Lien, F.S. and Leschziner, M.A. A general non-orthogonal collocated FV algorithm for turbulent flow at all speeds incorporating second moment closure. Part 1:computational implementation. *Computer Methods for Applied Mechanics and Engineering*, 114:123–148, 1994.

[45] Lien, F.S., Liu, H., Chui, E., and McCartney, C.J. Development of an Analytical beta-function pdf Integration Algorithm for Simulation of Non-premixed Turbulent Combustion. *Flow, Turbulence and Combustion*, 83:205–226, 2009.

[46] Liew, S.K. and Bray, K.N.C. A stretched laminar flamelet model of turbulent nonpremixed combustion. *Combust. Flame*, 56:199–213, 1984.

[47] Lilly, D.K. A proposed modification of the germano subgrid-scale closure method. *Physics of Fluids*, A(4):633–635, 1992.

[48] Liu, F., Guo, H., Smallwood, G.J., Gülder, Ö.L., and Matovic, M.D. A robust and accurate algorithm of the beta-pdf integration and its application to turbulent methane-air diffusion combustion in a gas turbine combustor simulator. *Int. J. of Thermal science*, 41:763–772, 2002.

[49] Liu, K., Pope, S.B., and Caughey, D.A. Calculations of bluff-body stabilized flames using a joint probability density function model with detailed chemistry. *Combust. Flame*, 141:89–117, 2005.

[50] Majander, P. and Siikonen, T. Evaluation of Smagorinsky-based subgrid-scale models in a finite-volume computation. *Int. J. for Numerical Methods in Fluids*, 336:95–102, 1991.

[51] MANNUAL. *MPI-2: Extensions to the Message-Passing Interface*. Message Passing Interface Forum, http://www.mpi-forum.org, 2003.

[52] Martinez, S.N. and Kronenburg, A. LES-CMC simulations of a turbulent bluff-body flame. *Proceedings of the Combustion Institute*, 31:1721–1728, 2007.

[53] Moin, P. Progress in large eddy simulation of turbulent flows. *AIAA 97-0749*, 1997.

[54] Moin, P. and Kim, J. Numerical investigation of turbulent channel flow. *Journal of Fluid Mechanics*, 118:341–377, 1982.

[55] Moser, R.D., Kim, J., and Mansour, N.N. Direct numerical simulations of turbulent channel flow. *Physics of Fluids*, 11:943–945, 1999.

[56] Muradoglu, M., Liu, K., and Pope, S.B. Pdf modeling of a bluff-body stabilized turbulent flame. *Combust. Flame*, 132:115–137, 2003.

[57] Newman, G.R., Launder, B.E., and Lumley, J.L. Modelling the behaviour of homogeneous scalar turbulence. *Journal of Fluid Mechanics*, 111:217–232, 1981.

[58] Norris, S.E. *A parallel Navier-Stokes solver for natural convection and free surface flow*. PhD thesis, University of Sydney, 2000.

[59] Panchapakesan, N.R. and Lumley, J.L. Turbulence measurements in axisymmetric jets of air and helium. Part 2. helium jet. *Journal of Fluid Mechanics*, 246:225–247, 1993.

[60] Patankar, S.V. *Numerical heat transfer and fluid flow*. Hemisphere publishing corporation, 1980.

[61] Peters, N. Laminar flamelet concepts in turbulent combustion. *Proceedings of the Combustion Institute*, 21:1231–1250, 1986.

[62] Peters, N. *Turbulent combustion*. Cambridge University Press, 2000.

[63] Pierce, C.D. and Moin, P. A dynamic model for subgrid-scale variance and dissipation rate of a conserved scalar. *Physics of Fluids*, 10(12):3041–3044, 1998.

[64] Pierce, C.D. and Moin, P. Large eddy simulation of a confined coaxial jet with swirl and heat release. *AIAA*, 10(12):3041–3044, 1998.

[65] Pierce, C.D. and Moin, P. Subgrid scale variance and dissipation of a scalar field in large eddy simulations. *Physics of Fluids*, 13(6):1748–1754, 2001.

[66] Pitsch, H. Improved pollutant predictions in large-eddy simulations of turbulent non-premixed combustion by considering scalar dissipation rate fluctuations. *Proceedings of the Combustion Institute*, 29:1971–1978, 2002.

[67] Pitsch, H. and Steiner, H. Large eddy simulation of a turbulent piloted Methane/Air diffusion flame. *Physics of Fluids*, 12(10):2541–2554, 2000.

[68] Pope, S.B. PDF methods for turbulent reactive flows. *Prog. Energy Combust. Sci.*, 11:119–192, 1985.

[69] Pope, S.B. *Turbulent flows*. Cambridge University Press, 2000.

[70] Press, W.H., Teukolsky, S.A., Vetterling, W.T., and Flannery, B.P. *Numerical recipes*. Cambridge University Press, 2007.

[71] Raman, V. and Pitsch, H. Large eddy simulation of a bluff-body-stabilized non-premixed flame using a recursive filter-refinement procedure. *Combust. Flame*, 142:329–347, 2005.

[72] Reynolds, W.C. The element potential for chemical equilibrium analysis: Implementation in the interactive program STANJAN. Technical Report A-3391, Stanford University, 1986.

[73] Rhie, C.M. and Chow, W.L. Numerical study of the turbulent flow past an airfoil with trailing edge separation. *AIAA Journal*, 21:1525–1532, 1983.

[74] Robinson, S.K. Coherent motions in the turbulent boundary layer. *Annual Review of Fluid Mechanics*, 23:601–639, 1991.

[75] Rodi, W. Comparison of LES and RANS calculations of the flow around bluff bodies. *Journal of Wind Engineering and Industrial Aerodynamics*, 69-71:55–75, 1997.

[76] Sagaut, P. *Large eddy simulation for incompressible flows*. Springer, 2002.

[77] Sagaut, P., Montreuil, E., Labbe, O., Comte, P., and Cambon, C. Analysis of the near-wall behaviour of some self-adaptive subgrid-scale models in finite difference simultations of channel flow. *International Journal of Numerical Methods in Fluids*, 40(10):1275–1302, 2002.

[78] Sanders, J.P.H. and Gökalp. Scalar dissipation rate modelling in variable density turbulent axisymmetric jets and diffusion flames. *Physics of Fluids*, 10:938–948, 1998.

[79] Sarghini, F. and Piomelli, U. Scale-similar subgrid-scale stress models for large-eddy simulation. *AIAA paper No. 98-0538*, 1998.

[80] Schumann, U. Subgrid-scale model for the finite difference simulations of turublent flows in plane channels and annuli. *Journal of Computational Physics*, 18:376–404, 1975.

[81] Scott, K.A. *Progress on the application of the NS-alpha model to wall-bounded flows*. PhD thesis, University of Waterloo, 2008.

[82] Smagorinsky, J. General circulation experiments with the primitive equations. *Monthly Weather Review*, 91:99–165, 1963.

[83] Sun, O.S. and Su, L.K. Experimental assessment of scalar mixing models for large-eddy simulation. *34th AIAA Fluid Dynamics Conference and Exhibit*, 2004.

[84] Versteeg, H.K. and Malalasekera, W. *An introduction to computational fluid dynamics: the finite volume method*. Prentice Hall, 1995.

[85] Warnatz, J., Mass, U., and Dibble, R.W. *Combustion: Physical and Chemical fundamentals, modelling and simulation, experiments, pollutant formation.* Springer-Verlag, 1996.

[86] Xie, Z. and Castro, I.P. LES and RANS for turbulent flow over arrays of wall-mounted obstacles. *Flow, Turbulence and Combustion*, 76:291–312, 2006.

[87] Ye, I.K., Lien, F.S., and Chui, E. Comparative study on scalar variance and dissipation rate in URANS and LES. *Proceedings of Combustion Institute - Canadian Section*, 2008.

[88] Zang, T. Numerical simulation of the dynamics of turbulent boundary layers: Perspectives of a transition simulation. *Philosophical Trans. of The Royal Society of London*, 336:95–102, 1991.